An experimental and theoretical investigation of the rheological properties and degradation of mucin solutions (or why saliva becomes watery when removed from your mouth)

by

Caroline Wagner

Honours B.Eng, Mechanical Engineering, McGill University (2013)

Submitted to the Department of Mechanical Engineering
in partial fulfillment of the requirements for the degree of

Master of Science in Mechanical Engineering

at the

MASSACHUSETTS INSTITUTE OF TECHNOLOGY

June 2015

Author ..... Signature redacted .....
Department of Mechanical Engineering
May 19, 2015

Certified by ..... Signature redacted .....
Gareth H. McKinley
Professor, Mechanical Engineering
Thesis Supervisor

Accepted by ..... Signature redacted .....
David E. Hardt
Graduate Officer, Department Committee on Graduate Students

An experimental and theoretical investigation of the rheological properties and degradation of mucin solutions (or why saliva becomes watery when removed from your mouth)

by

Caroline Wagner

Submitted to the Department of Mechanical Engineering
on May 19, 2015, in partial fulfillment of the
requirements for the degree of
Master of Science in Mechanical Engineering

Abstract

The use of biological fluids such as saliva and cervical mucus as diagnostics for measurements of health status is becoming increasingly popular in the fields of biology and medecine, particularly given the non-invasiveness and ease of obtaining such fluids [39, 78]. In general, these biological fluids are polymeric, and as a result tend to be viscoelastic. However, as a result of protease and enzymatic activity, these fluids are often unstable and can degrade with time [23, 65]. This was observed in the case of saliva by Aggazzotti nearly a century ago [1]. Therefore, in order to reliably quantify their rheological properties for diagnostic purposes, it is essential to understand how their microstructure affects the bulk rheological behaviours observed under testing conditions. We develop two models to simulate the behaviour of saliva during simple elongational flow and account for the decrease in viscoelasticity with time. The first model considerd is the FENE-P model of a fluid, which is particularly suitable for describing the rheology of dilute polymer solutions (Newtonian solvents containing small amounts of dissolved polymer) as a result of its ability to capture nonlinear effects arising from the finite extensibility of the polymer chains. In extensional flows, these polymer solutions exhibit dramatically different behaviour from the corresponding Newtonian solvents alone, notably through the creation of persistent filaments when stretched. By using the technique of capillary thinning to study the dynamics of the thinning process of these filaments, the transient extensional rheology of the fluid can be characterized. We show that under conditions of uniaxial elongational flow, a composite analytic solution can be developed to predict the time evolution of the radius of the filament. Furthermore we derive an analytic expression for the finite time to breakup of the fluid filaments. This breakup time agrees very well with results obtained from full numerical simulations, and both numerics and theory predict an increase in the time to breakup as the finite extensibility parameter b, related to the molecular weight of the polymer, is increased. As $b \to \infty$, the results converge to an asymptotic result for the breakup time which shows that the breakup time grows as $t_{break} \sim \ln(M_W)$, where M_W is the molecular weight of the dilute polymer solution. We then consider the importance of the network properties of saliva that arise due to entanglements of the polymer chains. In order to account for this, we combine the FENE-P model with the Rolie-Poly model developed by Graham et al [45, 50] to obtain the Rolie-Poly-FENE-P model. We show that this model

is better able to accurately predict the extensional behaviour of both polyethylene oxide (PEO) solutions and saliva based on actual properties of these materials. This model cannot capture the sudden filament breakup observed in young saliva samples, however, which motivates the incorporation of a mechanism for network junction association or 'stickiness', as has been done by [71, 74, 40, 25] amongst others in biological networks. We draw largely off of the work for Tripathi et al [67] who modeled the rheology of hydrophobically modified ethoxylate-urethane (HEUR) polymer solutions as associating networks in order to develop an analogous model for saliva. We show that this model can reproduce the asymptotic 'middle elastic time' exponential radius decay described by Entov and Hinch [22], the dynamics upon which CaBER experimental interpretation of the system relaxation time λ_H is based. We also show that incorporation of a stickiness parameter allows for good agreement between the model and experimental CaBER data for saliva samples at various ages.

Thesis Supervisor: Gareth H. McKinley
Title: Professor, Mechanical Engineering

Acknowledgments

My father has been teaching me science since I was a few months old, and I would be remiss if I did not acknowledge how big an impact he has had on my life and career choices. My family is unwavering in their support and love, and I am so lucky to have them. I would not have been able to maintain my motivation and happiness to complete this thesis without them. Dad, Mom, Yuli, Dave and Shado: thank you.

I would additionally like to thank Dr. Gareth McKinley for his tremendous support throughout this process. I have learned an incredible amount from him academically, but most importantly, Gareth has always emphasized that he would support me in any of the fluctuating and diverse career and academic goals that I proposed over the course of the last two years. I am happy that I ultimately decided to stay at MIT for my PhD, and look forward to continue working with him for an additional few years.

Without the members of the HML lab I would have lost motivation and energy a long time ago. Adi, Bavand, Alex: you are excellent friends and have taught me an incredible amount that has made me a much better scientist than I was when I arrived. Setareh: you are the best desk mate that anyone could have asked for. Ahmed: you have provided me with the distractions and food discussions that I needed to keep going. Justin: you are the most dependable person anyone could hope to work with. Jai, Michelle, Michela, Divya, Shabnam, Dayong, Sid, Andrew: I have been very fortunate to get to see you and work with you on a daily basis, and I look forward to continuing to do so.

I would finally like to acknowledge Dr. Bradley Turner, Erica Shapiro, Dr. Thomas Ober for their invaluable assistance in educating me regarding subjects for which I knew very little, and for helping me with experimental aspects of this work.

Contents

List of Figures

List of Tables

Chapter 1

Introduction

The addition of a small amount of polymer to a Newtonian solvent can yield rather dramatic differences in the behaviour of the fluid under various flow conditions. When subjected to shearing flows, the ability of the polymer chains to align themselves and unravel in the flow direction leads to phenomena such as shear thinning, where the viscosity of the fluid is observed to decrease with increasing applied rate of shear due to the increasing orderliness of the contained polymer (although a very small number of polymeric fluids exhibit shear thickening, where the opposite effect of increasing viscosity with shear rate is observed due to dilation of the polymers [12]). This feature is heavily employed in the food industry with various polysaccharides such as Xanthan gum and Guar gum [35], where the imparted shear thinning permits many desirable behaviours. For instance, addition of Xanthan gum to salad dressing increases the viscosity when the dressing is on the shelf (at rest, low rate of shear), allowing the various herbs contained to remain in suspension and hence look more attractive to the buyer. When shaken (resulting in an increased shear rate), however, the viscosity decreases and the solution can be easily poured. When stretched as a result of being subjected to an extensional flow, polymer solutions tend to form persistent filaments and delay capillary breakup as a result of the increased resistance to flow provided by the polymer chains [47, 12]. These phenomena make polymer solutions attractive for many industrial applications, including extrusion processing and inkjet printing. In the latter, droplets of ink are ejected at high speed from a small nozzle, resulting in the formation of a near spherical droplet with a trailing filament [31]. It is desired that the trailing filament remain intact and not break up

into smaller trailing droplets (known as satellite droplets), as the printing sharpness and quality can be compromised by impact of these undesired and uncontrolled droplets on the printing surface [31]. Polymer is therefore added to the ink in order to delay this undesired breakup [31, 68, 51].

Many biological fluids are also polymeric, and the rheological properties that they possess are crucial for many of the functions that they serve. For instance, the polysaccharides found in mammalian synovial fluid are responsible for its lubricating properties, and the mucins found in saliva and mucous impart the elasticity needed for (amongst other things) lubrication, facilitated swallowing, and barriers against bacterial penetration [61, 35]. In as early as 1908, Fano studied these phenomena in biopolymer solutions such as egg white, bile, and plant extracts [26]. Since then, characterization and quantification of this polymer-induced elasticity has been of great academic interest, with one current application being use as a diagnostic tool to monitor the state of the fluid in question. For instance, Kopito and Kosasky [39] performed fertility studies to assess hormone levels during the menstrual cycle by measuring the rheological properties of cervical mucus. Further, Basilevsky and coworkers have explored the degradation of sputum upon exposure to certain bacteria as measured through changes in its elastic properties [9]. As a final example, Zussman and coworkers have noted that differences in saliva viscoelasticity between teenagers and the elderly may explain why the most common dental health issues plaguing these two age groups differ [78].

In a similar vein, the modelling of the fragmentation process of mucosalivary fluid during a violent expiratory event such as a cough or a sneeze is a crucial aspect of the study of respiratory disease transmission [14, 76, 6]. During such an event, an inspiration of air is followed by closure of the glottis and simultaneous contraction of the abdominal and intercostal muscles, which raises the diaphragm and results in a decrease in the effective volume surrounding the lungs [17]. This leads to an increase in the intrapleural pressure, which causes the glottis to open partially, sending out a short burst of high speed air. This shearing flow over the mucus in the trachea and saliva in the mouth leads to a complex process of fragmentation and droplet breakup in these fluids layers,

and the size of the resulting emitted droplets is crucial in the determination of the transmission mechanism of any potential contained pathogens [14, 6, 62, 60]. Smaller droplets ($\lesssim 5 - 10\mu m$) generally favour airborne transmission, as they dry very quickly and result in the pathogen remaining suspended in the air (where it is susceptible to being inhaled). On the other hand, larger drops, which tend to settle quickly under gravity, pose a greater threat of direct disease transmission through spraying onto susceptible surfaces [14]. As could be expected, the rheological properties of these mucosalivary fluids lead to their fragmentation processes differing greatly from a simple Newtonian fluid such as water. The polymer-induced elasticity from the mucin in these fluids leads to the creation of long filaments and delayed capillary breakup (as described above for inkjet printing), which affects the size distribution of droplets created [14]. Proper viscoelastic characterization of these fluids is therefore essential for the study and understanding of how respiratory diseases are transmitted.

In attempting to characterize the shear and extensional properties of saliva, it quickly becomes apparent that unlike synthetic non-Newtonian fluids which have repeatable rheological properties, those of saliva are highly variable. Firstly there is variability amongst subjects [61], but also within a given donor depending on time of day, proximity to last meal, and even hormonal cycle [64]. To complicate things further, the viscoelasticity of saliva decreases with time once the sample has been extracted from the mouth. Aggazzotti reported this observation in as early as 1922 [1] in his ground-breaking studies of *potere filante* or filament forming potential. He performed a series of experiments on saliva at various ages, such as stretching filaments until they broke and recording their maximum extensions, and examining the solubility of salivary components through the addition of acetic acid. His results showed a decrease in the maximum extension length of the thread, as well as an increase in the solubility of saliva as it aged. Although he did not draw this conclusion himself, both results suggest that as saliva ages, the molecular weight of the biopolymer contained in saliva decreases as a result of biological degradation mechanisms.

The importance of the ability to correctly quantify the viscoelastic properties of biological poly-

meric fluids is therefore clear. However, just as clear is the difficulty of being able to do so, particularly in the context of degradation and time-dependent evolution of the fluid properties. Therefore, the primary objective of this thesis is to provide a model to explain the observed changes in the rheological behaviour of saliva (and biopolymer fluids in general) as it ages, and to compare this model with experimental data. Ultimately, the goal of this work is to relate the molecular structure of biopolymers to the macroscale rheological properties that are observable in the fluids that contain them through both rheological experimentation and mathematical modelling.

Chapter 2

Saliva

2.1 Structure and Function

Saliva is composed primarily of water (99.5%) as well as proteins (0.2%) and other inorganic and trace substances (0.2%) [61]. Various glands in the mouth secrete different salivary components, the nature of which varies according to the ratio of serous to mucous cells that comprise the given gland. Serous cells, dominant in the parotid and submandibular glands, produce a more watery secretion that is strongly activated by stimuli, whereas mucous cells which are large components of the sublingual gland produce a more mucous-rich secretion [61]. All together, these various secretions as well as sloughed off endothelial cells, traces of food, blood, and other components comprise the complex network of whole saliva.

The list of essential bodily functions facilitated or permitted by saliva is a lengthy one. The majority of these functions arise from the viscoelasticity of saliva imparted by the network components. For instance, the ability of saliva to form a film that coats the various oral components is essential for lubrication, without which speech and swallowing is extremely difficult [13]. Additionally, food texture, taste perception, and mouth feel are all strongly dependent on the viscoelastic properties of saliva [64]. The salivary film is also crucial for the maintenance of oral health, as it protects the mucosa from bacterial attack and the teeth from demineralisation [61, 13].

The primary type of protein secreted in saliva is the glycoprotein mucin, of which MUC5B is the major component associated with the gel matrix of saliva [61]. However, Raynal et al have shown that solutions of pure MUC5B mucin at concentrations comparable to those found in saliva (approximately $200\mu g/ml$), do not reproduce the same rheological properties [56]. Indeed, other salivary components have more recently been identified as important players in the network, such as salivary micelles [61]. These are casein-like micelles composed of a wide range of molecules such as MUC7 mucin, sIgA antibody, lactoferrin, amylase, glycosylated PRP proteins, and lysozymes [61]. Figure 2-1 shows a summary cartoon of the various components that constitute the salivary network.

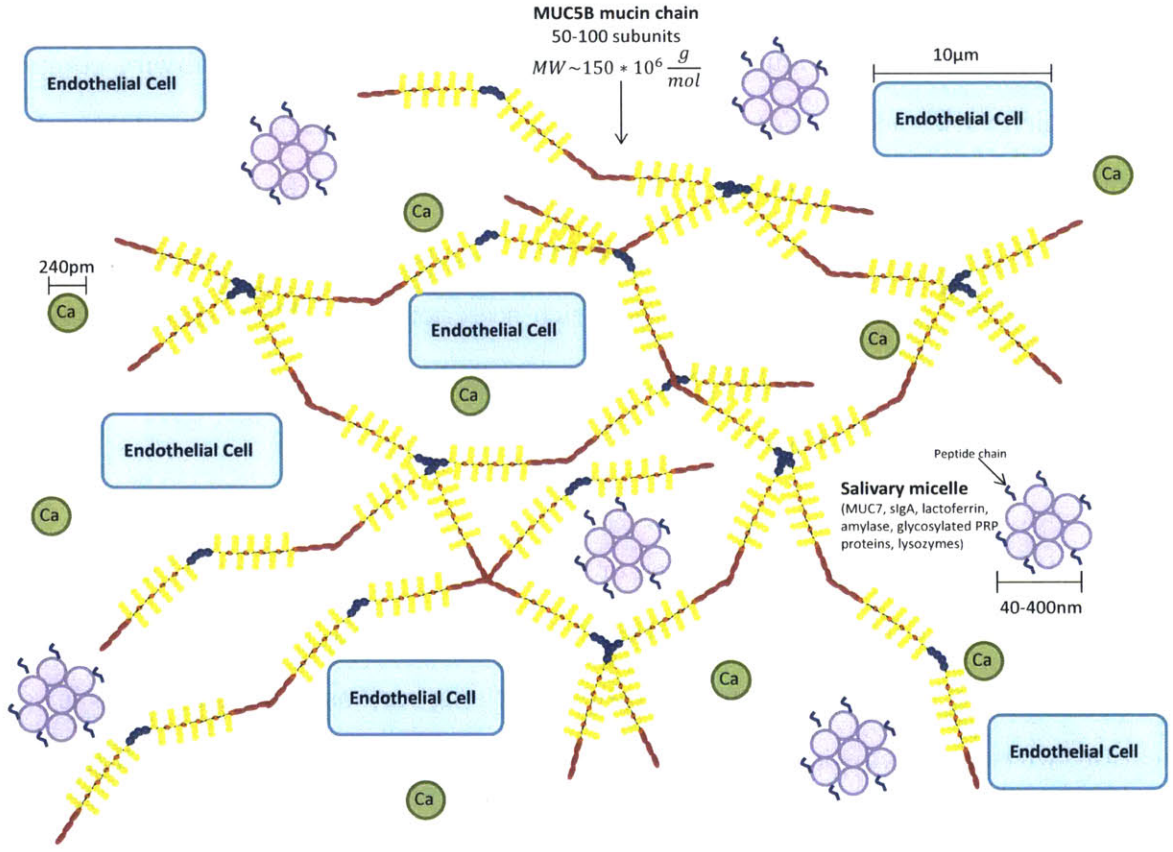

Figure 2-1: Cartoon recreation of the components of saliva based off the work of Schipper et al [61].

The structure of the high molecular weight MUC5B mucin ($MW \approx 1 - 2MDa$ [37]) deserves particular attention. Like the other members of the MUC family, MUC5B is highly glycosylated, consisting of about 80% carbohydrates: predominantly N-acetylgalactosamine, N-acetylglucosamine, fucose, galactose, sialic acid, and traces of mannose and sulfate [5, 20]. These carbohydrates form moderately branched oligosaccharide chains that attach to the protein core in a "bottle brush" configuration via O-glycosidic bonds to the hydroxyl side chains of serines and theonines [5]. Five such heavily glycosylated areas exist in MUC5B, and interspersed with them are an additional five relatively unglycosylated, cysteine rich regions, whose structure is more representative of globular proteins [37, 5]. The end regions of the mucin consist of one amino (NH_2) terminal and one carboxyl ($COOH$) terminal, which are both unglycosylated and cysteine rich [5]. The intact MUC5B molecule found in secretions consists of $50 - 100$ subunits assembled in a linear fashion [37]. The individual monomers form dimers through disulfide bonds at the $COOH$ terminals, and subsequently polymerize into lengthy chains through similar disulfide bonds at the NH_2 terminals [37]. Figure 2-2 A, taken from Schipper et al [61] shows a Cryo-SEM image of saliva in which the mucin network is clearly visible. In Figure 2-2 B, taken from Kesimer et al [37], the structure of the MUC5B molecule is clearly shown. The arrows indicate the NH_2 and $COOH$ terminal regions highlighted by 5nm colloidal gold markers. The average length between gold labels is $500nm$, the approximate length of a MUC5B monomer [37].

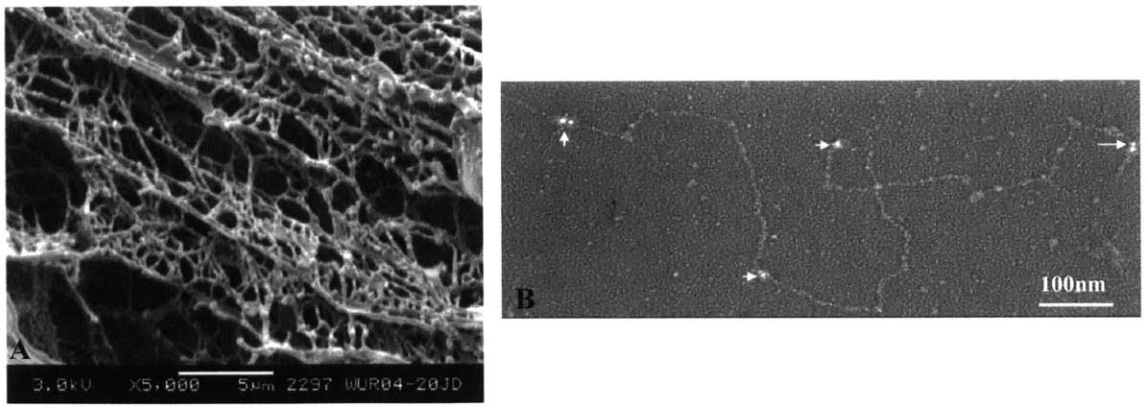

Figure 2-2: A: Detailed image of the mucin network from a Cryo-SEM image of saliva from Schipper et al [61]. B: An individual MUC5B polymer from Kesimer et al [37].

As suggested by the heavily entangled network depicted in Figure 2-2 A, mucin interactions also

play a large role in contributing to the viscoelasticity of saliva [72, 61]. Although the heavy glycosylation of the mucins is thought to inhibit any disulfide bond crosslinking , the long, linear MUC5B chains undoubtedly entangle to form a network [72]. There is also evidence of additional ion-mediated interactions. By decreasing the pH of purified porcine gastric mucin solutions (PGM, to which the human mucin MUC5AC expressed in the gastic mucosa is analogous), Celli et al have shown that the viscoelasticity and gel-like nature of the solution can be increased significantly [16]. They theorize that this is due to the mucin taking on a more rod-like configuration under acidic conditions, as opposed to a more random coil at neutral pH, and a subsequent exposure of previously hidden hydrophobic regions which provide new sites for interactions [16]. Other proposed interaction mechanisms within the salivary network include carbohydrate-carbohydrate interactions and calcium-mediated crosslinks [61].

All together, this mucin network imparts saliva with unique viscoelastic properties that are essential for the many functions that it serves. The detailed rheology of saliva is the subject of the next section.

2.2 Rheological Properties

In the sections to follow, the shear rheology of saliva is discussed in the context of both Small Amplitude Oscillatory Shear (SAOS) and Steady State Shear Flow, and the extensional rheology is examined using the technique of Capillary Breakup Extensional Rheomoetry (CaBER). First, however, we provide a brief discussion of the various methods of saliva collection.

2.2.1 Saliva Collection Methods

One interesting subtlety of performing rheological measurements with saliva is the choice of the method for procurement of the sample, which is known to have a significant impact on the properties of the collected saliva despite there being limited studies in the literature that investigate this quantitatively. Stokes et al [64] study three methods: mechanical stimulation using flavour-

less gum, stimulation by citric acid, and no stimulation. Their data suggests that the viscosity of acid-stimulated saliva is highest, and that the rheological properties of unstimulated and mechanically stimulated saliva are similar [64]. In contrast, Rantonen et al [55] collected samples from 30 different subjects and found that the viscosity of stimulated saliva is lower than that of unstimulated saliva. Both studies note that the properties of saliva change from individual to individual as well as with time of day, hormonal cycle, and consumption of food and liquids [64, 55].

To test individual variation, we obtained saliva samples from two different donors. We tested time of day changes by collecting either in the early morning or early afternoon, and attempted to control for effects of food consumption by requiring donors to abstain from eating or drinking one hour prior to collection [64]. Our observations of the effect of collection method on saliva properties are not in complete agreement with either Stokes [64] or Rantonen [55]. We observed that the viscosity of saliva was relatively unaffected by collection method, donor, or time of day at collection, as is shown in Figure 2-3. However, the elasticity of saliva (discussed in detail in Section 2.2.3) was much lower for mechanically stimulated samples, and despite being relatively insensitive to collection conditions was extremely sensitive to sample age. There is no literature to the best of our knowledge on the effect of collection method of saliva on its extensional rheology, and so we believe that these findings are amongst the first of their kind in this field. This observation of decreased elasticity upon stimulation is consistent with the more serous cell-rich glands being more sensitive to stimuli, as discussed in Section 3. Since our interest was to study the degradation of the mucin network, it was therefore preferable to ensure that the collected saliva was high in mucin content.

For all data presented in this thesis, saliva was collected without stimulation according to the method described in [28]. Vacuum was drawn in a closed collection vial into which appropriately sized holes were drilled in the cap to accommodate two plastic tubes. The end of one tube was connected to a vacuum pump, and the end of the other was inserted into the mouth of the donor. Once collected, the saliva was stored and tested at room temperature. Using this procedure

allowed for reasonably consistent rheological properties across donor and time of day at collection. Although evidence suggests that freezing saliva may delay protease breakdown [23], this was not of concern to us, as the degradation and subsequent changes in rheological properties of saliva were the primary concern of this investigation.

2.2.2 Shear Rheology

All shear rheology presented in this paper was obtained using a TA Instruments (New Castle, DE, USA) stress-controlled ARG2 rheometer with a $40mm$ or $60mm$, $2°$ cone and plate fixture. The temperature was maintained at $25°C$ for all experiments using a Peltier plate.

Figure 2-3 presents SAOS data for a sample of saliva collected in the early morning and tested at various times over the course of a 24 hour period. The response was very similar for all tests performed, and so only one data set is shown for clarity. Tests were performed at 9% strain after insuring that this value was within the linear elastic range for the sample, and data for which the raw phase angle $< 175°$ is shown in order to exclude effects of instrument inertia.

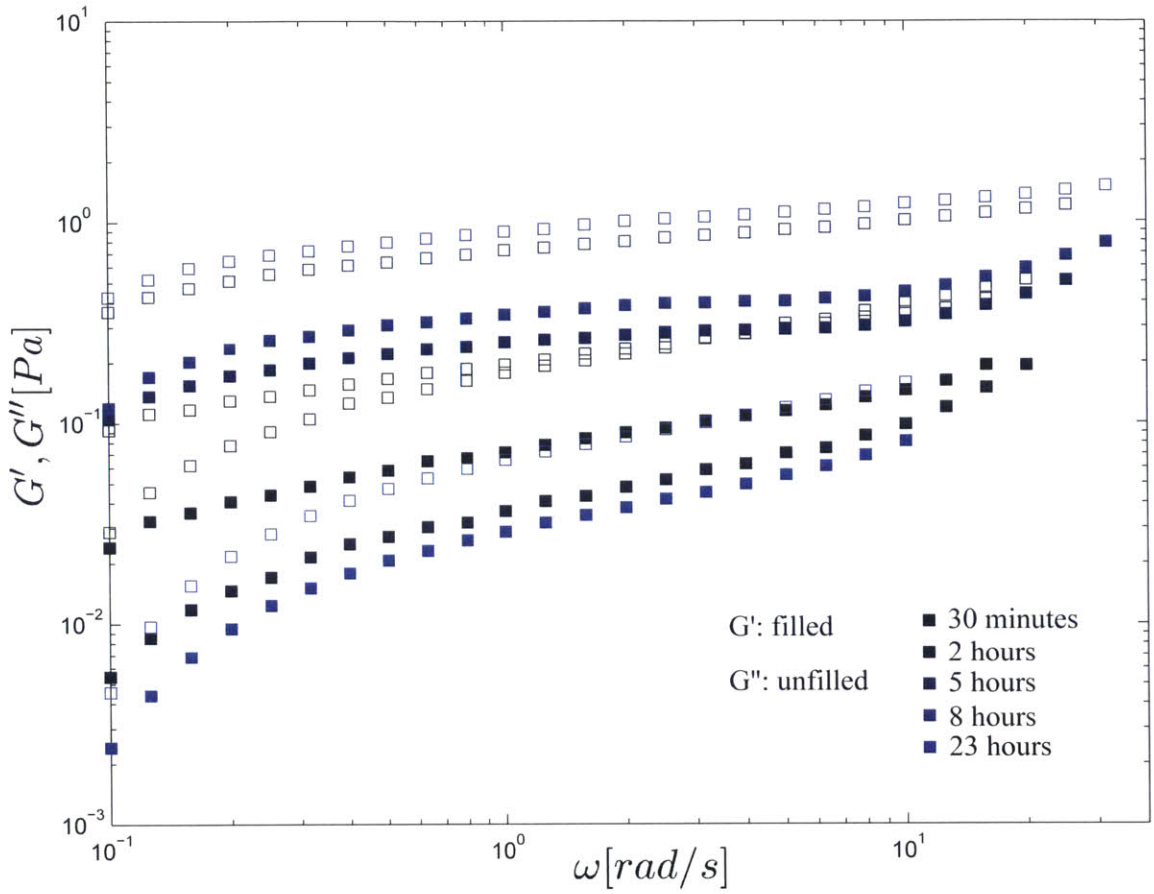

Figure 2-3: SAOS data for saliva samples at various ages

.

One immediately striking feature of the data is that the classical Maxwellian behaviour of a polymer melt or solution is not observed. Indeed the response can more appropriately be described as power-law like, which is a common feature of biological fluids as a result of the multiple relaxation modes created by the various length scales of their microstructures [33]. For all sample ages, the loss modulus G'' lies above the storage modulus G', suggesting a more fluid-like than solid-like response on the part of the sample. Less clear is the effect of age on the moduli. Although it could be expected that degradation of the chains leads to a weakening of the elastic component of the network as the sample ages, the data at 5 and 8 hours is not consistent with the trend of decreasing G'. In Section 5.4.2, when the elastic modulus is used to compute the parameters of the Rolie-Poly model for saliva, an average over several experiments is taken in order to determine an approximate form for the change of G' with sample age.

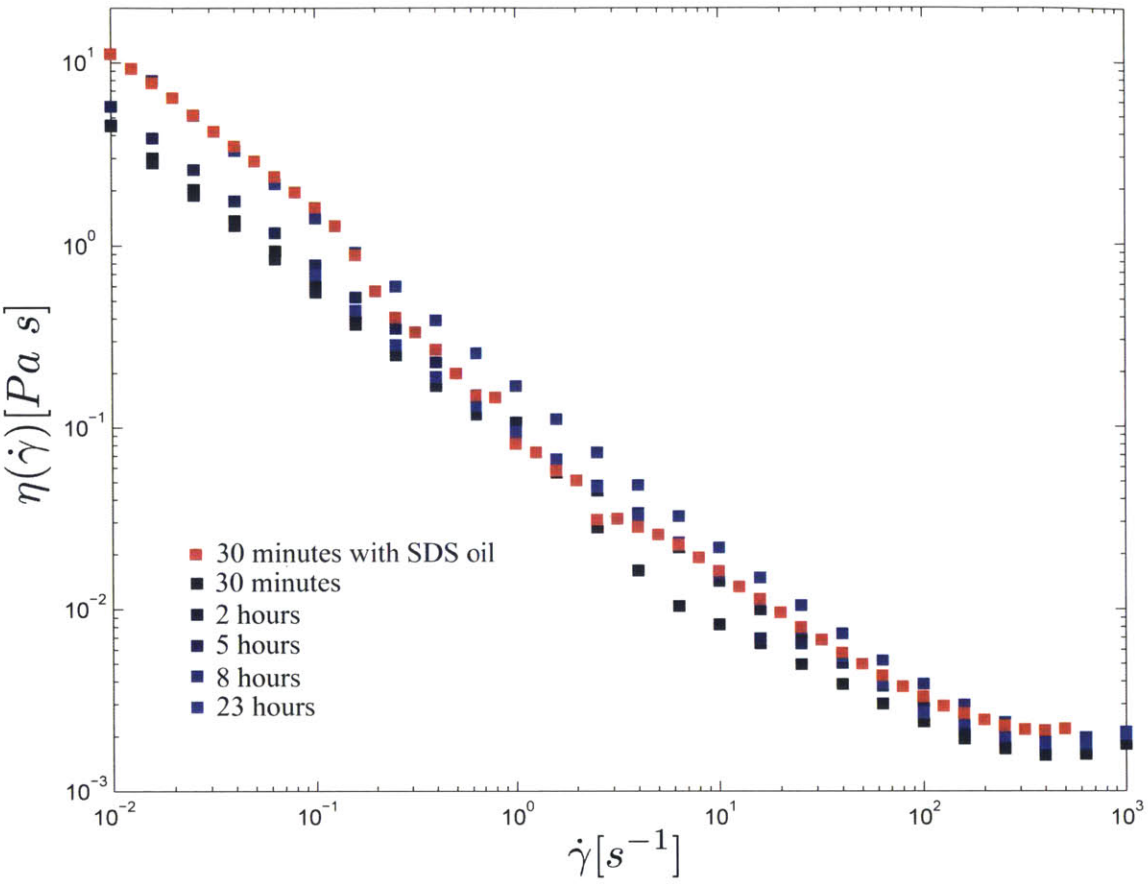

Figure 2-4: Shear viscosity data for saliva samples at various ages

In Figure 2-4, the shear viscosity as a function of shear rate is plotted for the same sample. As can be seen, saliva is quite shear thinning with a high shear rate plateau viscosity very close to that of water ($\eta_\infty \approx 0.002Pa$), but does not appear to demonstrate a zero shear plateau viscosity. Furthermore, the viscosity does not appear to be sensitive to the age of the sample.

One concern when performing rheological measurements on biological materials is the possibility of the development of a film of adsorbed protein at the solution/air interface which can affect the measurements of interest: those of the rheological properties of the bulk fluid [34, 13]. In order to evaluate whether this was affecting the observed rheological measurements, a test was run with a thin coating of SDS oil placed around the rim of the cone, eliminating direct exposure of the saliva sample to air [13]. The results of this test are shown in red in Figure 2-4, where

it is readily observed that the viscosity profile is nearly identical to the results without the SDS coating, suggesting that we are indeed measuring the bulk rheological properties of the fluid.

2.2.3 Extensional Rheology

Measurement of the viscoelasticity of saliva and other biological fluids has been of experimental interest for over a century [26, 1]. In 1908, Fano published a qualitative analysis of the spinnability of egg white, submaxillary saliva, gallbladder bile, and solutions of various plant extracts, namely from fragments of the Opuntia ficus indica leaf [26]. Although he proposed experiments to quantify the spinnability of these materials, he does not provide any experimental values in his work. In 1922, Aggazzotti performed a series of experiments on saliva that built off of the proposed experimental method of Fano [1]. Using a capillary tube, he stretched samples of saliva and measured the length at which the filaments ruptured, and used this as a measure of the spinnability, or *potere filante*, of the sample. He repeated these experiments after subjecting the saliva to various procedures such as heating, cooling, centrifugation and, most interestingly in the context of this work, simply allowing it to age. He observed that the maximum stretch length of the filament decreased as the sample aged, and that the solubility of the sample (as measured by the amount of precipitate that formed following the addition of a specified amount of acetic acid) increased. He concluded that these trends arise due to changes in the "molecular constitution of the mucin" [1].

Despite this early interest, there are very few other studies in the literature on the extensional rheology of saliva, and none apart from that by Aggazzotti [1], to the best of our knowledge, that examines the age dependence of saliva extensional properties. In terms of the literature that does exist, Haward et al studied the extensional rheology of saliva using a modified extensional flow oscillatory rheometer (EFOR)[29]: a cross-slot device that induces a local stagnation point in the flow, at which the flow velocity becomes zero but the shear rate remains significant. This causes the contained polymer chains to stretch, and the extensional viscosity can correspondingly

be measured. They observed an increase in the extensional viscosity with strain rate, up until a maximum strain rate of $\dot{\epsilon} \approx 1200s^{-1}$ at which point the extensional viscosity was observed to drop. At this strain rate, corresponding birefringence in the cross slot was also observed, suggesting flow modification along the central axis, which they attribute to possible inertial effects as well as rupture of disulphide bonds in the mucin chains [29]. Zussman and colleagues performed CaBER experiments on saliva samples obtained from patients of different age groups in order to quantify how saliva properties change between the young and the elderly as a potential explanation for why the most prevalent dental problems within these two age groups differ [78]. They found that the elasticity of saliva amongst the elderly, as measured by the relaxation time, was significantly higher than in young adults, and corresponded to a higher salivary protein content within this older age group. In general, however, a major difficulty with performing extensional rheology measurements on saliva and getting repeatable and consistent results is that saliva is unstable: the contained mucin begins to degrade over time due to protease and enzyamtic activity once the sample has been extracted from the mouth [23, 65]. Bongaerts and Stokes allude to this in their work [13, 64] but do not demonstrate how the measured viscoelastic properties are affected by this degradation.

Following the original analysis by Entov and coworkers [8, 7, 22], capillary thinning rheometry has become a standard technique for rapidly measuring the extensional properties of a wide range of viscoelastic fluids, including polymer solutions. The Capillary Breakup Extensional Rheometer (CaBER) is a commercially available instrument that is frequently used to perform these types of measurements. During the capillary thinning experiments performed in this work, a small sample of the test fluid is placed between the two rheoemter plates, each approximately $R_0 = 3mm$ in diameter and separated initially by approximately $2mm$. The plates are suddenly stretched to a final separation of approximately $9 - 10mm$ in a strike time of approximately $t_{strike} \approx 50ms$ in order to form a liquid bridge, and a laser micrometer tracks the midpoint radius of the filament as it thins under the action of capillary forces. In general for dilute polymer solutions, once fluid inertia can be neglected, the filament thinning process is initially governed by a viscocapillary

force balance in which viscous extensional stresses from the solvent oppose the increasing capillary pressure, and is followed by a later elastocapillary stage in which stresses generated by the stretching of the polymer chains dominate [48]. From measurements of the time evolution of the filament radius, the breakup time of the filament and relaxation time of the fluid can be obtained, both of which provide quantitative measures of the fluid's viscoelastic properties.

In Figure 2-5, a series of still images taken during the course of a CaBER experiment on a 30 minute old sample of saliva is shown. As is typical for more strongly elastic fluids, the assumption that the thinning filament is nearly exactly cylindrical and axisymmetric during the entire thinning process appears to be a good one [49].

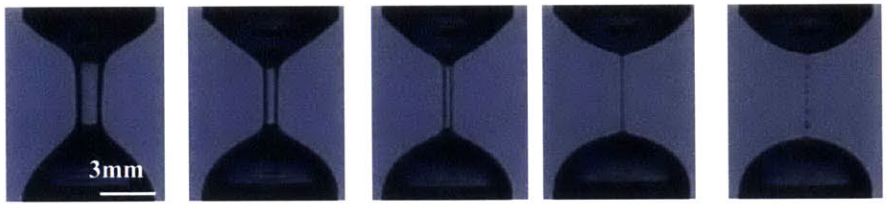

$$\frac{t - t_{strike}}{t_{break} - t_{strike}}$$

0 0.17 0.33 0.66 1

Figure 2-5: Still images at various stages of filament thinning during a capillary breakup extensional rheometry (CaBER) experiment with a sample of 30 minute old saliva.

In Figure 2-6, the results of Figure 2-5 are translated into plots of the nondimensional radius ξ as a function of time t for the saliva samples at various ages. Data is only shown for times later than the strike time (when the plates have reached their final separation height), and is normalized by the radius of the filament at the strike time. It is immediately apparent that the time to breakup of the filaments and the relaxation time of the samples decrease as the age of the saliva increases. As will be explained in detail in Section 4.4 the relaxation time is in general obtained from CaBER data by fitting a curve proportional to $\exp\left(-\frac{t}{3\lambda_H}\right)$ through the section of the radius evolution which follows an exponential decay; a signature of the elasto-capillary regime.

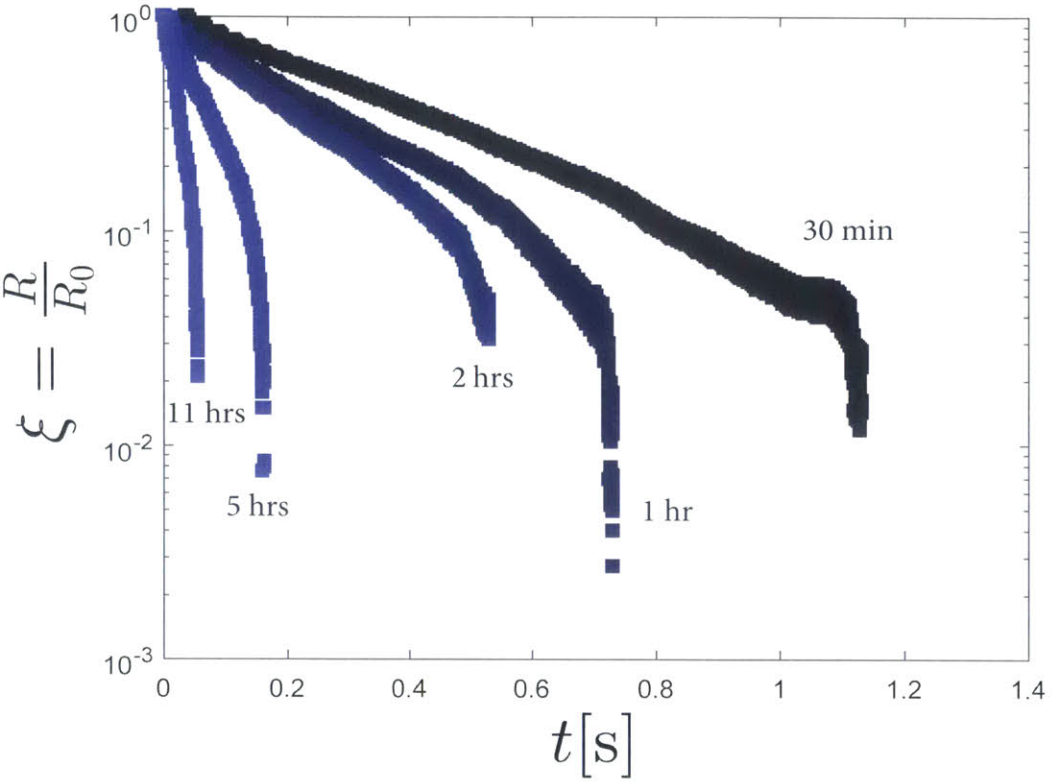

Figure 2-6: CaBER data of filament midpoint radius for saliva samples at various ages

.

In Figure 2-7, the measured average relaxation times λ_H with standard deviations are shown as a function as the age of the saliva sample. Data is shown for two different donors as an indicator of individual specimen variations, as well as for samples of saliva collected early in the morning and in the afternoon in order to be indicative of the effects of diurnal cycles on saliva properties. Although there is undoubtedly variation between samples, the overall trend of decreasing relaxation time with age is very apparent.

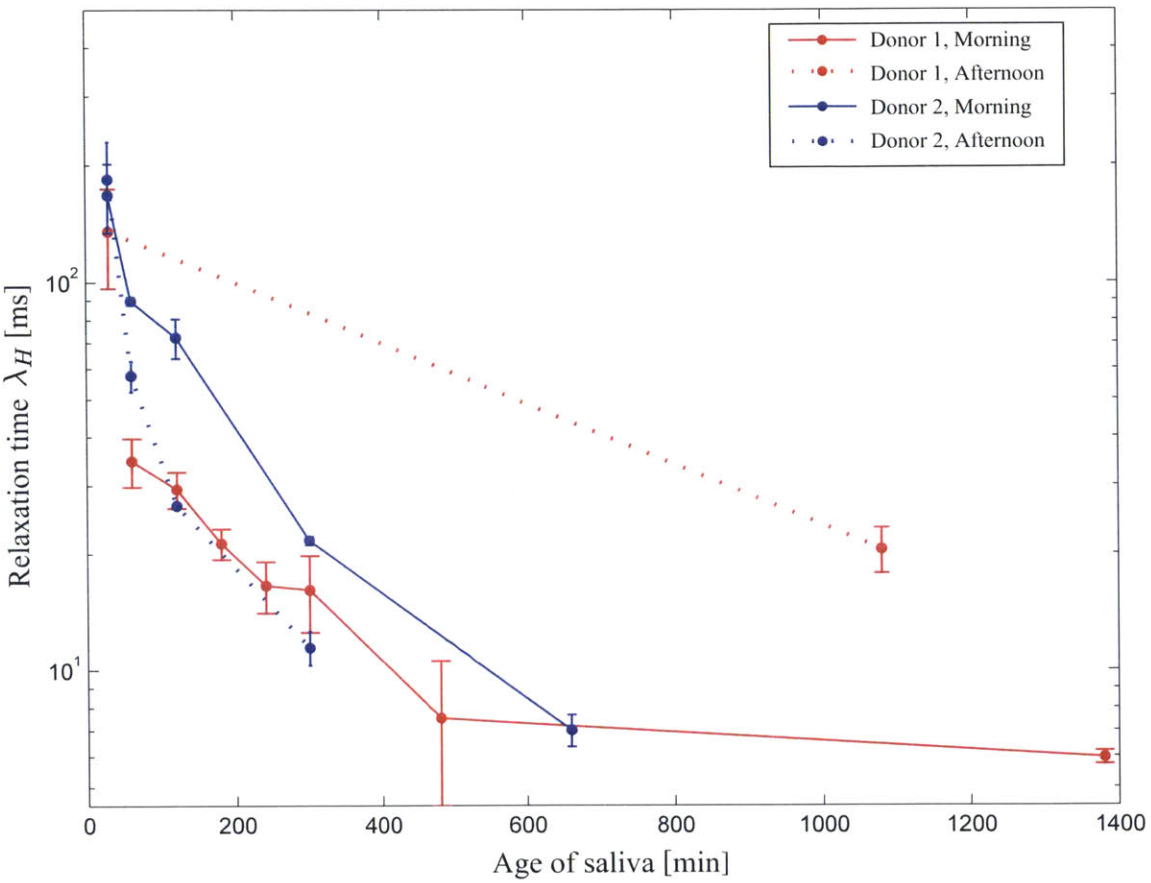

Figure 2-7: Average relaxation time of saliva samples as a function of their age for two different donors. Data is shown for saliva collected in the morning and the afternoon to demonstrate cyclical changes in properties

.

These results clearly suggest that the microstructure of the saliva is being modified as the sample ages, as suggested by Aggazzotti nearly a century ago [1]. Indeed, it is known that protease and enzymatic activity can cause salivary mucins to degrade with time [23, 65]. Therefore, the remainder of this thesis is devoted to the development of polymer models that can account for these changes in microstructure, and reproduce these experimentally observed macro-scale rheological findings under conditions of simple elongational flow. However, before exploring this topic, we provide a brief discussion of the development of substitute or analogue saliva fluids that possess comparable rheological properties to human saliva. These fluids present tremendous potential gains both for patients suffering from a wide range of diseases, and for biological experimentation and research.

2.3 Development of Saliva Substitute Fluids

2.3.1 Motivation

The need for the development of substitute saliva fluids for patients suffering from 'dry-mouth' or xerostomia has been recognized for over a century [27] as a result of the essential roles that saliva plays in the ability to speak, swallow, maintain oral health, and much more (see Section 3). The aetiology of salivary dysfunction is diverse, and can result either from diminished levels of salivation or structural damage to the salivary glands [27]. Certain clinical conditions such as anxiety and depression are known to decrease salivation, as well as some medications (particularly some tricyclic antidepressants)[27]. Furthermore, structural damage to the salivary glands arises due to some autoimmune diseases such as Sjörgen's syndrome which targets and destroys glands in the body, as well as diabetes and its associated neuropathies [27, 29]. Chemotherapy and radiotherapy treatments for cancers of the head and neck, although potentially helpful at eliminating cancerous cells, can also have the unfortunate effect of destroying the salivary glands [27].

Additionally, as explained earlier in this section, there is ongoing research related to epidemiology of respiratory diseases, for which the study of the fragmentation process of saliva during a cough or sneeze is of the utmost interest [14, 6, 76]. Since obtaining large quantities of saliva for such experiments is often not feasible, having a synthetic substitute with similar rheological properties would be extremely advantageous from an experimental point of view. In particular, it is desired rheologically-speaking that an appropriate saliva substitute should possess a similar shear viscosity profile to saliva (in the same numerical range and shear thinning), as well as comparable elasticity as measured through its relaxation time and filament radius evolution profile under the conditions of simple elongational flow during a CaBER experiment.

Clearly, there are other criteria beyond the matching of rheological properties which must be met when developing a substitute saliva to administer to patients (such as biological and dental compatibility). However, given the detailed rheological characterization of saliva that was performed

for this thesis, thought has been placed into finding suitable biopolymer solutions which could, at least from an experimental point of view, be used as substitutes for saliva. Although this is not intended to be a fully comprehensive discussion, the results found are promising that such a fluid can be found.

2.3.2 Current Technologies

Although some attempts have been made to develop saliva substitutes using animal mucins such as those extracted from bovine salivary glands, as was the case with reconstituted solutions of human salivary mucins [56], these solutions often do not yield the same viscoelastic properties as the saliva in its original form [27]. As a result, many of the products on the market today are biopolymer based, with Xanthan gum (eg. used in the product Xialine) and carboxymethylcellulose (eg. used in the product Saliveze) being two of the most popular biopolymers used [54, 27].

We therefore selected Xanthan gum (obtained from Sigma Aldrich, Saint-Louis MO) as a first biopolymer candidate in the development of a rheologically appropriate saliva substitute. Solutions of $0.05wt\%$ Xanthan gum in DI water were found to reproduce the shear viscosity profile of saliva quite well, as seen in Figure 2-8. The shear thinning behaviour is well captured, and the viscosity values obtained are very close to those of saliva, particularly at higher shear rates.

When CaBER was performed with the same $0.05wt\%$ solution of Xanthan gum, filament formation was impossible, meaning that the solution was nearly inelastic. In an attempt to reproduce the elasticity of saliva, $2 \times 10^6 g/mol$ MW polyethylene oxide (PEO) (obtained from Sigma Aldrich, Saint-Louis MO) was added to the Xanthan gum solution at various concentrations. It should be noted that there is some precedent in the literature for the addition of polymeric materials to saliva substitutes in order to enhance their rheological properties, an example being Preetha et al who added phosphatidylethanolamine (PE) to the substitute Saliveze [54].

Three different concentrations of PEO ($0.05wt\%$, $0.3wt\%$, and $1.5wt\%$) were added to the $0.05wt\%$ Xanthan gum solution, and relaxation times were obtained using CaBER. In order to reproduce the elasticity of young saliva (less than one hour old), it was required that the PEO/Xanthan solution have a relaxation time of approximately $50ms$ (see Figure 2-7). In Figure 2-8, the shear viscosity profiles and relaxation times of all three PEO/Xanthan solutions are presented, along with the shear viscosity profiles of the pure Xanthan solution and saliva. As can be seen, although the highest concentration PEO solution was sufficiently elastic, the addition of such large quantities of PEO had the deleterious effect of increasing the viscosity of the solution by more than an order of magnitude at all shear rates tested.

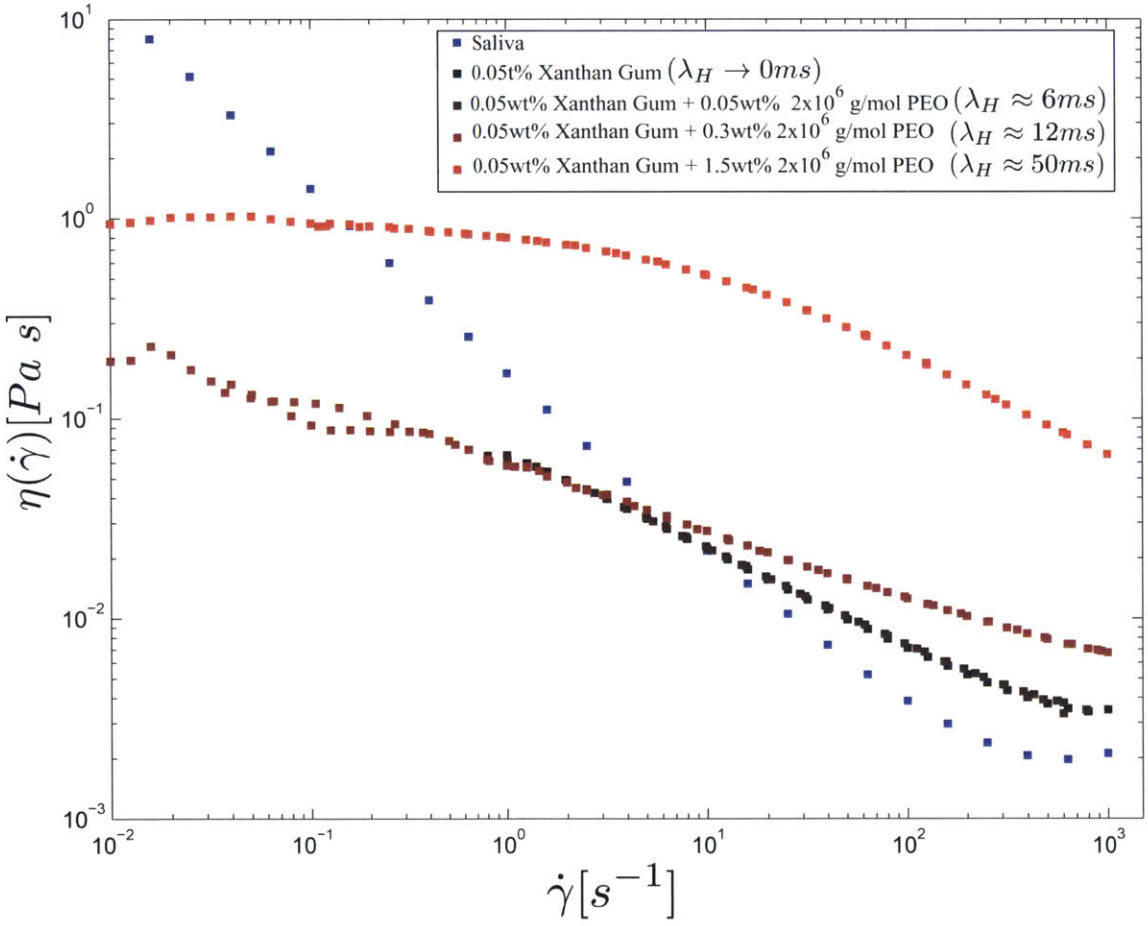

Figure 2-8: Shear viscosity data for saliva and $0.05wt\%$ xanthan gum solutions with various amounts of 2×10^6 g/mol MW PEO

Therefore, although the shear viscosity profiles of Xanthan gum solutions can be very similar

to those of saliva at the appropriate concentrations, the inability to produce a suitably viscous and elastic solution using easily obtained synthetic polymers (such as PEO) made this approach undesirable. We subsequently attempted to find a biopolymer with intrinsic viscoelasticity in order to eliminate the need to enhance elasticity using synthetic polymers. Two candidates: Mamaku gum and flax seed extract were found to be quite suitable, and details of the preparation and rheological properties of these solutions are presented in the next subsections.

2.3.3 Novel Biopolymer Solutions

2.3.3.1 Flax Seed Extract

Following interesting discussions with Oswaldo Oliva and the other head chefs at the Michelin star rated restaurant Mugaritz in Guipúzcoa, Spain, it was suggested that a solution of flax seed extract could be a suitable analogue fluid for saliva. Indeed, flax seed extract is often used in vegan cooking as a substitute for egg whites as a result of its similar consistency.

The component of the flax seed extract responsible for imparting the desired viscoelastic properties is the mucillage [77]. The mucillage is composed of a mixture of of neutral arabinoxylans and acidic rhamnose-containing polysaccharides at a ratio of approximately 1:0.7, and makes up approximately 6.5% by weight of the flax seeds [77]. The neutral polysaccharide arabinoxylan is the main polysaccharide contained in the mucillage (approximately 75%)[77]. Structurally, arabinoxylan contains a uniform arabinose: xylose ratio of 0.24, along with varying galactose and fucose residues in its sidechain [77]. Its molecular weight is approximately $1.2 \times 10^6 g/mol$ [77].

Following 'Stage 1' of the extraction procedure outlined by Ziolkovska [77], 3g of whole flax seeds (obtained from a local Whole Foods grocery store) were combined with 75 mL of DI water and stirred using a magnetic stirrer on a hot plate at 300rpm and $80°C$ for 30 minutes. Once cool, the supernatant solution was separated from the seeds, and diluted to a ratio of 5mL flax seed extract: 7mL of DI water. Assuming that 50% of solids are extracted from the seeds following this Stage 1 extraction as reported by Ziolkovska [77], it was therefore estimated that the final

flax seed extract solution had a mucillage concentration of approximately $c = 0.054g/L$. To date, no thermogravimetric analyses (TGA) have been performed to verify this concentration. It is additionally likely that other seed components, such as flax seed oil, were also extracted in the process. Regardless, this first attempt at an extraction yielded a suitable fluid which resembled saliva qualitatively, and with which rheological measurements could be performed.

2.3.3.2 Mamaku Gum

The second novel biopolymer considered was Mamaku gum. Mamaku gum is extracted from the fronds of the black fern tree and has traditionally been used by the Maori tribes of New Zealand for the treatment of boils, burns, wounds, rashes, and diarrhea [35]. The shear and extensional rheology of Mamaku gum has been characterized extensively elsewhere by Jaishankar et al [35].

A sample of unpurified dried Mamaku gum was kindly obtained from collaborators at Massey University in New Zealand. A $2.5wt\%$ solution of Mamaku gum was prepared using DI water, and was combined using a magnetic stirrer at 300rpm for approximately 5 hours until the solution looked entirely homogeneous.

2.3.3.3 Rheological Comparison with Saliva

In Figure 2-9, the shear viscosity profiles of 30 minute old saliva as well as the flax seed and Mamaku gum solutions described above are compared.

Although to a lesser degree than saliva, the flax seed solution is also shear thinning, although significantly more viscous at high shear rates ($\dot{\gamma} > 1s^{-1}$) than saliva. The $2.5wt\%$ Mamaku gum solution is only moderately shear thinning, and in fact exhibits a range of shear thickening behaviour between shear rates of approximately $40s^{-1} < \dot{\gamma} < 70s^{-1}$. This behaviour is well documented in [35], and is believed to arise as a result of unfolding of the polymer chains due to the imposed shear flow, which exposes more previously hidden sites that permit hydrogen bonding between the chains.

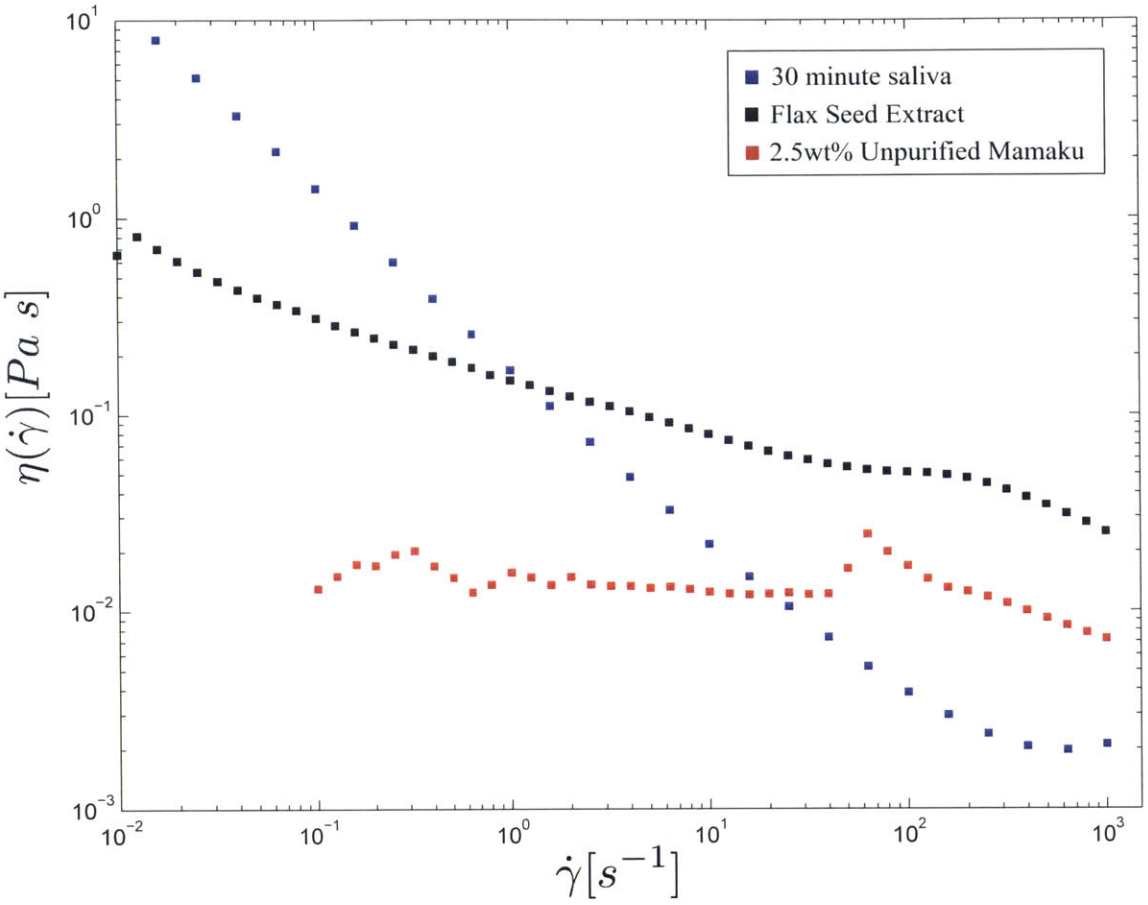

Figure 2-9: Shear viscosity comparison of saliva, flax seed extract, and $2.5wt\%$ unpurified Mamaku gum

In Figure 2-10, SAOS data is presented for the same fluids with the % strain indicated, determined for each sample to lie within the linear elastic range. For all three fluids over the entire testable frequency range (save the highest frequencies in the case of the Mamaku gum solution), the loss modulus G'' exceeds the storage modulus G'. Furthermore, as previously mentioned, all three fluids exhibit a distinct power-law like response of the moduli, which has been well documented in biopolymer solutions [33].

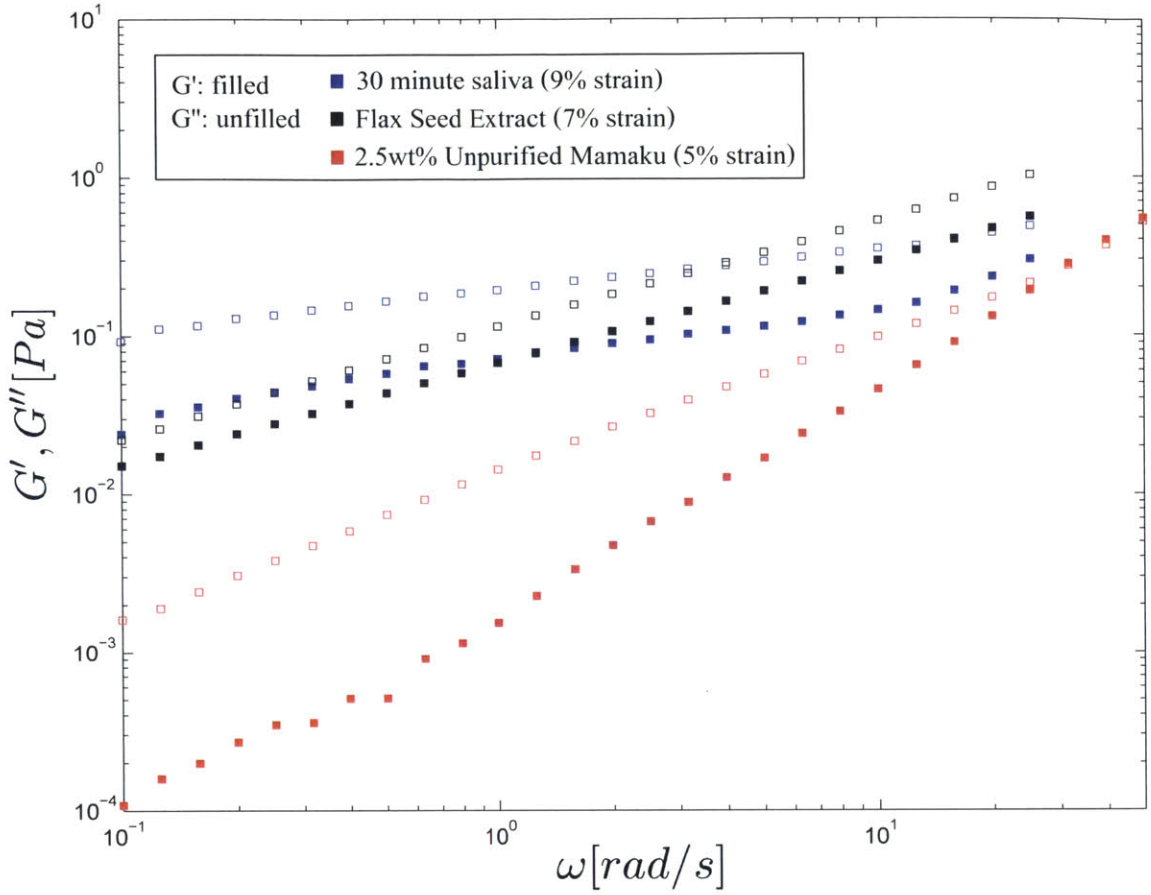

Figure 2-10: SAOS comparison of saliva, flax seed extract, and $2.5wt\%$ unpurified Mamaku gum

Finally, in Figure 2-11, CaBER data is shown for the $2.5wt\%$ Mamaku gum solution, the flax seed solution, and saliva at two ages (30 minutes and 1 hour). The relaxation times λ_H are shown in the figure, and additionally the average relaxation time for all runs performed of the Mamaku gum and flax seed solutions are reported. For the Mamaku gum solution, consistent and reproduceable CaBER data was obtained (and evidenced by the small disparity between the relaxation time for the run shown and the average value obtained). Conversely, it was difficult to obtain consistent CaBER data for the flax seed solution. As a result, there is significant disparity amongst the breakup time results and relaxation time values for the different runs performed. It is believed that this could be due to inhomogeneity within the solution as created thus far. In future, centrifugation and prolonged mixing could be attempted in order to eliminate this variability. We therefore report two characteristic CaBER runs for the flax seed solution in Figure 2-11 in order

to be more indicative of the range of behaviours observed.

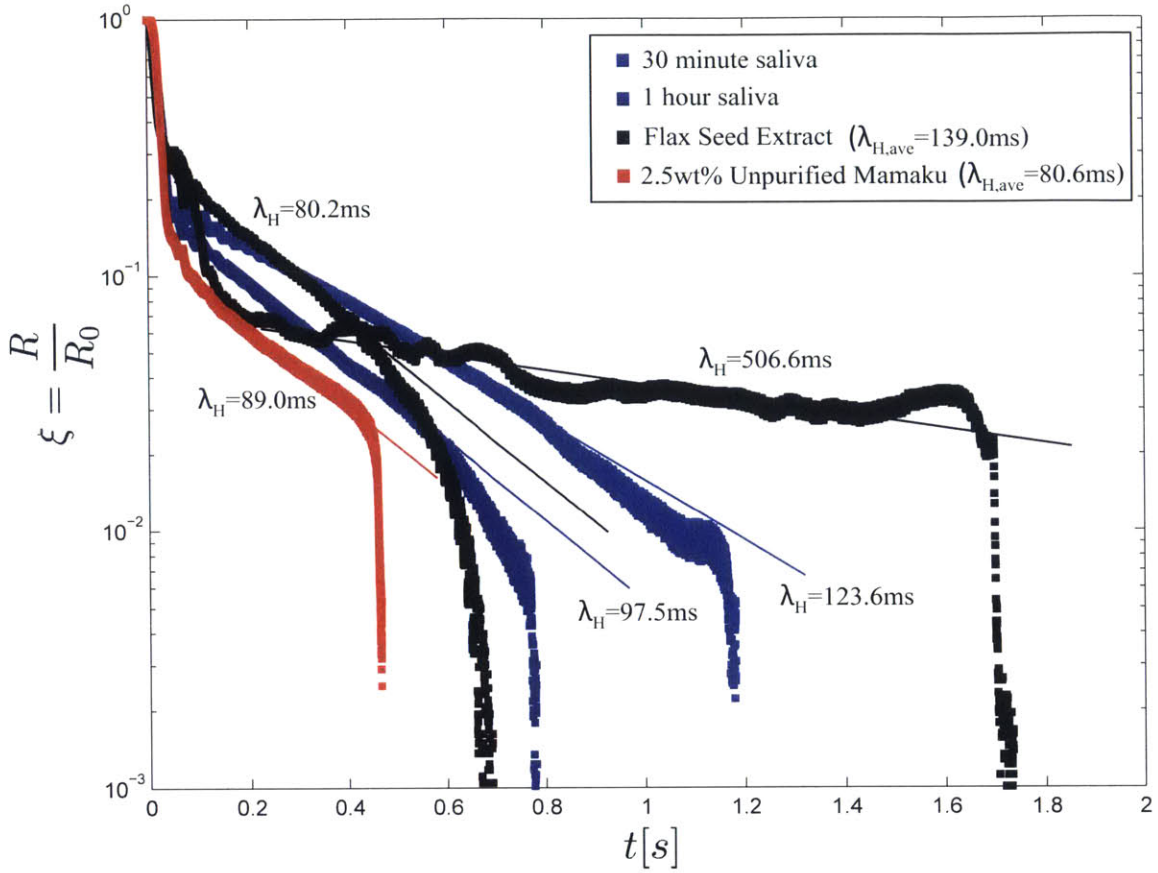

Figure 2-11: CaBER comparison of saliva, flax seed extract, and $2.5wt\%$ unpurified Mamaku gum with relaxation times indicated

Encouragingly, both the Mamaku gum and flax seed solutions were comparably viscoelastic to young saliva (less than one hour old), as can readily be seen in Figure 2-11 by the comparable times to breakup and relaxation times of the samples. The viscoelasticity of the $2.5wt\%$ Mamaku gum solution was found to be very comparable to that of one hour old saliva, which would make it a promising candidate for use in experiments for which relatively fresh saliva samples are desired. The flax seed solution on one run was comparably viscoelastic to one hour old saliva, and then on additional runs demonstrated very large relaxation times ($\lambda_H \approx 500ms$) and filament breakup times. These results are nevertheless encouraging, and suggest that with appropriate homogenization and dilution, flax seed solutions could also be very suitable candidates for a substitute saliva

fluid.

Chapter 3

Determination of molecular modeling properties for MUC5B mucin

Before proceeding to the various models used to simulate the behaviour of saliva under simple elongational flow conditions, it is useful to carefully detail the steps by which the molecular parameters of the mucin used in the various models were determined.

We model the MUC5B mucins (the biological properties of which have been described in Section 3 as bead spring chain polymers, following the method of Bird et al [10]. In Figure 3-1, a representative segment of molecular weight MW of a MUC5B chain is shown, taken from Bansil and Turner [5]. In the FENE-P model, this segment is taken to be the entire mucin chain, while in the Rolie-Poly-FENE-P and Sticky Network models, it is taken to be an entanglement segment (M_e instead of MW).

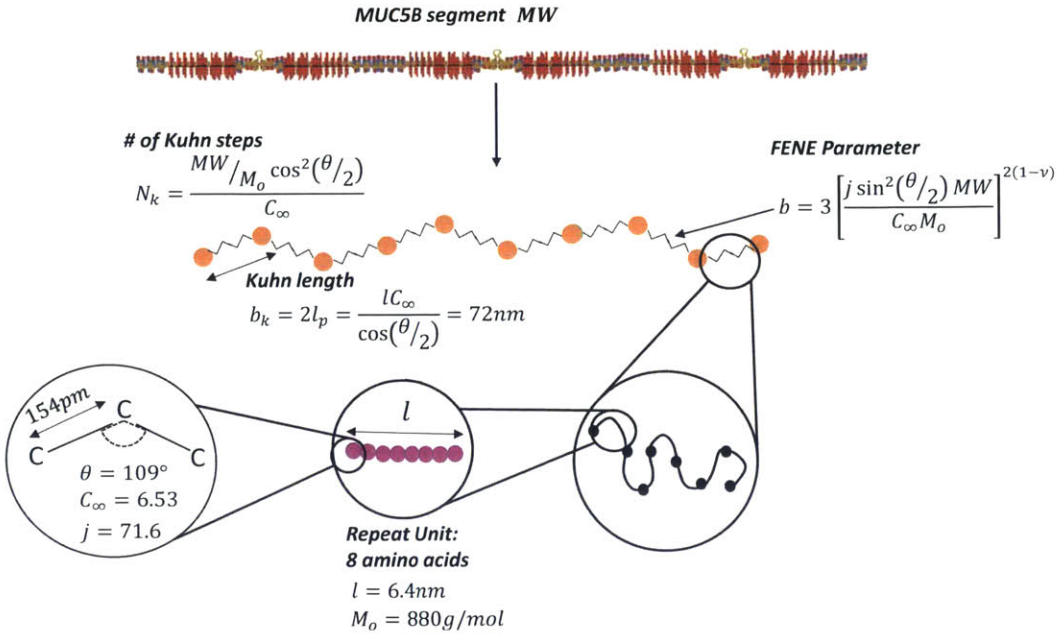

Figure 3-1: Detailed description of the method of determination of the model parameters for MUC5B from physiological properties.

The repeat unit of MUC5B mucin is estimated to be around 8 amino acids in length, as reported by Inatomi et al in human MUC5AC mucin (genetically very similar to MUC5B) [32]. Using standard values for the molecular weight and size of an amino acid, we can approximate the length l and molecular weight M_o of a repeat unit to be $l = 6.4nm$ and $M_o = 880\frac{g}{mol}$.

The persistence length of mucin has been estimated by Round et al for ocular mucins as approximately $l_p = 36nm$ [58]. From this result, we obtain an estimate for the Kuhn length between adjacent beads in the chain as

$$b_k = 2l_p = 72nm.$$

Additionally, from the definition of the Kuhn length [67]

$$b_k = \frac{lC_\infty}{cos\left(\frac{\theta}{2}\right)} \tag{3.1}$$

we can obtain an estimate for the characteristic ratio for MUC5B as $C_\infty \approx 6.53$, where θ is the carbon-carbon bond angle in the chain back bone $\theta = 109°$.

With the characteristic ratio determined, it is possible to evaluate the number of Kuhn steps (or spring segments in the chain) [67]

$$N_k = \frac{\frac{MW}{M_o} cos^2\left(\frac{\theta}{2}\right)}{C_\infty}. \tag{3.2}$$

Finally, we calculate the finite extensibility of the mucin segment in question by making use of the equation [18]

$$b = 3\left[\frac{jsin^2\left(\frac{\theta}{2}\right) MW}{C_\infty M_o}\right]^{2(1-\nu)}, \tag{3.3}$$

where j is the number of carbon-carbon bonds in the repeat unit and ν is the Flory exponent, estimated as $\nu = 0.6$ for a good solvent.

With these definitions established, we proceed to the details of the models considered in this work.

Chapter 4

The FENE-P model

The first attempt made at simulating the behaviour of saliva under CaBER conditions was to model saliva as a Finitely Extensible Nonlinear Elastic (FENE) fluid. This section outlines the details of this modelling, and in particular highlights the composite analytic solution that was developed [73].

4.1 Motivation

Entov and Hinch [22] provide a full numerical solution for the evolution in the radius of a filament of a FENE fluid undergoing uniaxial elongational flow during elastocapillary thinning. The FENE model for a polymer solution assumes a Newtonian solvent containing a dilute suspension of polymer chains that are modelled as finitely extensible (with maximum extensibility b) and non-linearly elastic. To date, CaBER analysis has typically consisted of experimental measurement and comparison with numerical simulations of filament thinning using the FENE model. Select examples include Liang and Mackley [44], who studied the concentration-dependent relaxation times of polyisobutylene (PIB) solutions, as well as Anna [2, 3] and Clasen and coworkers [18], who studied the dynamics of elastocapillary thinning in various concentrations and molecular weights of polystyrene-based Boger fluids and compared their results with numerical simulations of the FENE model to determine the effective elongational relaxation time.

As a result of the continued interest in capillary thinning rheometry, it would be useful to have an analytic solution that gives the finite time to breakup and describes the evolution in the mid-filament radius $R(t)$ as one varies the concentration, molecular weight, or solvent viscosity of a polymer solution. Recently, Torres and coworkers [66] developed an exact implicit analytic solution for the finite time to breakup and time evolution of the radius for a Giesekus fluid undergoing capillary-driven thinning. They studied semi-dilute and concentrated guar gum solutions, and because of the very viscous nature of these entangled systems, their analytic model for the forces acting on the filament was able to neglect the contributions of solvent viscosity with negligible consequence. Many biological fluids, however, are dilute polymer solutions, and in this concentration regime, the solvent viscosity is known to play an important role in the overall extensional stress response, particularly at early times [48]. Motivated by these developments, we analyse the elastocapillary thinning of a filament of a Finitely Extensible Nonlinear Elastic (FENE) fluid, paying special attention to the different phases of the process including the initial solvent response, the intermediate elastic regime when the chains are partially stretched, and the ultimate approach to maximum extensibility as the polymer chains become fully stretched.

We begin by revisiting the derivation of the FENE-P constitutive equation (where the -P indicates the Peterlin approximation) in several different forms, from which we derive an analytic expression for the time evolution of the mid-filament radius $R(t)$. Using this result, we can then determine the finite time to breakup when the polymer stress contribution is considered in isolation of the viscous solvent response. We subsequently consider the special limit of infinite extensibility, and show via comparison with the corresponding result from Entov and Hinch [22] how the solvent viscosity must be explicitly accounted for. We ultimately present a composite analytic solution, which incorporates both an initial viscous-dominated phase and a later polymer-dominated phase. We explore the level of extensional strain at which the transition from a viscocapillary to elastocapillary balance occurs. For real fluids, the viscous phase can be followed by either an intermediate elastic phase or by transition directly to the fully stretched FENE phase depending on the magnitude of the finite chain extensibility b. We conclude by comparing the finite breakup times predicted

from the numerical and composite analytic results as the molecular extensibility of the chains varies, and show how these predictions compare with those from Entov and Hinch [22] when the extensibility parameter b becomes very large.

4.2 Definitions and derivations

In what follows, we consider a cylindrical filament of initial radius R_0, consisting of a dilute polymer solution with solvent viscosity η_s, surface tension σ, at temperature T, containing polymer chains of number density n and molecular weight M_W. The polymer chains are modelled as finitely extensible dumbbells with spring constant H, and fully stretched chain length Q_0. The finite extensibility parameter, related to the ratio between the fully stretched length and equilibrium coil size, is defined as $b = \frac{3Q_0^2}{\langle Q^2 \rangle_{eq}} = \frac{HQ_0^2}{kT}$, where k is the Boltzmann constant and $\langle Q^2 \rangle_{eq}$ is the equilibrium mean square size of the chain. The characteristic relaxation time of the dumbbell is defined as $\lambda_H = \frac{\zeta}{4H}$, where ζ is the Langevin friction coefficient of the beads [12].

In real solutions, the finite extensibility parameter and the relaxation time are related to the molecular weight and the solvent quality through scalings of the form $b \sim M_W^{1-\nu}$, and $\lambda_H \sim M_W^{3\nu}$ respectively, where ν, the excluded volume coefficient characterizing the quality of the solvent, is in the range $0.5 \leq \nu \leq 0.6$ [18]. However, for what follows in this work, in keeping with the approach of Entov and Hinch [22], we treat the relaxation time λ_H and the finite extensibility parameter b as independent variables. Later work will focus on reconciling these parameters with changes in actual molecular structure of the polymer chains, e.g. due to oxidative or mechanical degradation.

4.2.1 Derivation of the Bird form of the FENE-P constitutive equation

We begin by deriving the FENE-P constitutive equation as is detailed in [12] by Bird et al. The force in a FENE dumbbell as a function of the dumbbell stretch is given by

$$\boldsymbol{F} = \frac{H\boldsymbol{Q}}{1 - \frac{Q^2}{Q_0^2}}, \tag{4.1}$$

where $\mathbf{Q}$ is the connector vector (of magnitude Q) between the two ends of the dumbbell of maximum extension Q_0.

The Kramer's expression for the polymer contribution to the stress tensor can then be written as

$$\boldsymbol{\tau}_p = -n \langle \boldsymbol{QF} \rangle + nkT\boldsymbol{\delta} = -nH \left\langle \frac{\mathbf{QQ}}{1 - \frac{Q^2}{Q_0^2}} \right\rangle + nkT\boldsymbol{\delta}, \tag{4.2}$$

where $\langle . \rangle$ indicates an ensemble average over all dumbbells.

In order to find a closed form solution to this equation, Peterlin suggested the use of the approximation $\left(\frac{\langle Q^2 \rangle}{\langle Q_0^2 \rangle} \equiv \left\langle \frac{Q^2}{Q_0^2} \right\rangle \right)$ [53], from which we arrive at the final form of the Kramer's polymer stress tensor equation

$$\boldsymbol{\tau}_p = -nH \frac{\langle \mathbf{QQ} \rangle}{1 - \left\langle \frac{Q^2}{Q_0^2} \right\rangle} + nkT\boldsymbol{\delta}. \tag{4.3}$$

Similarly, the Giesekus expression for the polymer stress tensor for Hookean dumbbells is given by

$$\boldsymbol{\tau}_p = \frac{n\zeta}{4} \langle \mathbf{QQ} \rangle_{(1)} \tag{4.4}$$

where the subscript (1) denotes the upper convected derivative of the tensor, defined in [12] for a representative tensor $\boldsymbol{\tau}$ as

$$\boldsymbol{\tau}_{(1)} = \frac{D}{Dt}\boldsymbol{\tau} - \{(\boldsymbol{\nabla v})^T \cdot \boldsymbol{\tau} + \boldsymbol{\tau} \cdot (\boldsymbol{\nabla v})\} \tag{4.5}$$

where $\boldsymbol{v}$ is the velocity vector.

To develop a closed-form expression for the stress tensor, we need to eliminate the microscopic

variable $\langle \mathbf{QQ} \rangle$ and its invariants such as $tr\langle \mathbf{QQ} \rangle$, where by definition $tr\langle \mathbf{QQ} \rangle \equiv \langle Q^2 \rangle$. Taking the trace of Eq. (4.3), it can readily be shown after some algebraic manipulation that we can rewrite the FENE term in the form of a new parameter, f:

$$\frac{1}{1 - \left\langle \frac{Q^2}{Q_0^2} \right\rangle} = f = 1 + \frac{3}{b}\left(1 - \frac{tr(\boldsymbol{\tau}_p)}{3nkT}\right). \tag{4.6}$$

Using this new parameter, we can rewrite the Kramers stress tensor in Eq. (4.3) as

$$\boldsymbol{\tau}_p = -nHf\langle \mathbf{QQ} \rangle + nkT\boldsymbol{\delta}. \tag{4.7}$$

Finally, by taking the upper convected derivative of Eq. (4.7) and combining it with the Giesekus expression in Eq. (4.4), the constitutive relation for the stress tensor in a dilute suspension of FENE-P dumbbells can be found to be

$$f\boldsymbol{\tau}_p + \lambda_H \boldsymbol{\tau}_{p_{(1)}} - \lambda_H \left[\boldsymbol{\tau}_p - nkT\boldsymbol{\delta}\right] \frac{D \ln f}{Dt} = -nKfT\lambda_H \dot{\boldsymbol{\gamma}}. \tag{4.8}$$

where $\boldsymbol{\tau}_p$ is the polymer stress tensor, f is the FENE term defined as

$$f = 1 + \frac{3}{b}\left(1 - \frac{tr(\boldsymbol{\tau}_p)}{3nkT}\right), \tag{4.9}$$

$\dot{\boldsymbol{\gamma}}$ is the symmetric rate of strain tensor and $\boldsymbol{\delta}$ is the unit tensor. This is the form considered by Bird et al [11] which we later use to derive our analytic result.

The dynamics of the problem as well as the governing force balance are specified by assuming a time-varying and axisymmetric uniaxial elongational flow ($v_r = -\frac{1}{2}\dot{\epsilon}(t)r, v_z = \dot{\epsilon}(t)z$) in a cylindrical filament of radius $R(t)$, from which it follows that the time-varying strain rate is given by

$$\dot{\epsilon}(t) = -\frac{2}{R}\frac{dR}{dt}. \tag{4.10}$$

Combining the force balances in the radial and axial directions, we can eliminate the unknown pressure inside the thinning filament and obtain the following force balance in which the capillary

stress is balanced by a combination of the viscous extensional stress difference and the polymer stress difference:

$$\frac{\sigma}{R} = 3\eta_s\dot{\epsilon} - (\tau_{zz} - \tau_{rr}). \tag{4.11}$$

Eqs. (4.8)-(4.11) yield a closed set of equations which can be solved simultaneously in order to obtain the time evolution of the various experimentally observable variables of the problem such as the mid-filament radius $R(t)$.

4.2.2 Derivation of the Entov and Hinch form of the FENE-P constitutive equation

Additional physical insight can be gained if we express these equations in terms of the microstructural deformation tensor $\mathbf{A}$, as is done by Entov and Hinch [22], instead of the polymer stress tensor $\boldsymbol{\tau}_p$, . The dimensionless tensor $\mathbf{A}$ is related to the ensemble average of the second moment tensor, $\langle\mathbf{QQ}\rangle$ through $\mathbf{A} = \frac{\langle\mathbf{QQ}\rangle}{\frac{Q_{eq}^2}{3}}$, where $\mathbf{Q}$ is the connector vector (of magnitude Q) between the two ends of the dumbbell, and $\langle . \rangle$ indicates an ensemble average over all dumbbells. As previously stated, the equilibrium coil size is related to the fully stretched coil length through $Q_{eq}^2 = \frac{3Q_0^2}{b+3}$ [18]. The polymer stress is related to the microstructural deformation through the expression $\boldsymbol{\tau}_p = -nkT(f\boldsymbol{A} - \boldsymbol{\delta})$, where using this notation, the FENE term f can be expressed as

$$f = f(tr(\boldsymbol{A})) = \frac{1}{1 - \frac{tr(\boldsymbol{A})}{b}}. \tag{4.12}$$

Note that since b is generally quite large, we will make the approximation for all that follows that $(b + 3) \approx b$. Finally, in order to simplify the calculations to follow, we introduce the parameters $B = \frac{3}{b}$, and $G = nkT$.

By re-expressing the constitutive relation derived in the previous section using this notation, we obtain two ordinary differential equations for the radial and axial microstructural deformations

$$\dot{A_{zz}} = 2\dot{\epsilon}A_{zz} - \frac{1}{\lambda_H}(fA_{zz} - 1) \tag{4.13}$$

$$\dot{A_{rr}} = -\dot{\epsilon}A_{rr} - \frac{1}{\lambda_H}(fA_{rr} - 1). \tag{4.14}$$

In order to form a closed set of equations, we once again combine these evolution equations for the dumbbell stretch with the kinematic expression for the strain rate $\dot{\epsilon}$ given in Eq.(4.10) and the force balance from Eq.(4.11) expressed in terms of the microstructural deformation tensor:

$$\frac{\sigma}{R} = 3\eta_s\dot{\epsilon} + nkTf(A_{zz} - A_{rr}). \tag{4.15}$$

In the numerical sections of the work to follow, the coupled system of equations (Eqs. (4.13)-(4.15) in combination with Eq. (4.10)) is solved using the Matlab integration routine ode15s with real and absolute tolerances of 10^{-4} in order to obtain convergent numerical integrations of the complete equation set. The solution of the full system of equations is treated as a reference or 'exact' solution. However, we show in the following section that with a couple of additional simplifications, an analytic solution for the capillary thinning of a solution of FENE dumbbells can also be obtained.

4.3 Analytic solution

Numerical simulations suggest that after an initial phase in which the solvent viscosity is important (and which we consider in detail later in Section 4.5), the capillary pressure becomes nearly entirely balanced by the axial contribution to the polymer stress in the thinning and elongating filament. In this regime, it is justified to make two additional assumptions in order to simplify the problem further: firstly, that the radial and tangential contributions to the stress tensor are negligible; and secondly that the viscous extensional stress difference is negligible.

From Eq. (4.11), the approximate force balance becomes

$$\tau_{zz} \approx -\frac{\sigma}{R}. \tag{4.16}$$

Substituting this result, as well as that for the strain rate $\dot{\epsilon}(t)$ given in Eq. (4.10) into the constitutive equation given in Eq. (4.8) yields an ordinary differential equation for the midpoint radius R in terms of time t only.

$$\frac{\mathrm{d}R}{\mathrm{d}t}\left(-\frac{3\sigma}{R}+\left(\frac{\sigma}{R}+G\right)\frac{B\sigma}{3GR(B+1)+B\sigma}+\frac{4G}{\sigma}\right)=-\frac{1}{\lambda_H}\left(1+B\left(1+\frac{\sigma}{3GR}\right)\right) \tag{4.17}$$

At this point, it is useful to define some non-dimensional numbers in order to further simplify the equations to follow. We introduce a non-dimensional radius, $\xi = \frac{R}{R_0}$, a non-dimensional time, $\tau = \frac{t}{\lambda_H}$, and an elastocapillary number, $E_c = \frac{GR_0}{\sigma}$, which is the ratio between the elastic modulus $G = nkT$ of the dilute suspension of dumbbells and the initial capillary pressure $\frac{\sigma}{R_0}$. Following [22], we also introduce a final non-dimensional parameter to scale the relative magnitude of the solvent viscosity, $S = \frac{\eta_s}{G\lambda_H} = \frac{\eta_s}{\eta_p}$, which we discuss in detail further below. Typical ranges of these parameters for biological fluids are $\eta_s \sim 1-100\ mPa\ s$, $\lambda_H \sim 1-1000\ ms$, $E_c \sim 0.001-1$ [61], and $S \geq 1$.

Eq. (4.17) can be solved analytically, and using the initial condition that at non-dimensional time $\tau = 0$ the non-dimensional radius is $\xi = 1$, we obtain an implicit solution for the evolution of the radius with time, given by

$$\left(\frac{1}{1+E_c(b+3)}-\frac{1}{1+\xi E_c(b+3)}\right)+3\ln\left(\frac{1+\xi E_c(b+3)}{1+E_c(b+3)}\right)+4E_c\frac{(b+3)}{(b+2)}(\xi-1)=-\frac{(b+3)^2}{b(b+2)}\tau. \tag{4.18}$$

In Figure 4-1, we plot the evolution of the nondimensional radius against the nondimensional time for various values of the finite extensibility parameter, b. In keeping with the choice of Entov and Hinch, the elastocapillary number is taken to be $E_c = 0.001$ [22]. The effect of increasing b is clearly to slow down the thinning of the filament and delay the time to breakup. When b is small, the polymer chains reach their fully stretched length relatively early in the thinning process. At this point, the viscosity of the FENE fluid essentially becomes constant at a high value corre-

sponding to the steady state extensional viscosity, and the radius decays linearly in time. However, when b becomes sufficiently large, the chains continue to be able to stretch elastically and resist the increasing capillary pressure for progressively longer filament thinning times before reaching their finite extensibility limit. In the limit of $b \to \infty$, finite extensibility effects are never felt, and the Oldroyd-B solution corresponding to an exponential decrease in the radius is recovered. This limit will be explored in detail in the next section.

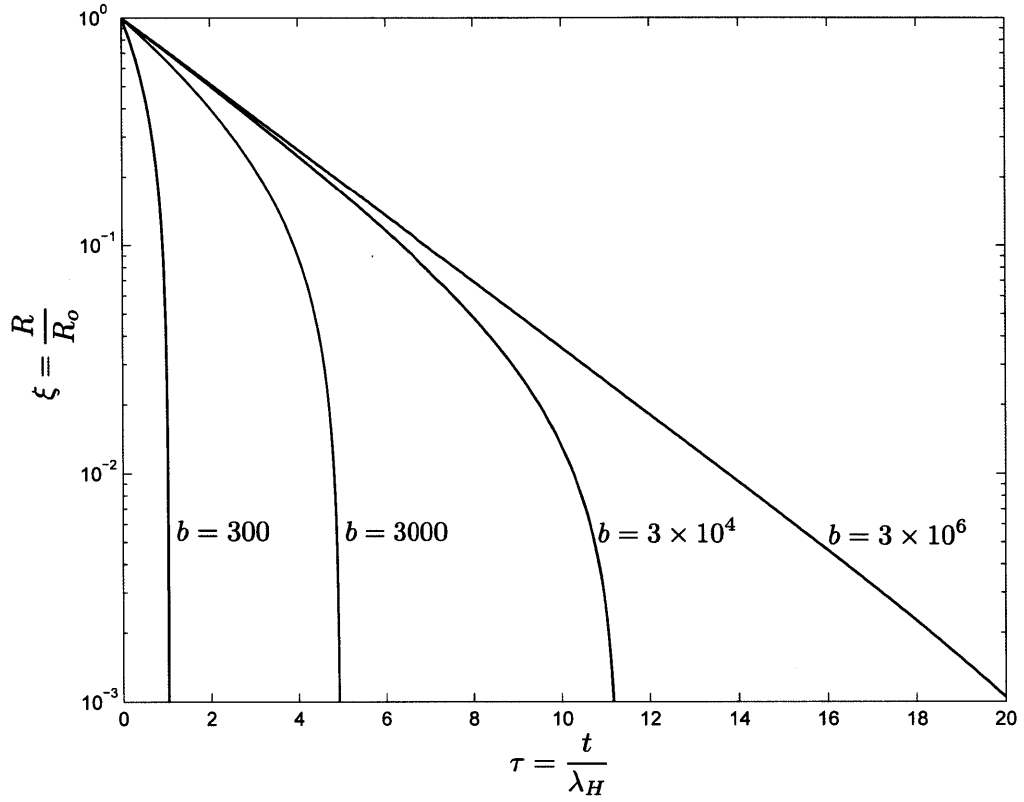

Figure 4-1: Evolution of the non-dimensional radius ξ versus non-dimensional time τ for various values of the finite extensibility parameter b with an elastocapillary number $E_c = 0.001$ and $S = 0$.

Perhaps the most useful outcome of this solution is the ability to obtain an exact analytic result for the finite time to breakup of the filament, t_{break}. By substituting $\xi = 0$ into Eq. (4.18), we obtain the following expression

$$\frac{t_{break}}{\lambda_H} = \tau_{break} = \frac{b(b+2)}{(b+3)^2}\left(\frac{E_c(b+3)}{1+E_c(b+3)} + 3\ln(1+E_c(b+3)) + 4E_c\frac{(b+3)}{(b+2)}\right). \tag{4.19}$$

This result allows us to quantify an important experimentally observable property for a thinning thread of a complex fluid, the finite time to breakup, using only two non-dimensional microstructural parameters; the molecular extensibility b of the chain and the elastocapillary number E_c. As $b \to \infty$, the breakup time diverges because the chains can stretch indefinitely. This limit of infinite extensibility is considered in the next section.

4.4 Limit of infinite extensibility ($b \to \infty$)

In the limit of infinite extensibility of the chains, $b \to \infty$ (or $B = 0$), Eq. (4.18) for the evolution of the non-dimensional radius ξ reduces to

$$3\ln(\xi) + 4E_c(\xi - 1) = -\tau. \tag{4.20}$$

At early times, when the mid-filament radius is still close to R_0, ξ can be written as $\xi = 1 - \delta$, where $\delta << 1$. Substituting this expression into Eq. (4.20) and expanding the logarithmic term, we see that the radius initially evolves linearly in time as

$$\xi \approx 1 - \frac{\tau}{3 + 4E_c}. \tag{4.21}$$

At later times, as $\xi \to 0$, the logarithmic term dominates and Eq. (4.20) predicts that the radius decays exponentially as

$$\xi = e^{4E_c/3} e^{-\tau/3}. \tag{4.22}$$

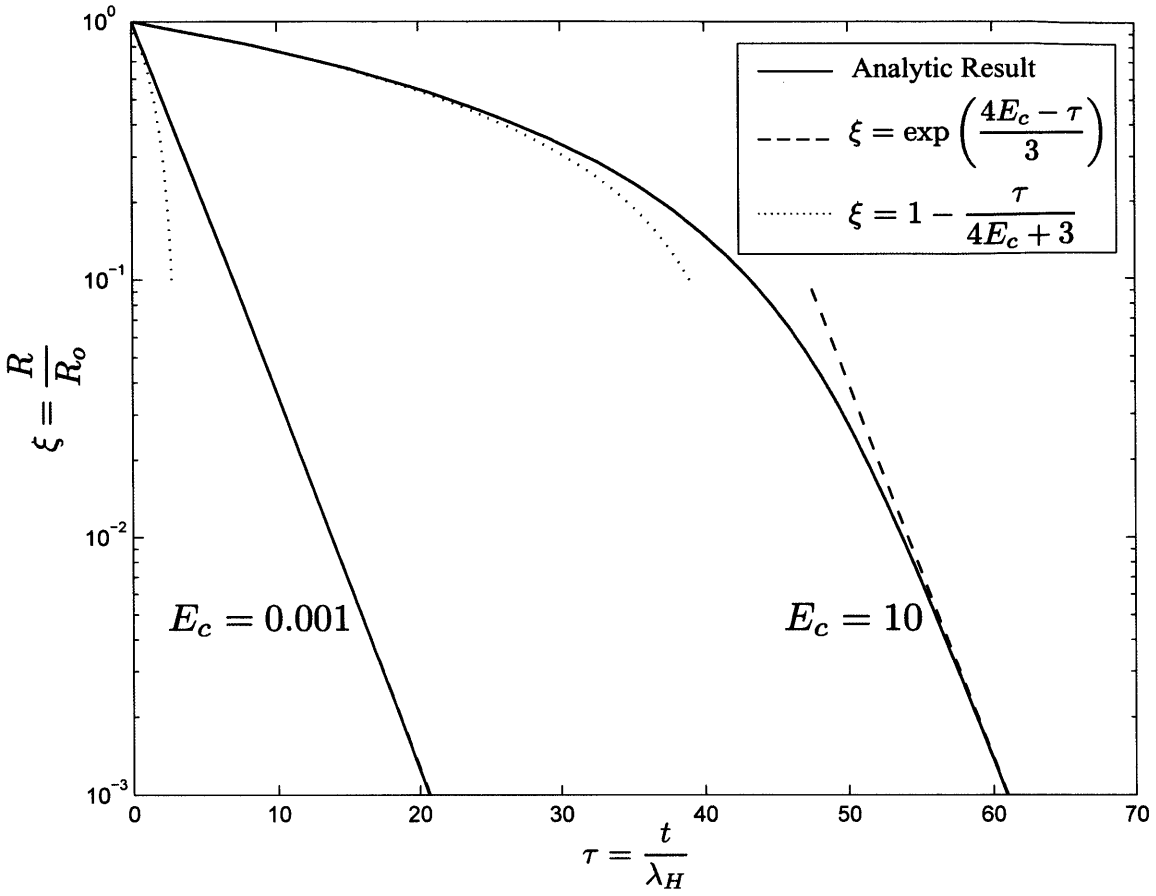

Figure 4-2: Effect of the elastocapillary number E_c on the evolution of the non-dimensional radius ξ as a function of the non-dimensional time τ, for the infinite extensibility limit of $b \to \infty$. The linear limit given in Eq. (4.21) is shown by the dotted line, and the later exponential limit in Eq. (4.22) is shown by the dashed line.

Entov and Hinch also present an analytic result for the radius evolution derived from Eqs. (4.13)-(4.15) during what they term the 'middle elastic time'; the period following the viscous dominated regime, when viscous contributions to the extensional stress can be ignored and finite extensibility effects are negligible. It is evident from Figure 4-1 that when b is small, this period is not necessarily encountered, as finite extensibility effects become important essentially as soon as polymer stresses become significant enough to play a role in the force balance. This is an important consideration when attempting to extract viscoelastic properties from CaBER experiments for dilute polymer solutions, as the relaxation time can only be obtained from radius evolution data if the exponential decay regime characteristic of elastocapillary thinning is encountered [15, 59, 68]. A criterion for achieving this exponential elastocapillary balance based on a minimum polymer concentration and molecular weight (or extensibility) argument has been discussed by Campo-Deano

and Clasen [15]. Recently, however, Sachsenheimer et al have shown that good measurements of the extensional relaxation time can still be obtained from filament sagging measurements and force calculations using a tilted CABER, even if this exponential thinning regime is not established [59]. We examine the detailed dynamics of this transition to polymer stress dominated thinning later in this work.

The appropriate analogous period to Entov and Hinch's [22] "middle elastic time" in the present analytic solution corresponds to late times when $b \to \infty$, for which the solution to the capillary thinning equation is given in Eq. (4.22). Following the arguments of Entov and Hinch [22], analysis of Eq. (4.9) indicates that when finite extensibility effects are negligible, we can take $f \approx 1$. Substituting this approximation and Eq. (4.10) along with the assumption that $A_{zz} - 1 \approx A_{zz}$ into Eq. (4.13), we obtain the following evolution equation

$$\frac{dA_{zz}}{dt} = -A_{zz}\left(\frac{4}{R}\frac{dR}{dt} + \frac{1}{\lambda_H}\right), \tag{4.23}$$

which, using the initial condition ($R = R_0$ and $t = t_0$), as previously done, yields

$$A_{zz} = \left(\frac{1}{\xi}\right)^4 e^{-\tau}. \tag{4.24}$$

Under these conditions and the assumption that the radial and tangential contributions to the polymer stress are again negligible, the force balance in Eq. (4.15) reduces to an elastocapillary balance of the form

$$\frac{\sigma}{R} = GA_{zz}. \tag{4.25}$$

Finally, combining Eqs. (4.24) and (4.25) yields Entov and Hinch's expression [22] for the non-dimensional radius evolution during the middle elastic time:

$$\xi^{(EH)} = E_c^{1/3} e^{-\tau/3} = \left(\frac{nkTR_0}{\sigma}\right)^{1/3} \exp\left(-t/3\lambda_H\right). \tag{4.26}$$

This result is clearly inconsistent with what was obtained analytically in Eq. (4.22). For a typ-

ical value of the elastocapillary number $E_c = 0.001$ at time $\tau = 0$, Eq. (4.26) predicts that $\xi = E_c^{1/3} = 0.1$, while Eq. (4.22) predicts that $\xi = e^{4E_c/3} \approx 1$. It is clear then that the assumption made in deriving our analytic solution in Eq. (4.18) that the solvent viscosity could be neglected entirely is not true in this parameter range. Indeed, for dilute polymer solutions, there is an initial period of filament thinning during which the viscous extensional stress dominates over the polymer stress contribution. Results derived from the full numerical solution accurately capture this initial period (see for example Clasen at al [18]), which explains why, unlike the analytic result, simulations show that when the middle elastic time begins, the corresponding value of the radius is $R < R_0$.

This analysis motivates the need for a composite analytic result, in which the analytic solution derived above for the radius evolution during the polymer stress-dominated capillary thinning regime is combined with an appropriate short time solution in the early viscous regime. Determining how to construct this composite analytic result and comparing it with direct numerical solution of Eqs. (4.13)-(4.15) will be the focus of the remainder of this manuscript.

4.5 Composite analytic result

In order to formulate the composite analytic solution, two remaining items are needed: first, we must solve for the temporal evolution of the radius during the initial viscous regime, and second, we must determine the point at which the transition to the polymer stress dominated regime occurs.

At this time, we more formally introduce the final non-dimensional parameter, $S = \frac{\eta_s}{\eta_p} = \frac{\eta_s}{G\lambda_H}$, which gives the ratio between the solvent and polymer contributions to the viscosity, where the latter is given by $\eta_p = G\lambda_H$. We can also express this ratio in terms of polymer concentration by writing the zero-shear viscosity in expanded form as $\eta_0 = \eta_s(1 + c[\eta] + ...) = \eta_s + \eta_p$, where c is the concentration of polymer chains and $[\eta]$ is the intrinsic viscosity. It follows that $S = \frac{1}{c[\eta]}$. Since the coil overlap concentration c^* scales as $c^* \sim \frac{1}{[\eta]}$, then $S \approx \frac{c^*}{c}$ [18]. From this result, it is clear that in order for the polymer solution to be dilute, which is the case for many biological fluids, we

require that $S \geq 1$, and for the remaining figures, we generally use $S = 1$ to be consistent with Entov and Hinch [22]. The solution given in Eqs.(4.18),(4.19) is relevant only in the limit $S << 1$.

4.5.1 Early viscous regime

Addressing the first item noted above, if $S \geq 1$, then early in the thinning process (before the polymer chains have been sufficiently stretched to begin contributing to resisting the capillary pressure that drives the thinning filament) the force balance in Eq. (4.11) simplifies to

$$\frac{\sigma}{R} = 3\eta_s \dot{\epsilon}. \tag{4.27}$$

Before continuing on to the solution of this equation during the early viscous regime, however, a more in-depth consideration of the viscocapillary balance in Eq.(4.27) is merited.

Up until this point, all derivations have assumed a perfectly cylindrical filament at all times during the thinning process. Although this is a reasonably good approximation late in the thinning process when polymer stresses are dominant (which is the case that the analytic solution considers), there is ample evidence that early on during the initial viscous thinning phase, the curvature of the filament is quite important [49, 21] (though this will not affect the agreement between the analytic model and numerical simulations since both assume a cylindrical filament). We therefore introduce the notation of Tripathi and McKinley [49], derived for viscous Newtonian fluids, to account for the axial filament curvature and enable quantitative agreement between the composite analytic solution and experimental data.

By assuming a perfectly cylindrical thread of Newtonian fluid attached to infinite reservoirs at either end, the solution assumes that the net longitudinal stress in the solvent is 0 for all times. In this limit, the axial tension in the filament arising from surface tension is

$$F_z(t) = 2\pi\sigma R_{mid}(t).$$

Tripathi and McKinley show that in fact the axial curvature and the resulting viscous longitudinal stress in the filament is non-zero, and good agreement can be achieved with experimental data by incorporating a correction factor $X(t)$ such that $F_z(t) = X(t) \times 2\pi\sigma R_{mid}(t)$. Numerical solution of the similarity solution presented by Papageorgiou for slender viscous threads shows that the value of $X(t)$ converges to a constant given by $X(t) \approx 0.7127$ [52]. As such, the modified force balance during the initial viscous thinning period is found to be

$$(2X - 1)\frac{\sigma}{R} = 3\eta_s\dot{\epsilon}, \tag{4.28}$$

where it is simple to see that $X = 1$ recovers the initial cylindrical filament solution [49].

Substituting the expression given in Eq. (4.10) for $\dot{\epsilon}$ into Eq. (4.28) and integrating using the initial condition $R = R_0$ at $t = 0$, we find the well known result that during the initial viscous regime, the filament radius decays in a linear fashion given by

$$\xi = 1 - \frac{(2X - 1)\tau}{6SE_c}. \tag{4.29}$$

From this relationship, we can derive the viscous breakup time t_c at which a Newtonian filament (in which the only term opposing the capillary pressure is the viscous extensional stress difference) would break. To find t_c, we set $\xi = 0$ in Eq. (4.29), and obtain

$$t_c = \frac{6SE_c\lambda_H}{(2X - 1)} = \frac{6\eta_s R_0}{\sigma(2X - 1)}. \tag{4.30}$$

From Eq. (4.10), it follows that the strain rate during the viscous regime is given by

$$\dot{\epsilon} = \frac{2}{\lambda_H(\tau_c - \tau)}, \tag{4.31}$$

where $\tau_c = {}^{t_c}/_{\lambda_H} = \frac{6SE_c}{(2X-1)}$.

Since elastic stretching of the chains starts from equilibrium conditions, during this period finite extensibility effects are negligible, and so again we take $Z = 1$. From Eq. (4.13) and the rela-

tionship for $\dot{\epsilon}$ during the linear viscocapillary period (Eq. (4.31)), we find that the early axial microstructural deformation is given by

$$A_{zz} = \left(\frac{\tau_c}{\tau_c - \tau}\right)^4 e^{-\tau}. \tag{4.32}$$

Figure 4-3 shows the evolution of the axial microstructural deformation A_{zz} (a), the Weissenberg number $Wi = \lambda_H \dot{\epsilon}$ (b), and the FENE parameter f (c) at very early times for various values of the finite extensibility parameter b. The solid black lines correspond to the numerical simulations, and the solutions obtained for A_{zz} and $\dot{\epsilon}$ during the initial linear viscous period are shown by the dashed blue lines. It can be seen that this expression diverges at the viscous breakup time, τ_c, as derived in Eq. (4.30) and shown in Figure 4-3 by the broken (black) line. However, for short times $\tau < \tau_c$, these expressions provide a very good analytic expression for the evolution in $A_{zz}(t)$ and $\dot{\epsilon}(t)$ for all values of b (large or small).

The solid dots denote the transition points (τ^*, A_{zz}^*) that need to be determined for the composite analytic solution and their counterparts at identical times for Wi and f. The breakup time for a Newtonian fluid, τ_c, and the transition time τ_∞^* in the limit of infinite extensibility, are shown with dot-dashed lines. As b is reduced, the level of axial microstructural deformation departs from the viscocapillary solution increasingly early as a result of the limited extensibility of the constituent dumbbells and plateaus at $A_{zz}^* = b\left(1 - \frac{1}{2Wi^*}\right) \approx b$ as given in Eq. (4.35). As b becomes very large, τ^* approaches the infinite extensibility transition time τ_∞^*, and the plateau value of A_{zz} approaches that predicted during the "middle elastic time", $A_{zz,\infty}^*$, given in Eq. (4.24) and shown by the dashed black line. The FENE parameter f behaves in a similar way, beginning at $f = 1$ when when chains are unstretched,and increasing as time progresses and the strain rate increases. In the limiting case of $b \to \infty$, the FENE parameter is $f = 1$ for all times, as expected. In contrast to A_{zz} and f, the behaviour of the strain rate is not monotonic, as is detailed in the next section.

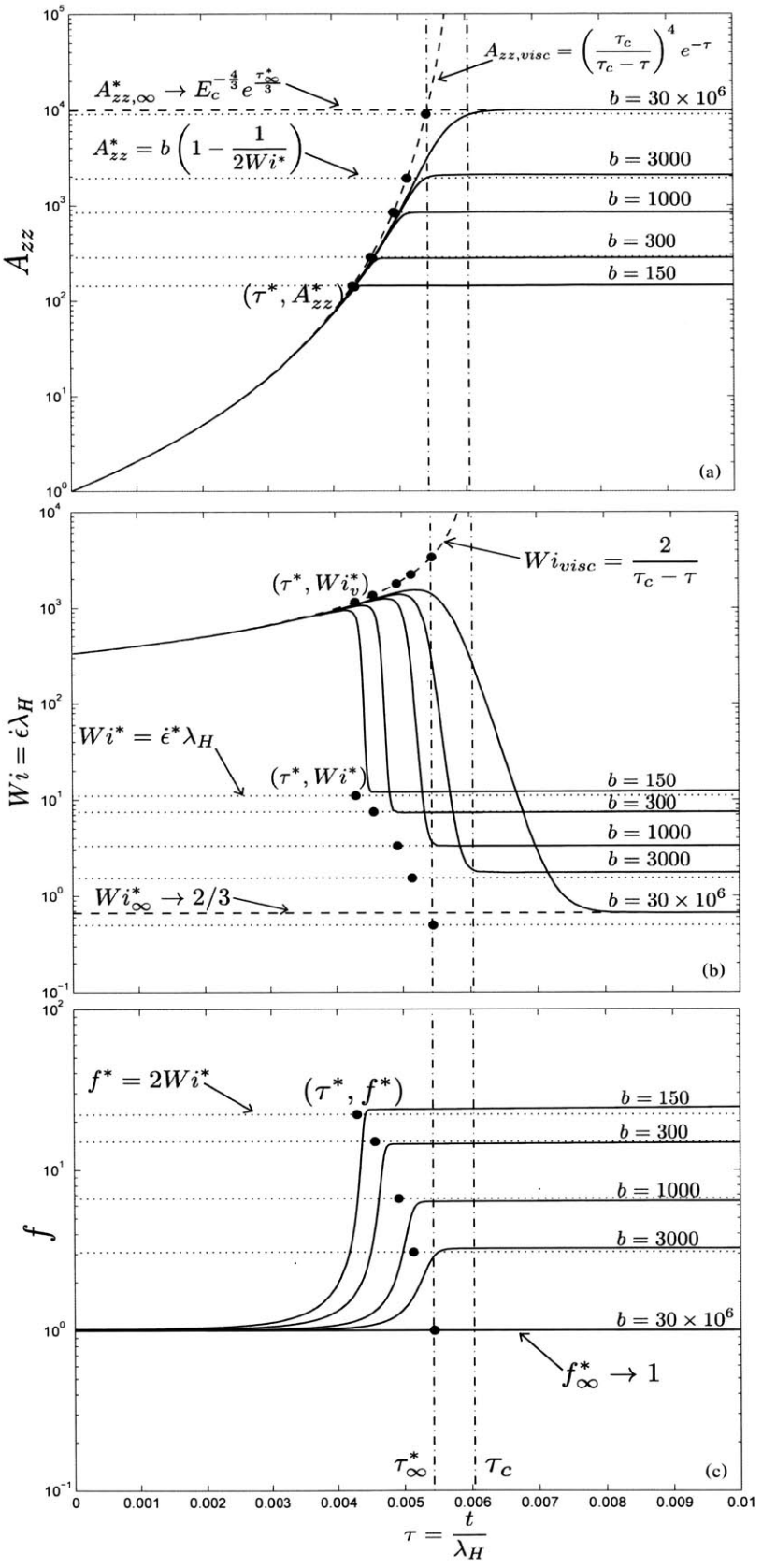

Figure 4-3: Effect of varying the finite extensibility parameter b on the level of axial microstructural deformation A_{zz} (a), the Weissenberg number Wi (b) and the FENE parameter f (c).

4.5.2 Transition to the polymer stress dominated regime

Now to address the second remaining issue, we note from Figure 4-3 that at some time t^* and radius R^* and corresponding value of the polymer stretch A_{zz}^* (where the star superscript denotes the transition point value of each variable) the extensional stress resulting from the stretching of the polymer chains becomes comparable in magnitude to the viscous contribution from the solvent. We determine this transition time by considering the point at which both the viscocapillary and elastocapillary balances hold simultaneously. The former arises from the early linear viscocapillary regime and is given by

$$\frac{\sigma}{R^*} = \frac{3\eta_s \dot{\epsilon_v}^*}{(2X-1)} \tag{4.33}$$

where $\dot{\epsilon_v}^*$ is the strain rate at time t^*, as determined from Eq. (4.31), $\dot{\epsilon}_v^* = \frac{2}{\lambda_H(\tau_c - \tau*)}$. Simultaneously, a new force balance (as given in Eq.(4.15) with only the axial stress term retained) develops between the capillary pressure and the combined resistance of the viscous and the polymer contributions to the tensile stress. In order to be able to satisfy this new relationship for the same value of the capillary stress, the strain rate must instantly drop to some new lower value, $\dot{\epsilon}^* < \dot{\epsilon_v}^*$ (as seen in Figure 4-3(b)), and equating this force balance with the viscous one from Eq.(4.33) yields the relationship

$$\frac{3\eta_s \dot{\epsilon_v}^*}{(2X-1)} = \frac{\sigma}{R^*} = 3\eta_s \dot{\epsilon}^* + nkTf^* A_{zz}^*. \tag{4.34}$$

It remains to determine the transition point values of the axial microstructural deformation A_{zz}^*, axial polymer stress $\tau_{zz}^* = -nkTf^* A_{zz}^*$, and finite extensibility parameter f^*. At the transition point (t^*, R^*), the numerical simulations shown in Figure 4-3 as the solid black lines indicate that the axial microstructural deformation reaches an approximate plateau value. The maximum deformation the polymer chains can reach is limited by the finite extensibility parameter, b. When b is small, the chains are nearly fully extended once this plateau occurs and $A_{zz}^* \approx b$. Clearly, FENE effects are non-negligible in this regime, and so the force balance derived during the "middle elastic time" is not valid. As b increases, the chains continue to extend after the linear viscous

regime ends, but it is evident from Figure 4-3 that the time rate of change of A_{zz} is comparatively very small (in dimesionless terms because of the large elastic stress difference that arises for finitely extensible chains). Therefore, at the transition point, we make the approximation that $\dot{A_{zz}} \approx 0$, which from Eq. (4.13) yields that $f^* \approx 2Wi^*$, where Wi^* is the Weissenberg number at this transition, defined as $Wi^* = \lambda_H \dot{\epsilon}^*$. From the definition of f (Eq. (4.9)) we obtain

$$A_{zz}^* = b\left(1 - \frac{1}{2Wi^*}\right). \tag{4.35}$$

By substituting the expression for A_{zz}^* given in Eq.(4.35) and the expression for $\dot{\epsilon_v}^*$ derived above into Eq.(4.34) we obtain the final result for the crossover force balance

$$3\eta_s \frac{2}{\lambda_H(\tau_c - \tau*)(2X-1)} \simeq \frac{\sigma}{R^*} \simeq 3\eta_s\dot{\epsilon}^* + 2G\lambda_H b\dot{\epsilon}^*\left(1 - \frac{1}{2Wi^*}\right). \tag{4.36}$$

Both the solvent contribution and the FENE contribution from the extended polymer chains are therefore viscous in character (i.e. they scale linearly with $\dot{\epsilon}^*$). For all that follows, we take $X = 1$ for simplicity, and drop the factor of $(2X-1)$ from the initial viscous solution, although retention of this factor or substitution of $X = 0.7127$ from the Papageorgiou similarity solution would neither be difficult nor would it alter the nature of the analysis to follow. Solving Eq.(4.36) yields a first relationship between the rate of strain at the crossover $\dot{\epsilon}^*$ and the crossover time τ^*

$$\dot{\epsilon}^* = \frac{\frac{2}{\lambda_H(\tau_c - \tau^*)} + \frac{Gb}{3\eta_s}}{1 + \frac{2Gb\lambda_H}{3\eta_s}}. \tag{4.37}$$

The second relationship is found from the fact that at the transition point, the axial microstructural deformation is constant in both regimes on either side of the 'pinch'. In other words, because $\dot{A_{zz}} \approx 0$ we have at t^* that

$$\left(\frac{\tau_c}{\tau_c - \tau^*}\right)^4 e^{-\tau^*} = A_{zz}^* = b\left(1 - \frac{1}{2Wi^*}\right). \tag{4.38}$$

This yields a second equation for $\dot{\epsilon}^*$ in terms of τ^*,

$$\dot{\epsilon}^* = \frac{1}{2\lambda_H}\left[1 - \frac{e^{-\tau^*}}{b}\left(\frac{\tau_c}{\tau_c - \tau^*}\right)^4\right]^{-1}. \tag{4.39}$$

Finally, we solve for the crossover or transition time τ^* by equating Eqs. (4.37) and (4.39) to obtain, in non-dimensional form, the following implicit expression for τ^*:

$$\frac{1}{2}\left(1 - \frac{e^{-\tau^*}}{b}\left(\frac{\tau_c}{\tau_c - \tau^*}\right)^4\right)^{-1} = Wi^* = \frac{\frac{2}{\tau_c - \tau^*} + \frac{b}{3S}}{1 + \frac{2b}{3S}}. \tag{4.40}$$

From this expression, τ^* can be solved for numerically, and the result is then used to compute the modified strain rate $\dot{\epsilon}^*$ and the plateau value of the various other parameters such as f^* and Wi^*. The dimensionless radius at the transition point, ξ^*, is found from substituting this result for τ^* into Eq. (4.29).

It is important to note that when b approaches the limit of infinite extensibility ($b \to \infty$), FENE effects and the viscous contribution to the total extensional stress are indeed negligible during this elastocapillary period, and at the end of the viscous regime the solution does transition to the "middle elastic time" defined by Entov and Hinch [22] and in Section 4.2.2. In Eq. (4.26), we derived an explicit result for the rate of radius evolution in this regime. We can therefore combine this result with the linear evolution of the filament radius (Eq. (4.29) here with $X = 1$) expected in the initial viscocapillary regime in order to determine the transition time $\tau^*_\infty = {}^{t^*_\infty}/_{\lambda_H}$ in the limit of infinite extensibility

$$1 - \frac{\tau^*_\infty}{6SE_c} = E_c^{1/3} e^{-\tau^*_\infty/3}. \tag{4.41}$$

The value of the filament radius at the transition point (denoted R^*_∞), follows from either equation ((4.26) or (4.29)). Since the "middle elastic time" is simply a special case of the early FENE period with $f = 1$ and $\dot{\epsilon}^*$ sufficiently small that the viscous extensional stress is negligible, as $b \to \infty$ the two transition points converge with

$$\lim_{b\to\infty}(t^*, R^*) \to (t^*_\infty, R^*_\infty). \tag{4.42}$$

The plateau value for the microstructural deformation in the limit of $b \to \infty$ can also be derived by combining Eqs. (4.24) and (4.26), which are both valid during the "middle elastic time", to obtain

$$A^*_{zz,\infty} \to E_c^{-4/3} e^{\tau^*_\infty/3}. \tag{4.43}$$

Although in general we must solve for this crossover time τ^* given in Eq.(4.40) numerically, in certain limits an analytic expression can be obtained. If we consider S to be of order unity, then the non-dimensional transition time τ^* is very small (typically on the order of 10^{-3}) and the exponential term in Eq. (4.40) can be approximated as unity. In the limit of large finite extensibility parameter b, a Taylor expansion of Eq.(4.40) then gives

$$\tau^* \approx \tau_c(1 - E_c^{1/3}) \tag{4.44}$$

It is simple to see that this analytic result for the case of $b \to \infty$ is in agreement with the solution obtained for the "middle elastic time" (Eq. (4.41)) for the limit of $\tau^*_\infty = {}^{t^*_\infty}/_{3\lambda_H} \to 0$.

Finally, we summarize the steps required in order to construct the composite analytic solution, and then plot and compare this result with the numerical solution. We first obtain the transition time for crossover from a viscocapillary to elastocapillary balance τ^* by solving Eq. (4.40) numerically, where for $\tau < \tau^*$, the radius evolution is given by the linear viscous result from Eq. (4.29). For times $\tau > \tau^*$, the mid-filament radius evolution $\xi(\tau)$ is given by the analytic result in Eq. (4.18), although the initial radius is no longer R_0 since there has already been capillary thinning during the initial linear viscocapillary regime. We account for this by defining a new effective elastocapillary number E_c^*, which reflects the fact that the elastocapillary thinning period actually begins with a smaller effective initial mid-filament radius, R_0^* than the initial plate radius R_0. We obtain this new radius by numerically solving Eq. (4.18) for the value of E_c^* that permits the analytic solution to pass through the point (τ^*, ξ^*). We can then calculate the effective initial radius R_0^* through the rescaling $E_c^* = E_c \frac{R_0^*}{R_0}$. Finally, with this effective elastocapillary number,

we can obtain an exact analytic expression for the finite time to breakup of the filament (which has taken account of the initial importance of the viscosity of the solvent at early times using Eq. (4.19)).

In Figure 4-4, we plot the evolution of the non-dimensional radius ξ as a function of the non-dimensional time τ for the numerical, analytic, and composite analytic solutions with $E_c = 0.01$ and a reasonably large value of the finite extensibility parameter, $b = 3 \times 10^4$, for three different values of the non-dimensional solvent viscosity, S. The analytic elastocapillary solution from Eq. (4.18), shown by the dashed-dotted black line, clearly overpredicts the full numerical result on account of its neglect of the initial period of rapid viscocapillary thinning. The inset shows how the composite analytic solution is created, as summarized above. We begin with the linear viscocapillary balance (from Eq. (4.29)), shown by the dotted line for each value of S, which matches the corresponding numerical result very well at early times $\tau < \tau^*$. At the transition point, denoted (τ^*, ξ^*), (and shown by a large star in the inset figure), we reinitialize our analytic elastocapillary result, defined with a new effective radius R_0^* (or equivalently a new elastocapillary number E_c^*), and depicted by a solid line. The reinitialized form of Eq.(4.19) then can be used to find τ_{break}. Especially for small and moderate values of S, the composite analytic result matches the numerical solution nearly exactly for the entire thinning process, as can be seen in the main graph.

Clearly, the effect of increasing the non-dimensional solvent viscosity ratio S is to delay the transition time at which the thinning becomes dominated by elastic polymer stresses as opposed to viscous extensional ones. We note that S is increased by increasing the solvent viscosity η_s, and that a delay in the transition time is associated with a decreased value in the filament radius R^* at which the transition ultimately occurs. This can clearly be seen in the inset of Figure 4-4. As the solvent viscosity is increased from $S = 1 \rightarrow 10$, the viscous extensional stress grows correspondingly as well, and so the polymer chains must be stretched more and more before the polymer stresses become significant components of the total force balance. It follows that the finite time to breakup also increases with S (for fixed values of λ_H and b), although for the parameter

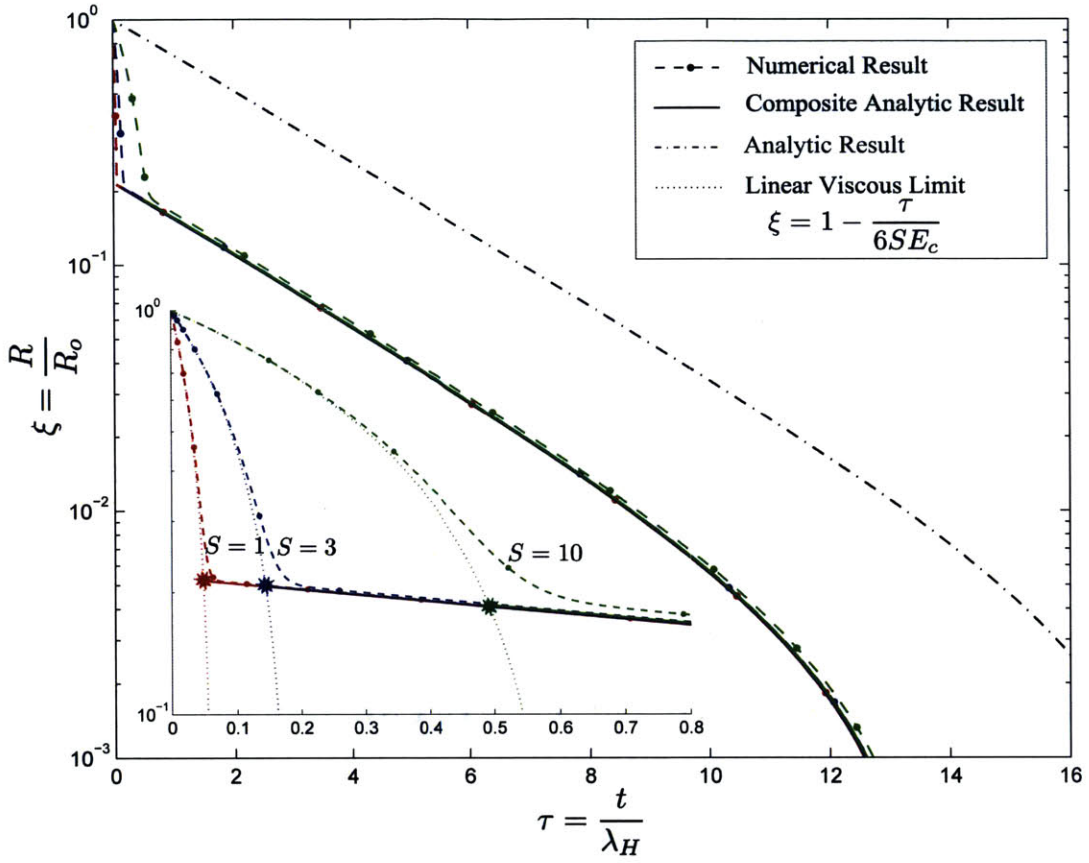

Figure 4-4: Comparison of the numerical, analytic, and composite analytic results for the evolution of the non-dimensional radius ξ as a function of the non-dimensional time τ for $E_c = 0.01$, $b = 3 \times 10^4$, and three different values of the non-dimensional viscosity $S = {}^{\eta_s}/_{\eta_p}$. The red curve denotes $S = 1$, the blue curve denotes $S = 3$, and the green curve denotes $S = 10$. The composite analytic result, composed of the linear viscous result and the analytic result from Eq. (4.18) adjusted for the new effective initial radius R_0^*, matches the full numerical solution very well. The analytic result from Eq. (4.18) overpredicts the radius due to its neglect of the solvent viscosity which dominates the initial rapid stretching phase. The inset shows that the solvent viscosity ratio S affects the solution only at very early times. The principal effect being to delay the transition point (τ^*, ξ^*), denoted by a star, as a result of the polymer stresses being comparatively smaller for longer times. However, once elastic stresses dominate, the value of S becomes irrelevant.

range chosen in Figure 4-5 the overall effect is rather small. From Eq. (4.26), it is clear that the effect of increasing the elastocapillary number E_c, either by increasing the initial radius R_0, the temperature T, or chain density n, or decreasing the surface tension of the solution σ, is to increase the radius at the transition point R^*, which implies an earlier transition to the elastocapillary thinning regime. As a result, the effect is also to increase the time to breakup of the filament, since more of the thinning process occurs at the relatively lower exponential thinning rate of the elastocapillary regime as opposed to the initial rapid linear thinning rate that results from a viscocapillary balance.

4.6 Analytic expression for the breakup time

The use of the new effective initial radius for the elastocapillary balance R_0^* and a corresponding effective elastocapillary number E_c^* in order to account for the initial viscous thinning period allows us to solve for the finite time to breakup of the filament analytically using Eq. (4.19).

In Figure 4-5, this breakup time is plotted as a function of the finite extensibility parameter b for both our composite analytic result (solid line) and the numerical solution of Eqs. (4.10) and (4.13) -(4.15) (filled points). For the purposes of numerical computation, the breakup time is chosen to correspond to the time at which $\xi^* \to 10^{-4}$. It can be seen that the two results match very well over the whole range of values of b considered.

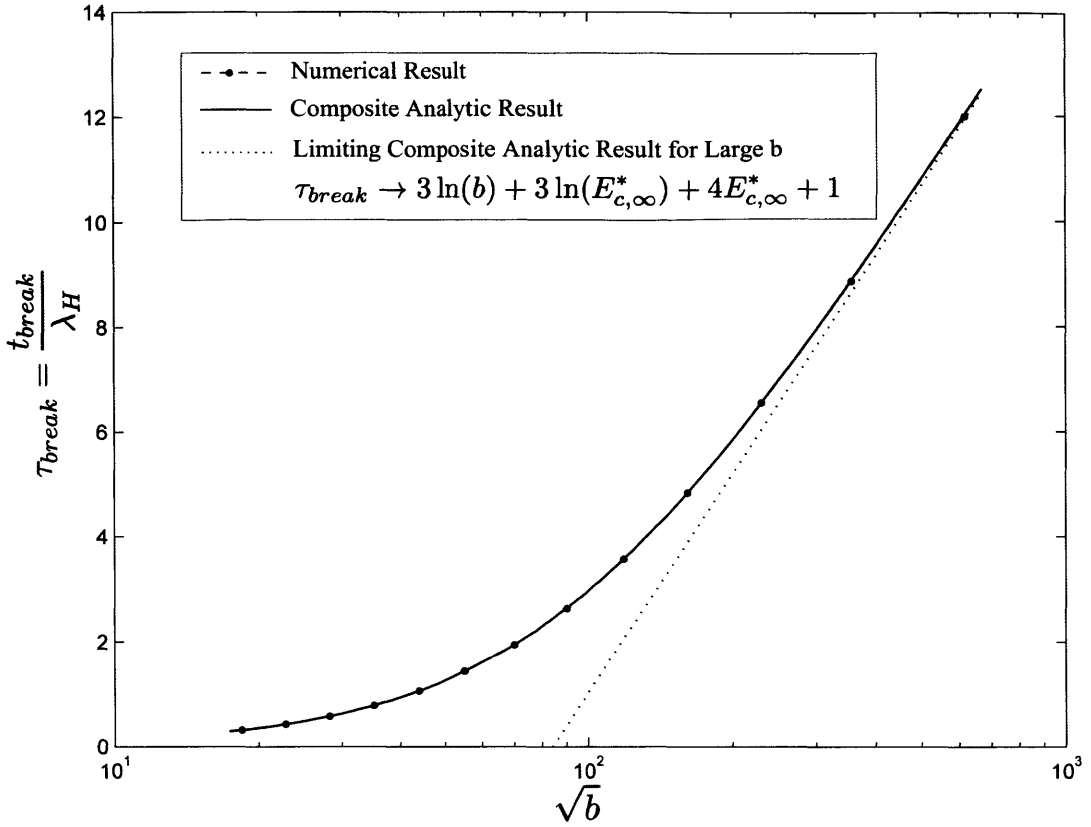

Figure 4-5: Comparison of the predicted breakup time from the numerical and composite analytic solutions, as a function of the finite extensibility parameter b. The elastocapillary number is taken to be $E_c = 0.001$ and the non-dimensional viscosity is taken to be $S = 1$ in order to provide comparison with the results presented by Entov and Hinch [22]. The two results agree very well, and converge to the limiting analytic result when the finite extensibility parameter approaches infinity.

Entov and Hinch [22] present an analytic result for the breakup time at large b (for a simplified case of their model in which the fluid is assumed to have a single relaxation time) given by

$$\tau_{break}^{(HE)} \rightarrow 3\ln\left(\frac{4b}{3}\right) + 4\ln(E_c) + 3. \tag{4.45}$$

They state that this equation overpredicts the results that they obtain from their full numerical solution rather significantly [22]. By using the solution for the breakup time given in Eq. (4.19),it can readily be shown that in the limit of $b \rightarrow \infty$, Eq. (4.19) becomes

$$\tau_{break} \rightarrow 3\ln(b) + 3\ln(E^*_{c,\infty}) * + 4E^*_{c,\infty} + 1 \tag{4.46}$$

where $E^*_{c,\infty} = E_c \xi^*_\infty$ is the effective rescaled elastocapillary number in the limit of infinite extensibility that is relevant after crossover to the elastocapillary balance.

This result is plotted as the dotted line in Figure 4-5. At large values of the finite extensibility parameter corresponding to $\sqrt{b} \gtrsim 300$, both the composite analytic and numerical solutions converge to this asymptotic result that is appropriate for very large (but finite) values of the extensibility parameter. Thus, our result improves on the expression derived by Entov and Hinch [22] (Eq. (4.45)).

4.7 FENE-P experimental comparison

As validation of the FENE-P model described above, we attempt to describe the CaBER data for saliva at various ages presented in Section 2.2.3. We estimate the solvent viscosity of saliva to be $\eta_s = 0.003 Pas$ from the shear rheology data in Section 2.2.2 and approximate the surface tension as $\sigma = 0.06 Nm$ [41]. Furthermore, the concentration of MUC5B in human saliva is approximately $c = 233 \frac{\mu g}{ml}$ [57]. The initial radius R_0 is taken to be the experimental value of the filament radius at the strike time (when the plates have reached their final separation height), and the relaxation time λ_H is measured from the slope of the experimental curve during the exponential thinning region. The rest of the parameters are determined by fitting an appropriate value for the molecular weight MW at each given age. The fit values for the molecular weight MW, and the corresponding values of the finite extensibility parameter b, elastocapillary number E_c, and dimensionless viscosity S are shown in Table 4.1.

Time[min]	$MW[\times 10^6 \frac{g}{mol}]$	b	E_c	S
30	0.12	747.84	0.0505	0.005
60	0.15	894	0.0362	0.00857
120	0.28	1473	0.0199	0.0197
300	0.7	3065.8	0.0057	0.110
660	9	23651.6	368.8×10^{-6}	1.948

Table 4.1: FENE-P model parameters for saliva at various ages.

In Figure 4-6, the predictions of the model using the parameters described above are plotted against the experimental CaBER data for saliva at various ages. Several model defficiencies are immediately apparent.

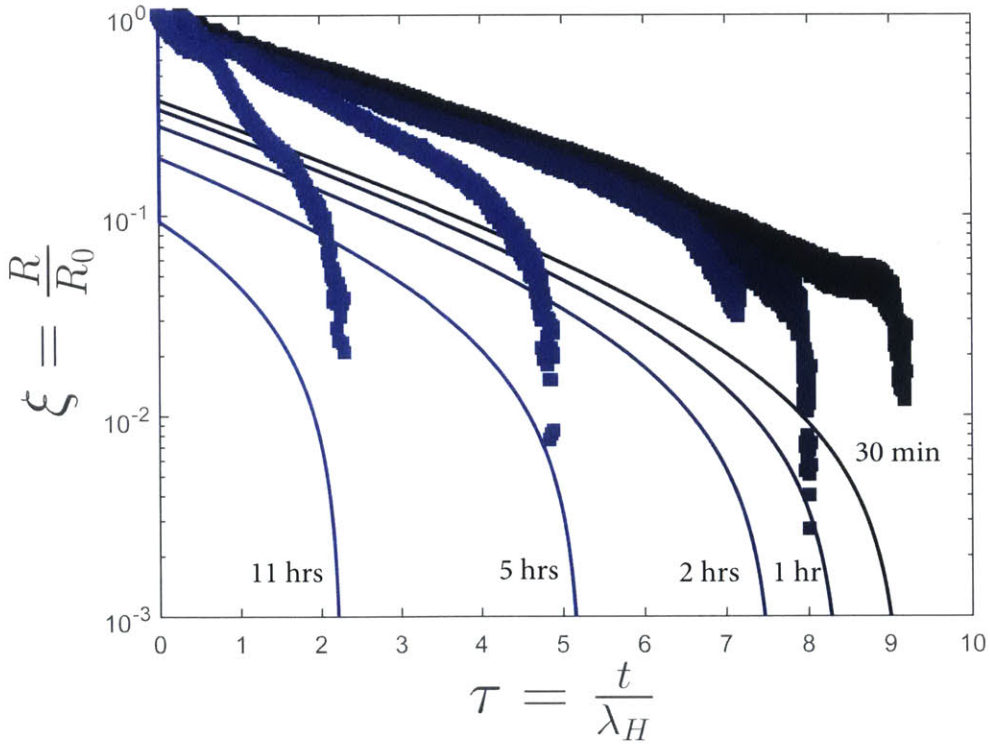

Figure 4-6: Fit of FENE-P model to CaBER data for saliva at different ages.

Firstly, the model predicts a rapid initial viscocapillary dominated drop in the filament radius by

approximately one order of magnitude before the elastocapillary region begins, which is evidently not observed in the experimental data. Additionally, this model of a dilute solution of dumbbells is unable to capture the observed phenomenon seen experimentally of a sudden and dramatic filament rupture, particularly for younger saliva samples.

Additionally, in order to capture the decreasing breakup time observed with age, it is necessary to increase the molecular weight in the model. Doing so decreases the number density of polymer chains n more dramatically than it increases the finite extensibility parameter b, which has the effect of decreasing the elastocapillary number E_c and increasing the dimensionless viscosity S. Correspondingly, the rapid initial viscocapillary drop is predicted to increase with age, and the time to breakup shortens. It is not physical to believe that degradation and enzymatic activity would lead to an increase in the mucin molecular weight, and furthermore, the fit values of molecular weight are several orders of magnitude lower than those reported in the literature of nearly $200 \times 10^6 \frac{g}{mol}$ [61]. This motivates the development of alternative model systems in the chapters to follow.

4.8 FENE-P model conclusions

In this section we have derived a composite analytic solution that describes the complete time evolution of the filament radius and the finite time to breakup of a FENE-P fluid filament undergoing elastocapillary thinning. The composite analytic solution consists of an initial viscocapillary regime characterized by an initial linear decrease in the filament radius (see Eq. (4.29)), followed by a rapid crossover (or 'pinch point') to an elastocapillary regime dominated by the polymer stress, for which we have determined an analytic expression for the evolution of the filament radius (see Eq. (4.18)). The time and radius at which the crossover between the two regimes occurs, denoted (t^*, R^*) respectively, can be approximated analytically by considering simultaneous force balances: during the initial linear regime, it is assumed that the viscous extensional stress alone balances the capillary force; while in the second regime, both the viscous extensional stress and the FENE polymer stress are important. By determining this pinch point and rescaling the initial radius for our analytic elastocapillary balance to be R_0^*, the finite breakup time can be derived

and is given by Eq. (4.19). We have also noted that in the limit of infinite chain extensibility ($b \to \infty$), this transition point converges to values (t^*_∞, R^*_∞), which correspond to an alternate elastocapillary balance in which capillary forces are opposed only by neo-Hookean polymer stresses (without FENE effects) and the viscous extensional stress is negligible. This corresponds to the "middle elastic time" regime first considered by Entov and Hinch [22]. We have also shown that our composite analytic solution matches very well with the full numerical simulations over a wide range of fluid parameters in terms of both the time evolution of the mid-filament radius $R(t)$ and the finite time to breakup. Although negligibly small, these simulations do incorporate the contribution of the radial stresses.

Part of the challenge in determining the composite analytic solution arises from determining the crossover point (t^*, R^*) between the initial viscocapillary and (finitely extensible) elastocapillary balance that develops at later times. Determining this crossover accurately is important for establishing the characteristic length scale on which elastic effects become important in dilute polymer solutions. However, as the concentration of dissolved polymer increases (and S decreases), or as the network forming character of the fluid sample increases, this term becomes progressively less important. This can be easily observed experimentally by the absence of an initial viscocapillary thinning phase (see for example the filament thinning measurements in [44], [2], [66] and [30]).

Although the FENE-P model can qualitatively capture some of the behaviour observed with CaBER of saliva, it is severely deficient in many respects. Firstly, it predicts an increase in MUC5B molecular weight with age as a result of polymer density dominating the mechanics of the flow, which is unphysical and inconsistent with the hypothesis that enzymatic activity leads to degradation and shortening of the chains. Furthermore, the model predicts a rapid initial viscocapillary decrease in the filament radius, and smooth decrease to breakup, which is not observed experimentally.

Both of these deficiencies suggest that modeling saliva as a dilute polymer solution may not be

ideal. Upon examination of Figure 2-2, further thought suggests that perhaps the network forming properties of the large mucins cannot be neglected in the development of a molecular model. As such, a subsequent model, the Rolie-Poly-FENE-P model based off of the Rolie-Poly model created by Graham et al [45, 50] was developed.

Chapter 5

The Rolie-Poly-FENE-P model

5.1 Brief overview of the rheology of entangled polymers

Graham, Likhtman et al have developed a model for fast flows of entangled polymer melts which they term the Rolie-Poly (Rouse Linear Entangled Polymers) Model [45, 50]. In contrast to the FENE-P model developed previously, in which the time rate of change of the microstructural deformation tensor $\boldsymbol{A}$ depended only on the flow and the FENE term related to chain stretching (see Equations (4.13) and (4.14)), the Rolie-Poly model accounts for the processes of reptation, constraint release, chain stretch, and contour length fluctuations in addition to the external flow.

Before considering the governing equations, it is useful to consider what these various terms mean physically. Consider Figure 5-1 below taken from Larson [42]. In Figure 5-1 A, a sketch of a random entangled polymer network is shown, with one chain bolded for clarity. As originally theorized by de Gennes in 1971 [19], the surrounding polymers effectively confine the chain in question to move within a tube, and this idea is shown in Figure 5-1 B. The segments of the tube are modelled as a random walk, with each step size, or tube segment, equivalent in size to the tube diameter [42, 19]. The tube contour length is known as the primitive path, and this length is much less than the total length of the polymer chain [42, 19].

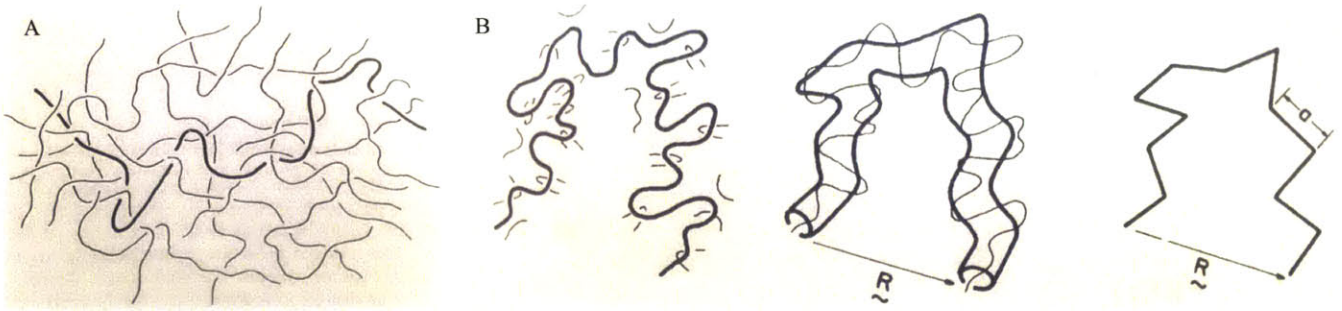

Figure 5-1: A: Sketch of an entangled polymer network. B: The surrounding polymers confine the chain in question to a 'tube'. Images taken from [42]

In an entangled network, each entanglement segment is characterized by an entanglement relaxation time λ_e. When subjected to an external flow, the relaxation process of chain retraction in response to being stretched, also considered in the FENE-P model, occurs on the time-scale of the Rouse time, λ_R [45]. By definition, the Rouse time is related to the entanglement relaxation time by

$$\lambda_R = z^2 \lambda_e,$$

where z is the number of entanglement segments in one chain. As a result of the entanglements, however, there are additional relaxation mechanisms to consider other than chain retraction, as shown in Figure 5-2 from Larson [42].

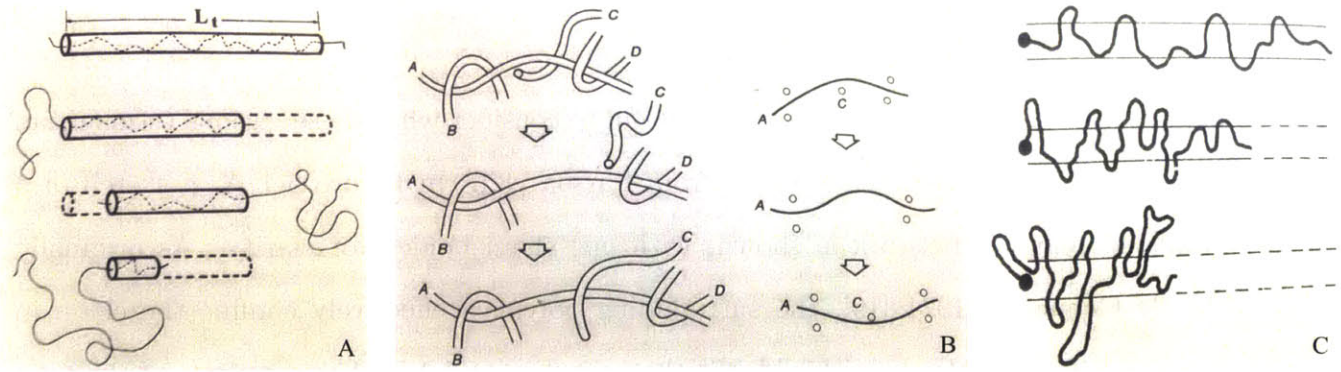

Figure 5-2: Illustration of the mechanisms of reptation (A), constraint release (B), and fluctutations of the primitive path length (C)

The first additional mechanism to consider is that of reptation. As developed by de Gennes, reptation is the notion that a chain can migrate out of its confining tube as a result of thermal

motion and reorient [42, 19]. This occurs over a time-scale known as the reptation time, defined as

$$\lambda_D = 3z^3\lambda_e.$$

A schematic of this process is shown in Figure 5-2 A. Furthermore, since all of the polymers in the network are reptating, then during the reptation time of one chain, the constraints that are confining it to its original tube are changing. As constraints are relaxed, the tube and chain are able to take on new configurations and reorient [42]. This process, known as constraint release, is illustrated in Figure 5-2 B. A final mechanism to consider is that of primitive path fluctuations, shown in Figure 5-2 C. This process occurs when one end of the polymer chain is tethered, say to a polymer branch point [42, 19]. This tethering does not allow the chain to reptate, but instead the free end of the chain can relax away from the end of the tube, releasing those constraints on its configuration [42].

With these concepts defined, it is now possible to derive the full Rolie-Poly Equations as done in [45].

5.2 Rolie-Poly equations derivation

Analogously to Equations (4.13) and (4.14), the governing equation for the time rate of change of the polymer microstructural deformation $\boldsymbol{A}$ for the Rolie-Poly model is given by

$$\frac{d\boldsymbol{A}}{dt} = (\nabla \boldsymbol{v}) \cdot \boldsymbol{A} + \boldsymbol{A} \cdot (\nabla \boldsymbol{v})^T - \frac{1}{\lambda_D}(\boldsymbol{A} - \boldsymbol{I}) - f_{retr}(tr\boldsymbol{A})\boldsymbol{A} - f_{ccr}(tr\boldsymbol{A})(\boldsymbol{A} - \boldsymbol{I}), \tag{5.1}$$

where f_{retr} is the function describing chain retraction, f_{ccr} is the function describing constraint release, and $\boldsymbol{I}$ is the identity matrix [45].

In the limit of small stretch ($tr(\boldsymbol{A}) - 3 \ll 1$), Likhtman et al [45] show that the retraction and

constraint release terms can be expressed as

$$f_{retr}(trA) = \frac{2(tr(A) - 3)}{\lambda_R}$$

and

$$f_{ccr}(trA) = \frac{2\beta(tr(A) - 3)}{\lambda_R}$$

where β is the CCR coefficient originally introduced by Marrucci [46] and generally taken to be $\beta = 0.5$ [45]. Similarly, in the large stretch limit ($tr(A) - 3 \gg 1$),

$$f_{retr}(trA) = \frac{2}{\lambda_R}$$

and

$$f_{ccr}(trA) = \frac{2\beta\left(\frac{tr(A)}{3}\right)^2}{\lambda_R}$$

.

By interpolating between the small and the large stretch regimes, Likhtman et al arrive at the general Rolie-Poly constitutive equation

$$A_{(1)} = -\frac{1}{\lambda_D}(A - I) - \frac{2\left(1 - \sqrt{\frac{3}{tr(A)}}\right)}{\lambda_R}A - \frac{2\left(1 - \sqrt{\frac{3}{tr(A)}}\right)}{\lambda_R}\beta\left(\frac{tr(A)}{3}\right)^{\delta}(A - I), \qquad (5.2)$$

where again the subscript (1) denotes the upper convected derivative and δ is a negative power obtained by a fit to their full theory, generally chosen to be $\delta = -0.5$ [45].

This constitutive equation is applicable for both large and small chain stretch. However, examination of Figure 4-3 A shows that the large stretch criterion of $tr(A) - 3 \gg 1$ is satisfied for essentially all times during the flow. As such, we can derive a simplified form of the Rolie-Poly-FENE-P equations which retains only the large stretch limiting forms of f_{retr} and f_{ccr}, namely

$$\boldsymbol{A}_{(1)} = -\frac{1}{\lambda_D}(\boldsymbol{A}-\boldsymbol{I}) - \frac{2}{\lambda_R}\boldsymbol{A} - \frac{2\beta\left(\frac{tr(\boldsymbol{A})}{3}\right)^{\delta}}{\lambda_R}(\boldsymbol{A}-\boldsymbol{I}). \tag{5.3}$$

At this point, the dynamics of the network have been accounted for, but there is no inclusion of any finite extensibility effects of the polymer chains. Likhtman et al suggest that this could be included by modifying the Rouse time scale λ_R in order for it to depend on the amount of stretch in the chain [45]. Physically, when the chain is unstretched, the retraction time scale should be undisturbed and equal to the Rouse time λ_R. Conversely as the chain becomes very stretched, similar to pulling a spring towards its maximum extension, the retraction time-scale should decrease until $\lambda_R \to 0$ when the finite extensibility of the chain is reached. In other words, we seek a solution of the form

$$\lambda_R \to \lambda_R \times func\left((1-\frac{tr(\boldsymbol{A})}{b})\right)$$

so that when

$$\frac{tr(\boldsymbol{A})}{b} \ll 1, \quad \lambda_R \to \lambda_R$$

and when

$$\frac{tr(\boldsymbol{A})}{b} \gg 1, \quad \lambda_R \to 0.$$

In order to choose the exact functional form for the effective Rouse time, we require that in the limit of no entanglements, or equivalently only one entanglement segment ($z = 1$), the FENE-P form of the constitutive equation be recovered. Comparison of Equations (5.5) and (4.13) in the limit of large stretch ($\boldsymbol{A} \gg \boldsymbol{I}$) reveals, as expected, that the reptation and constraint release terms are not encountered in the FENE-P equation. In the limit of $z = 1$, we can ignore those two terms, as we have eliminated interactions with other chains in this limit.

With these terms eliminated then, comparison of Equations (5.5) and (4.13) reveals that the functional form chosen should be

$$\lambda_R \to \lambda_R \frac{2}{f}$$

where f is the FENE parameter defined in Equation (4.12) as

$$f = f(tr(\boldsymbol{A})) = \frac{1}{1 - \frac{tr(\boldsymbol{A})}{b}}.$$

Substituting this result into the complete Rolie-Poly constitutive equation ((5.2)) yields the complete Rolie-Poly-FENE-P constitutive equation

$$\boldsymbol{A}_{(1)} = -\frac{1}{\lambda_D}(\boldsymbol{A} - \boldsymbol{I}) - \frac{f\left(1 - \sqrt{\frac{3}{tr(\boldsymbol{A})}}\right)}{\lambda_R}\boldsymbol{A} - \frac{f\left(1 - \sqrt{\frac{3}{tr(\boldsymbol{A})}}\right)}{\lambda_R}\beta\left(\frac{tr(\boldsymbol{A})}{3}\right)^{\delta}(\boldsymbol{A} - \boldsymbol{I}), \tag{5.4}$$

and similarly substituting into the simplified Rolie-Poly constitutive equation in the limit of large stretch (5.3) yields the simplified Rolie-Poly-FENE-P constitutive equation

$$\boldsymbol{A}_{(1)} = -\frac{1}{\lambda_D}(\boldsymbol{A} - \boldsymbol{I}) - \frac{f}{\lambda_R}\boldsymbol{A} - \frac{f\beta\left(\frac{tr(\boldsymbol{A})}{3}\right)^{\delta}}{\lambda_R}(\boldsymbol{A} - \boldsymbol{I}). \tag{5.5}$$

It should be noted that Kabanemi and Hétu have discussed a similar method for inclusion of finite extensibility for FENE-CR springs in the Rolie-Poly model [36]. Although they arrive at a slightly different functional form for the effective Rouse time λ_R, the overall principles are very similar.

With these new constitutive equations and the governing equation of the flow, CaBER simulations of the Rolie-Poly-FENE-P fluid can be performed exactly as was done in Section 4. The only subtlety to note is the slight change in the dependence of the relationship between the polymer stress $\boldsymbol{\tau}_p$ and the microstructural deformation $\boldsymbol{A}$. Because the Rolie-Poly-FENE-P model considers the stretch of a polymer *entanglement segment* and not an entire chain, the density term n effectively becomes

$$n_e = zn$$

in order to denote the entanglement segment density as opposed to the chain density. Correspond-

ingly, the appropriate elastic modulus to use when calculating the polymer stresses is

$$G_e = zG$$

We can also consider the analogous Rolie-Poly-FENE-P "middle elastic regime" ($f \approx 1$ and $\boldsymbol{A} \gg \boldsymbol{I}$) to that derived in Section 4.4 for the FENE-P model in order to obtain a relationship between the relaxation time predicted by the FENE-P fluid and measured directly from CaBER experiments, λ_H, and the entanglement relaxation time λ_e. In order to compare Equations (5.5) and (4.23), it is once again required that constraint release be "turned off" by setting $\beta = 0$. Ye et al [75] and van Meerveld [70] have shown that although constraint release is important in weaker extensional flows where $\lambda_{flow} \lesssim \lambda_D$, it is generally not a significant component of chain relaxation for stronger extensional flows such as those found in CaBER. This appears to be reasonable: if the chains are not able to reptate within the time scale of the flow, then there is no real mechanism for releasing constraints on the tube configuration.

Reexpressing λ_H and λ_R in terms of λ_e and using the approximations $\boldsymbol{A} - \boldsymbol{I} \approx \boldsymbol{A}$ and $\beta = 0$ allows us to arrive at a "middle elastic regime" form for the Rolie-Poly-FENE-P model, analogous to the result in Equation (4.23) for the FENE-P mode:

$$\boldsymbol{A}_{(1)} \approx -\left(\frac{3z+1}{3z^3}\right)\frac{\boldsymbol{A}}{\lambda_e} \tag{5.6}$$

which by direct comparison with Equation (4.23) yields that

$$\lambda_H \to \frac{3z^3\lambda_e}{3z+1}. \tag{5.7}$$

In order to summarize these ideas, the complete Rolie-Poly constitutive equation without finite extensibility in Equation (5.2) and the complete Rolie-Poly-FENE-P constitutive equation in Equation (5.4) with $b = 1000$ are combined with the governing equations of simple elongational flow

$(v_r = -\frac{1}{2}\dot{\epsilon}(t)r, v_z = \dot{\epsilon}(t)z)$ and solved numerically for $E_c = 0.001$, $z = 10$, $\lambda_e = 0.001s$, and various values of the strain rate $\dot{\epsilon}$. In Figure 5-3, the axial microstructural deformation A_{zz} and the extensional viscosity $\eta_e = \frac{\tau_{p,zz} - \tau_{p,rr}}{\dot{\epsilon}}$ are plotted as a function of the strain rate $\dot{\epsilon}$.

When the time scale of the flow $\lambda_{flow} = \frac{1}{\dot{\epsilon}}$ is greater than the reptation time λ_D, the chains have time to reptate and reorient during the flow and the viscosity initially remains approximately constant. As the flow time scale λ_{flow} becomes smaller than the reptation time λ_D but still larger than the Rouse chain relaxation time λ_R, the chains can no longer reptate and begin to align with the flow, but are still not noticeably stretched by the flow as they still have time to retract within their confinement tubes. As a result, the viscosity is seen to decrease. Finally, as λ_{flow} becomes shorter λ_R, the chains are no longer able to retract and begin to be stretched by the flow. The viscosity correspondingly increases, either indefinitely in the case of no finite extensibility, or until the chains reach their maximum extension in the case of the Rolie-Poly-FENE-P model, at which point the the viscosity reaches a final plateau value.

5.3 Parameter definition

In order to be able to model CaBER experiments of saliva or other entangled polymer systems using the Rolie-Poly-FENE-P theory, it is necessary to go through the derivation for how the various parameters of the model are derived from the molecular properties of the polymer of interest.

In Figure 5-4, a side-by-side sketch of the systems considered in both the FENE-P and Rolie-Poly-FENE-P models is presented. In the Rolie-Poly-FENE-P model, we consider an entangled network of polymer chains of molecular weight MW composed of N repeat units of molecular weight M_o and length l within a solvent of viscosity η_s. Each entanglement segment contains N_e repeat units, leading to a total of $z = \frac{N}{N_e}$ entanglements or entanglement segments per chain.

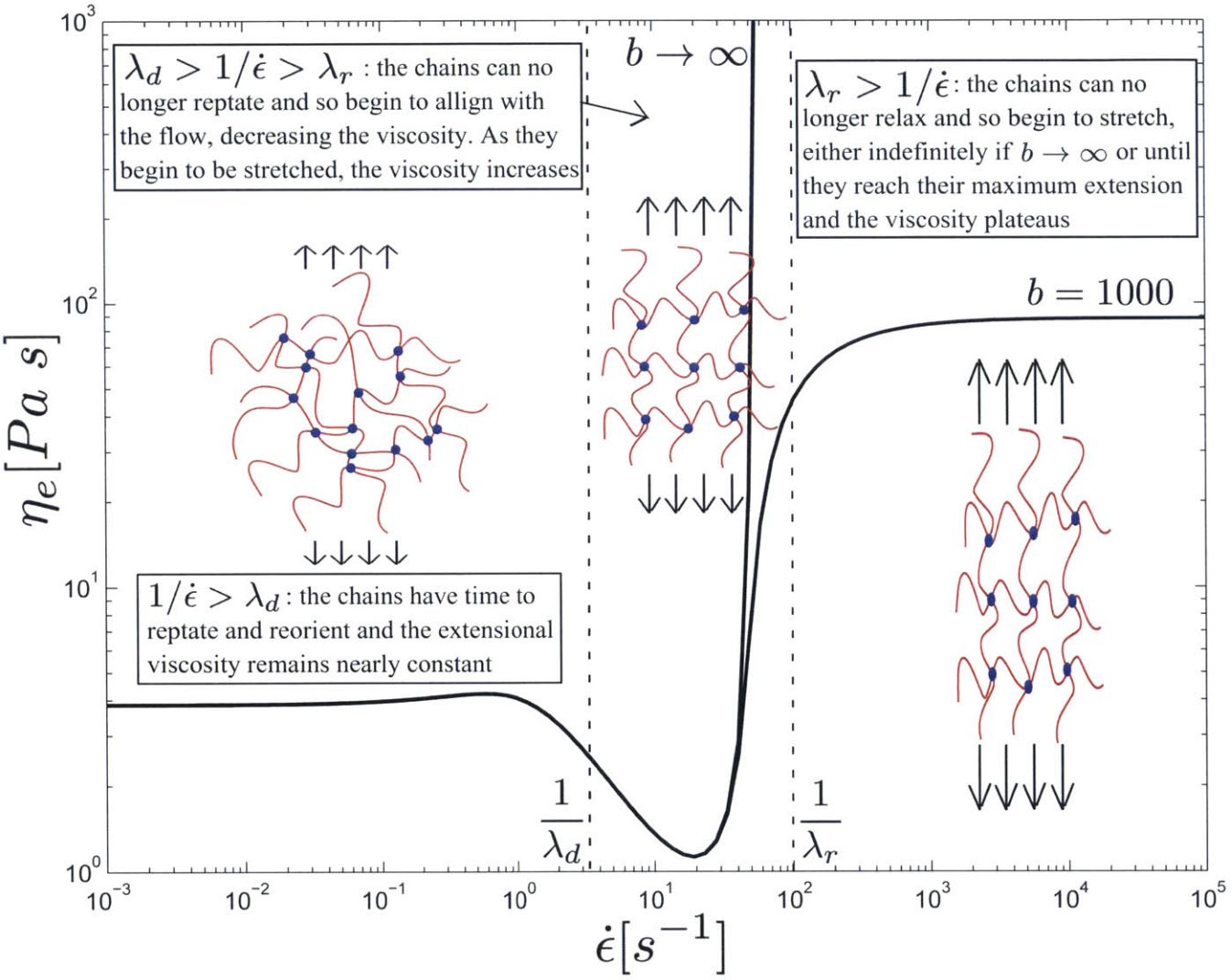

Figure 5-3: Illustration of the extensional viscosity η_e of the Rolie-Poly network during simple elongational flow with and without finite extensibility as a function of the strain rate $\dot{\epsilon}$.

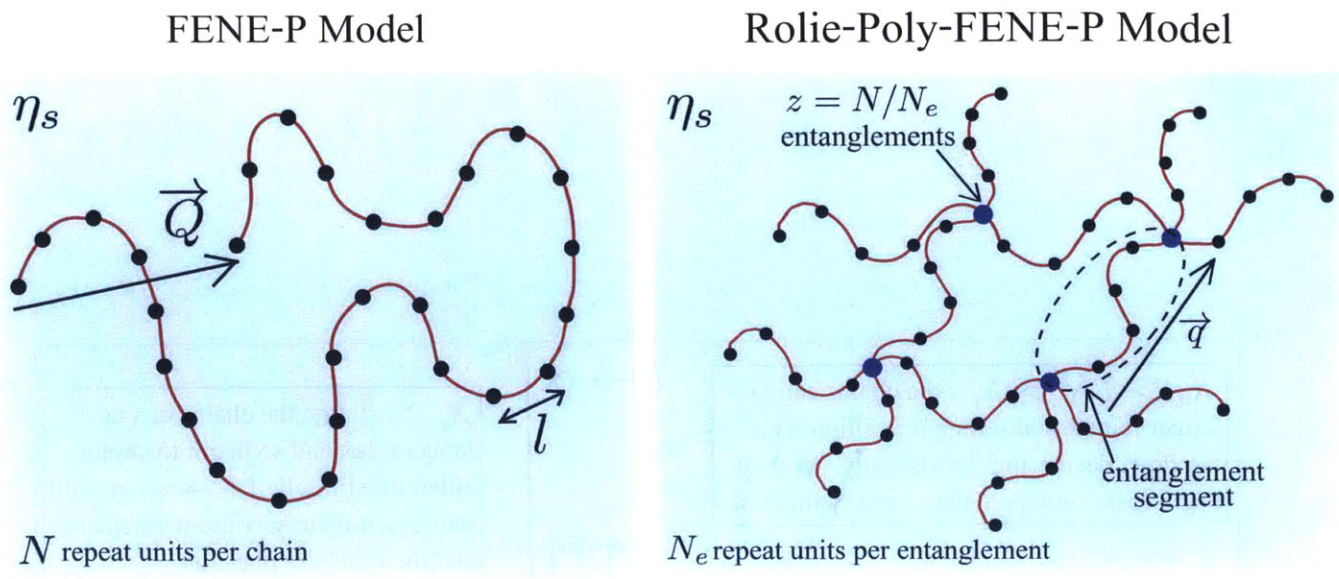

Figure 5-4: Comparison and explanation of the various parameters for the FENE-P and Rolie-Poly-FENE-P models.

In comparison to the FENE-P model where the polymer chain force $\boldsymbol{F}$ was a function of the end-to-end vector $\boldsymbol{Q}$ of the entire chain (see Equation (4.1)), we consider instead for the Rolie-Poly-FENE-P model the force $\boldsymbol{F}_e$ in an entanglement segment as a function of $\boldsymbol{q}$, the end-to-end vector between two entanglements. The remainder of the derivations for the polymer stress tensor $\boldsymbol{\tau}_p$ are identical to the FENE-P model, with the exception that the density term is the entanglement segment density n_e as opposed to the chain density n, where $n_e = zn$.

It remains to determine the number of entanglements z and the entanglement relaxation time λ_e for the network in question. Following the definitions of Larson et al [43], the entanglement molecular weight $M_e = N_e M_o$ is defined as

$$M_e = \frac{4}{5}\frac{ck_BTN_A}{G_N} \tag{5.8}$$

where c is the polymer concentration and G_N is the plateau value of the elastic modulus for the polymer solution. In general, this plateau modulus G_N is not as clearly defined as the analogous one for a polymer melt, G_N^0, [75], but it can nevertheless be approximated using SAOS data.

The number of entanglements then follows immediately as

$$z = \frac{MW}{M_e}. \tag{5.9}$$

The entanglement relaxation time λ_e is obtained using Equations (5.7) and (5.9) and from the system relaxation time λ_H obtained from CaBER data. The entanglement relaxation time is also defined as[43]

$$\lambda_e = \left(\frac{4}{5}\right)^2 \left(\frac{M_e}{M_o}\right)^2 \frac{\zeta l^2}{3\pi^2 k_B T}, \tag{5.10}$$

which allows us to estimate the friction coefficient ζ discussed in Section 4.2.

With these parameters defined, we first compare the CaBER predictions of the Rolie-Poly-FENE-P model with a test system of entangled polyethylene oxide (PEO) solutions taken from Arnolds et al [4]. We then consider the problem of the degrading saliva network.

5.4 Comparison with experiment

5.4.1 Entangled PEO solutions from Arnolds et al [4]

Arnolds et al [4] investigated the shear and extensional rheology of PEO solutions in the concentrated to entangled regimes, which is a very similar system to the one of interest to this thesis of entangled mucin networks. Consequently, there is excellent shear and extensional rheology data available in this paper with which to validate the results of the current model. We choose to focus on the data for the $1 \times 10^6 \frac{g}{mol}$ PEO solution at concentrations of $1, 2, 3, 5wt\%$.

In keeping with the procedure defined in the previous section, the plateau modulus G_N and the system relaxation time λ_H are determined respectively from SAOS and CaBER data from [4]. We furthermore assume an initial radius $R_0 = 3mm$ of the plate radius, and use molecular properties for PEO in water to determine the molecular properties of the solution. Equations (5.8)-(6.4) can

then be used to determine the remaining parameters for the Rolie-Poly-FENE-P model. Table 5.1 summarizes all of this data for the various runs.

wgt %	G_N[Pa]	M_e [MDa]	z	λ_e[ms]	λ_H[ms]	b	S	E_c
5	800	0.131	7.64	0.651	36.5	1028.85	0.00153	9.7
3	150	0.419	2.39	6.87	34.4	2608.98	0.000776	1.92
2	90	0.465	2.15	4.77	19.1	2838.42	0.00187	0.995
1	40	0.523	1.91	2.92	9.1	3118.88	0.00684	0.449

Table 5.1: Rolie-Poly-FENE-P model parameters for $MW = 1 \times 10^{6g}/_{mol}$ PEO at various concentrations based off of data from Arnolds et al [4].

Arnolds et al report that for $MW = 1 \times 10^{6g}/_{mol}$ PEO in water, the critical overlap concentration (above which a solution is no longer defined as semi-dilute) is $c^* = 0.41wt\%$, and the critical entanglement concentration is $c_e = 2.48wt\%$. This appears to be quite consistent with the predictions of the model, where we see that the number of entanglements drops to approximately $z = 1$ at $c = 1wt\%$. It is clear though from the values of the dimensionless viscosity that none of the solutions are dilute ($S \ll 1$).

In Figure 5-5, CaBER data for $MW = 1 \times 10^{6g}/_{mol}$ PEO solutions at concentrations of $c = 1, 2, 3, 5wt\%$ from Arnolds et al [4] (shown as solid squares) is compared to the predictions of the Rolie-Poly-FENE-P model (solid lines) using the parameters tabulated in Table 5.1.

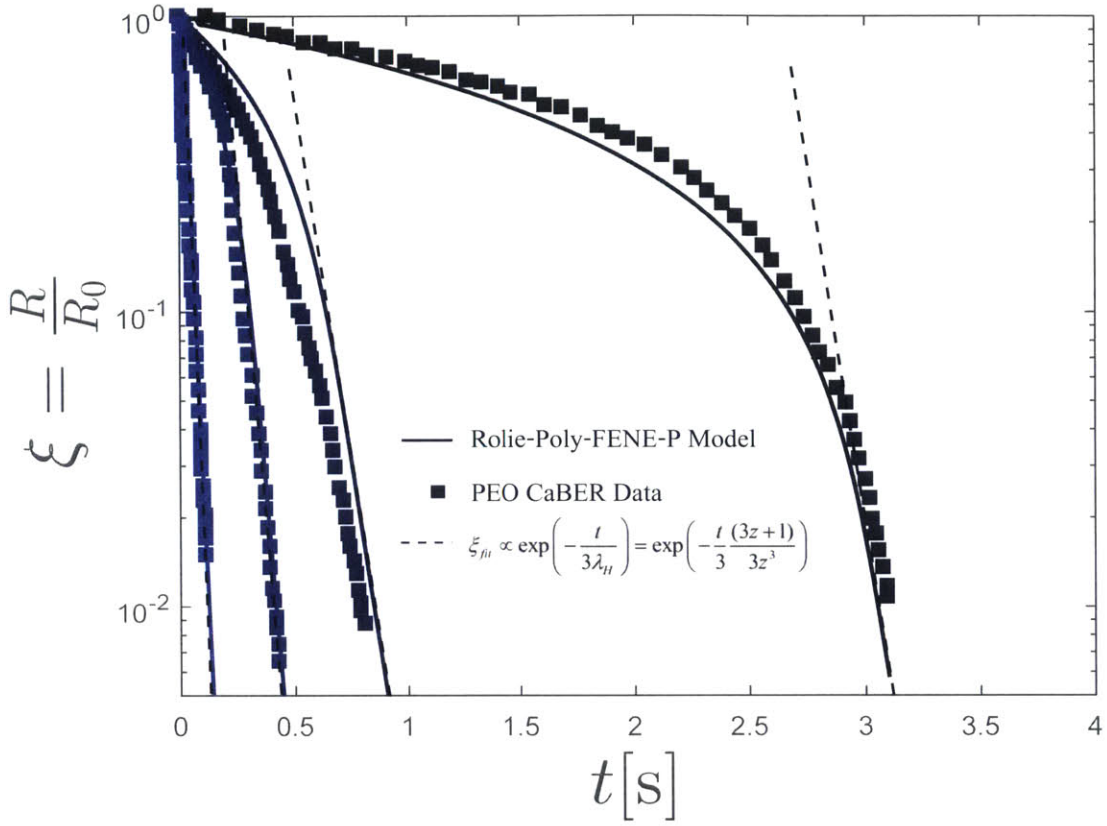

Figure 5-5: Comparison of CaBER data (solid squares) for $MW = 1 \times 10^{6g}/_{mol}$ PEO in water at various concentrations from Arnold et al (2010) [4] and the FENE-P and Rolie-Poly-FENE-P models (solid lines). The various model parameters are tabulated in Table 5.1.

Clearly, the data is well captured by the models at all concentrations considered. The dashed lines drawn are representative of the exponential thinning region predicted during the "middle elastic regime" and are of the form

$$\xi \propto \exp\left(-\frac{t}{3\lambda_H}\right)$$

where λ_H is obtained from the relationship in Equation (5.7). In Figures 4-2 and 4-4, it was shown with the FENE-P model that the initial viscocapillary period can be prolonged by either an increase in relative importance of the solvent viscosity (large S) or an increase in the concentration of the polymer and hence the elastocapillary number (large E_c). A large elastocapillary number essentially means that capillary forces remain unimportant in comparison to polymer stresses for longer times, delaying the onset of the elastocapillary regime. Initially with $c = 5wt\%$, the elastocapillary number $E_c = 9.7$ is large as a result of the high polymer concentration and $S =$

1.53×10^{-3} is very small, reflecting the relative importance of polymer over solvent viscosity. This large E_c effect outweighs the effect of the small value of S and the initial viscocapillary region is indeed very prolonged. As the polymer concentration is decreased, E_c decreases and S increases (as seen in Table 5.1). This is demonstrated by an increasingly short viscocapillary regime. Eventually at $c = 1wt\%$, closer to the concentration limit c^* and below the entanglement limit c_e, $E_c = 0.49$ and $S = 0.0068$. Since the value of b is still relatively small ($b = 3118.8$) and the relaxation time λ_H is on the order of only a few milliseconds, there is no significant "middle elastic time" region observed. However, the trend of rapid initial viscous decay followed by polymer dominated thinning as seen in Figure 4-4 is recovered.

5.4.2 Saliva at various ages

The problem of determining the parameters for the Rolie-Poly-FENE-P model for saliva is slightly more challenging than for the test model of PEO because of the process of degradation. As a result, it was assumed that the molecular weight of the mucin MW as well as the plateau modulus G_N were time dependent.

Esser et al [23] present data on the protein profiles of saliva after $0, 0.5, 1$ and 4 hours. Using a combination of sodium dodecyl sulfate polyacrylamide gel electrophoresis (SDS-PAGE) fractionation of saliva proteins and liquid chromatography tandem mass spectrometry (LC-MS/MS) to identify excised bands, they are able to track the degradation of salivary proteins over time [23]. By assuming that the intensity of the reported data for each protein size is directly related to the quantity of protein present at a given size, an average function can be determined for the decrease in molecular weight of MUC5B as a function of time.

Analysis of intensity peaks for proteins of a given size from the data in [23] allows us to develop an estimate for the rate of degradation of MUC5B, or in other words, a time dependent equation for the mucin molecular weight MW. The obtained result was from examination of protein sized $4610Da$ in the paper, for which the fit equation yields

$$MW(t) = MW_0 \left(\frac{t}{t_0}\right)^{-0.259}, \tag{5.11}$$

where MW_0 is the initial molecular weight of MUC5B ($150 \times 10^{6g}/_{mol}$), t_0 is the time corresponding to MW_0 artificially set to 1 minute, and t is the current time.

The plateau value of the elastic modulus G_N was treated as a fit parameter in order to obtain a reasonable estimate for the number of entanglement segments z which yielded results consistent with the CaBER data. G_N was found to decrease with time, and the numerical values appear largely consistent with the SAOS saliva data presented in Figure 2-3.These values are compiled in Table 5.2, with the remainder of the Rolie-Poly-FENE-P values calculated using Equations (5.8)-(6.4)).

Time[min]	MW[MDa]	G_N[Pa]	M_e [MDa]	z	λ_H[ms]	b
30	62.16	0.45	1.026	60.57	123	4165.23
60	51.95	0.4	1.155	44.99	91	4576.79
120	43.40	0.38	1.215	35.72	74	4768.51
300	34.24	0.3	1.539	22.24	33	5761.19
660	27.91	0.1	4.618	6.04	24	13874.24

Table 5.2: Sticky Network model parameters for saliva at various ages.

In Figure 5-6, the CaBER data reported earlier in Figure 2-6 is plotted as solid squares with the Rolie-Poly-FENE-P model (solid lines) for the various values in Table 5.2. It is clear that the Rolie-Poly-FENE-P performs better than the FENE-P model in terms of reducing the large initial viscous drop in the filament radius, which is not observed experimentally. The network model effectively increases the number density of the mucin chains, by considering entanglement segments as opposed to chains as a whole, which effectively increases the elastocapillary number E_c of the solution. Furthermore, the network interactions and deformation provide greater opposition to

the imposed capillary stress in contrast to the dilute solution considered in the FENE-P model. Additionally, through only changing the molecular weight MW of the mucin and adjusting the plateau modulus G_N accordingly, the Rolie-Poly-FENE-P model is indeed able to capture the trends of decreasing relaxation time $\lambda_H = \frac{3z^3\lambda_e}{(3z+1)}$ and breakup time that are observed as the saliva sample ages. Finally, the "middle elastic time" of the FENE-P model as derived in Equation (5.6) is indeed recovered by the model, as seen by the exponential region (linear on the log-lin graph) for the majority of the filament thinning process.

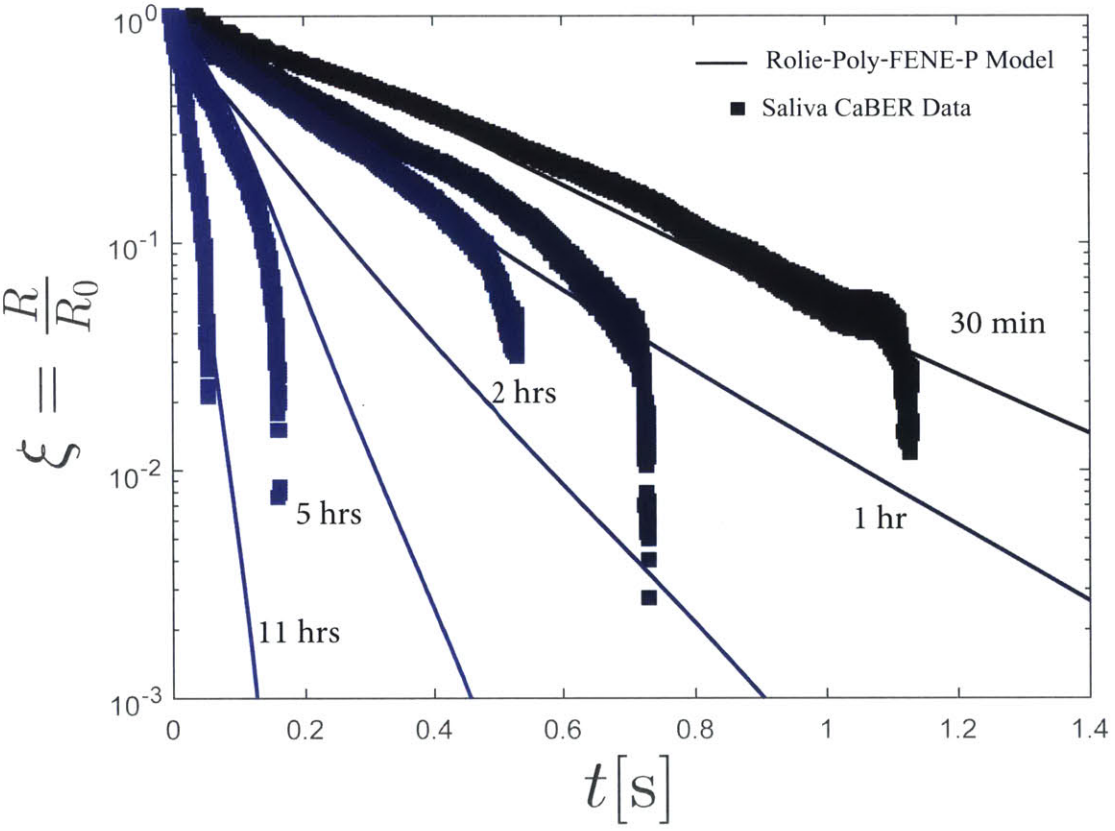

Figure 5-6: Comparison of the Rolie-Poly-FENE-P model with CaBER data for saliva at various ages

One trend that is not at all well captured, however, is the very rapid filament decrease and breakup following the exponential thinning period, observed most noticeably for the younger saliva samples. Examination of Figure 5-6 reveals that at a certain time during the filament thinning process, the entire network collapses in a 'glassy' or 'sticky' rupture, leading to a dramatic decrease in

polymer stresses and rapid breakup of the filament. This sort of behaviour has been previously in the literature by Haward et al in their studies of cross slot extensional flows of saliva [29]. They observe that the extensional viscosity of saliva begins to decrease at shear rates exceeding $\dot{\epsilon} \approx 1200s^{-1}$, and suggest that this could be due to rupture of the disulphide bonds forming the large mucin polymers, and corresponding flow-induced scission of the structures [29].

Therefore, the Rolie-Poly-FENE-P Model accounts for finite extensibility of the polymer chains, but not for a maximum stress that the chains can endure before they rupture. This concept of a dynamic strength for molecular bond adhesion has been considered in many different contexts in the literature. A couple of notable examples can be found in Evans and Ritchie [24], the modeling of 'glassy' or 'sticky' biological networks by Kroy et al [71, 74, 40], and the modeling of Hagfish slime by Ewoldt et al [25]. In the next section, we build on the work by Tripathi et al [67] to develop an analogous Sticky Network model for saliva, and demonstrate that the glassy behaviour observed in CaBER experiments can indeed be observed by considering associating interactions between the mucin chains.

Chapter 6

The Sticky Network Model

6.1 Motivation

The development of a model that can capture the dynamics of a sticky, or associative, network of polymer chains has applications to a wide variety of fields. In many biological systems, it is common to have large macromolecular assemblies in an aqueous solution, in which ion-mediated interactions, hydrogen bonding, protein-protein interactions, etc play a large role in determining the macroscopic mechanical behaviour of the network. Animal cytoskeletons and plant cell walls are ubiquitous examples of such systems [71]. Furthermore, the mechanism by which DNA interacts with proteins is highly dependent on interactions with the surrounding tissue network, as well as much of the process of cell division [40]. There is also precedent for modeling the macroscopic rheological response of mucus and other bodily fluids by associative network models, as has been done by Ewoldt et al in their studies of Hagfish slime. The gel-like nature of saliva is known to be attributed in large part to hydrophobic interactions, calcium-mediated crosslinking, and carbohydrate interactions amongst others between the large mucin chains and their surroundings [61]. As such, it seems reasonable to attempt to extend the concepts of the glassy or sticky network towards the modeling of saliva.

It is often not possible to describe the mechanics of such systems by considering the dynamics of the constituent chains alone [24, 40]. This has motivated the development of the Glassy Worm-

Like Chain model, in which a stickiness parameter is introduced in order to simulate the energy well that the cross-linked chain segments must overcome in order to be able to dissociate from the rest of the network [71]. The depth of the energy well is dependent on the type and strength of interactions in the system and the amount of stretch in the constituent chains: as they are stretched, the energy well they face becomes more shallow, and the chains are more likely to be able to dissociate. This is analogous to what is found in soft glasses, where thermally activated jumping between local traps occurs [71].

In this work, we closely follow the method of Tripathi et al [67], who modeled the shear and extensional rheological properties of hydrophobically modified ethoxylate-urethane (HEUR) systems, and extend their analysis to the modeling of the salivary network under simple elongational flow. HEUR polymers contain both hydrophilic central regions and hydrophobic end groups which associate with one another to minimize their exposure to the surrounding water [67], introducing the 'sticky' character to the network. Tripathi et al model this network as temporary, and allow for destruction and reformation of the network junctions [67]. As such, they consider two network species able to sustain polymer stresses: bridged chains, which join two separate micelles, and dangling chains, for which one end is attached to a micelle and the other is free [67].

The approach taken in this section is to combine the entanglement theory presented in Chapter 5 with the sticky or glassy energy framework presented in [67]. We simplify the model presented by Tripathi et al [67] by considering polymeric stress contributions to accumulate in bridged chains only. This is also the approach taken by Ewoldt et al in their modeling of Hagfish slime [25]. We make the further simplification that only junction destruction occurs, and do not include a mechanism for association. This is motivated by the observations of Haward et al in extensional flows of saliva, who observed a breakdown in the network above a characteristic strain rate [29]. Comparison with saliva CaBER data at the end of the chapter reveals that these provisions for associations between mucin chains allow for much better agreement with experimental data compared to the previous modeling attempts.

6.2 Definition of the Sticky Network model parameters

As was done for the Rolie-Poly-FENE-P model, we consider an entangled network of bead-spring-chain polymers of molecular weight MW. The number of entanglements z and hence the entanglement molecular weight M_e is established using the theory outlined in Section 5.3. Each entanglement segment can be stretched as a result of imposed external flow, and the stress build up in the chain is related to its finite extensibility parameter b (see Equation (3.3)). The parameters of this model are outlined in detail in Chapter 3.

We introduce the concept of associative junctions by considering each entanglement to lie in an energy well of depth ΔG. Physically, this energy well represents the network interactions such as calcium-mediated crosslinks and hydrogen bonds discussed earlier, although in this work we do not attempt to reconcile from a biological perspective the exact form of ΔG in relation to these interactions. The fraction of active chains (meaning those participating in the network, either dangling or bridged) is denoted by ν and depends on the depth of the energy wells through

$$\nu = n\left(\frac{\exp\left(\frac{\Delta G}{k_B T}\right)}{1+\exp\left(\frac{\Delta G}{k_B T}\right)}\right) \tag{6.1}$$

where as before, n is the total number density of chains. Clearly, when ΔG is large compared to the thermal energy, $\nu \approx n$ and all entanglement segments are considered active [67]. At any given time, the subset of elastically active entanglement segments that are bridged, or in other words can contribute to the accumulation of polymer stresses in the network, is defined as ν_a.

The entanglement segments have a characteristic size on the order of their gyration radius given by $l_c = \sqrt{\left(\frac{N_k b_k^2}{3}\right)}$, and the entanglements themselves are assumed to lie within micelles of width r_c, which sets the width of the energy activation barrier and is defined as

$$r_c = l_c \beta \left(\frac{N_k}{2}\right)^{\nu} N_{agg}{}^{\frac{(1-\nu)}{2}} \sqrt{\frac{3}{N_k}} \tag{6.2}$$

where N_k is the number of Kuhn steps in each entanglement segment (Equation (3.2)), ν is the Flory exponent again taken to be $\nu \approx 0.6$, β is a fitting parameter taken to be $\beta = 0.0077$ in this work, and N_{agg} is the micelle aggregation number [67]. This value is estimated to lie between $18 - 28$ for most micellar systems [67], and was taken to be $N_{agg} = 20$ in this work.

The characteristic spacing between micelles is defined as

$$\langle a \rangle^2 = \left(\frac{3N_{agg}}{8\pi n}\right)^{\frac{2}{3}}. \tag{6.3}$$

Clearly, the spacing is related to the number density of polymer chains n. When the network is very dense and n is large, $\langle a \rangle^2 < {l_c}^2$, and as a result the chains interact with other network elements before they have a chance to completely relax along their entire length once dissociation occurs. Although we do not specifically consider associations in this model, this concept will nevertheless be important for defining the network junction dissociation rate $M(\boldsymbol{q}, t)$, where $\boldsymbol{q}$ is the entanglement end-to-end vector.

The rate at which chains exit the network, or the rate of dissociation, is taken to be a product of the natural thermal vibration frequency Ω (where $10^8 < \Omega < 10^{10}$) and the quasi equilibrium likelihood of reaching a transition state given the activation barrier, $\exp\left(-\frac{\Delta G}{k_B T}\right)$ [67]. Hence

$$\lambda_e = \Omega \exp\left(-\frac{\Delta G}{k_B T}\right). \tag{6.4}$$

With these concepts in place, it is possible to define the system of equations governing the model.

6.3 Derivation of the Sticky Network model equations

Following the work of Tripathi et al [67], we define a distribution function Ψ_a to specify the fraction of bridged chains as a function of chain stretch and time, ie $\Psi_a(\boldsymbol{q}, t)$. Ψ_a can also be defined in terms of the volumetric distribution function ψ_a through

$$\Psi_a = \nu_a \psi_a$$

where ψ_a is normalized by $\int \psi_a dV = 1$.

By considering the interactions of the junction points with the flow as done by van den Brule and Hoogerbrugge [69] and Bird et al [10], the continuity equation for the distribution function can be found to be

$$\frac{\partial \Psi_a}{\partial t} = -\frac{\partial}{\partial \boldsymbol{q}} \cdot \left[(\nabla \boldsymbol{v})^T \cdot \boldsymbol{q} \Psi_a \right] - M(\boldsymbol{q}, t) \Psi_a. \tag{6.5}$$

As in the FENE-P model, we introduce the microstructural deformation tensor $\boldsymbol{A}$, to describe the stretch in the entanglement segments. Unlike before, $\boldsymbol{A}$ now depends on whether the chain is bridged or not, and hence

$$\boldsymbol{A} = \frac{1}{l_c^2} \int \boldsymbol{qq} \Psi_a dV. \tag{6.6}$$

The force in each entanglement segment F_e is again defined using a non-linear spring equation as $F_e = Hf(\boldsymbol{A})\boldsymbol{A}$, where H is the spring constant ($H = \frac{3k_B T}{N_k b_k^2}$) and the FENE-P spring term is given by

$$f(\boldsymbol{A}) = \frac{1}{1 - \frac{tr(\boldsymbol{A})}{b}}.$$

Multiplying Equation (6.5) by the second moment tensor $\boldsymbol{qq}$ and integrating over configuration space [67] allows us to arrive at the differential equation governing the evolution of $\boldsymbol{A}$

$$(\nu_a \boldsymbol{A})_{(1)} = -M \nu_a \boldsymbol{A} \tag{6.7}$$

where as before, the subscript (1) notes the upper convected derivative defined in Equation (4.5).

The final element required is the expression for the destruction rate term $M(\boldsymbol{q}, t)$. Following Tripathi et al [67], we can express the destruction rate as

$$M = g(c, M_e)\Omega \exp\left(-\frac{1}{k_B T}\left\{\Delta G - \int_q^{q-r_c} \boldsymbol{F_e} \cdot d\boldsymbol{q}\right\}\right) \tag{6.8}$$

where q is the magnitude of the entanglement end-to-end vector, $q = |\boldsymbol{q}|$ and g is a front factor term that depends on the entanglement segment concentration c and molecular weight M_e. The idea of the decreasing depth of the energy well as a function of entanglement section stretch is clearly demonstrated in the form of Equation (6.8). As the end-to-end vector q increases, the integral of the work term increases, lowering the effective energy barrier term ($\Delta G - Work$), and correspondingly increasing the destruction rate M.

Using the definition of F_e as well as the relationship between $\sqrt{tr(\boldsymbol{A})} = \frac{q}{l_c}$, we arrive at an expression for the destruction rate M

$$M(\boldsymbol{A}, t) = \frac{g}{\lambda_e}\left[\frac{1 - \frac{\left(\sqrt{tr(\boldsymbol{A})} - \sqrt{\frac{3}{N_k}}\beta\left(\frac{N_k}{2}\right)^{\nu} N_{agg}{}^{\frac{(1-\nu)}{2}}\right)^2}{b}}{1 - \frac{tr(\boldsymbol{A})}{b}}\right]^{\frac{b}{2}}. \tag{6.9}$$

Tripathi et al define g in terms of the equilibrium destruction rate (when $tr(\boldsymbol{A}) = 3$) and hence

$$g(c, M_e) = \chi \frac{< a >^2}{l_c^2}\left[\frac{1 - \frac{3}{b}}{1 - \frac{(\sqrt{(3)} - \sqrt{\frac{3}{N_k}}\beta\left(\frac{N_k}{2}\right)^{\nu} N_{agg}{}^{\frac{(1-\nu)}{2}})^2}{b}}\right]^{\frac{b}{2}}. \tag{6.10}$$

All of these concepts are summarized in Figure 6-1.

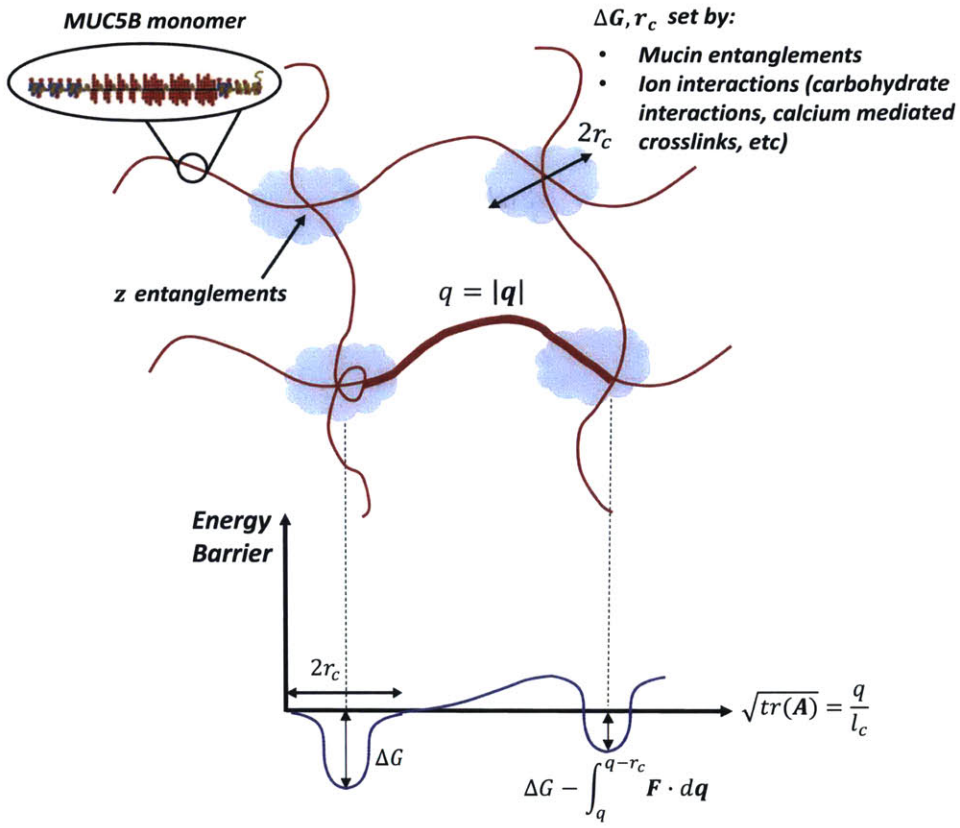

Figure 6-1: Physical description of the system considered in the Sticky Network model. The mucin chains are assumed to be entangled, with the number of entanglements set by the equations outlined in Chapter 5. Furthermore, ion interactions establish an energy well at each of these network junctions, the depth of which depends on the amount of stretch A in each entanglement segment. As the chains become very stretched, the energy well becomes more shallow, and the likelihood of chain detachment increases.

Finally, by imposing the velocity field for simple elongational flow as was done in Chapter 4, we arrive at the final form of the governing equations for the Sticky Network model.

The first equation specifies the time rate of change of the fraction of elastically active entanglement segments that are bridged ν_a, the second specifies the evolution of the axial microstructural deformation A_{zz}, the third specifies the evolution of the radial microstructural deformation A_{rr}, and the final one specifies the overall constitutive equation for the force balance, as expressed in Equation (4.15).

$$\frac{d\nu_a}{dt} = -M\nu_a \tag{6.11}$$

$$\frac{dA_{zz}}{dt} = -\frac{4}{R}\frac{dR}{dt} - 2MA_{zz} \tag{6.12}$$

$$\frac{dA_{rr}}{dt} = \frac{2}{R}\frac{dR}{dt} - 2MA_{rr} \tag{6.13}$$

$$\frac{\sigma}{R} = -\frac{6}{R}\frac{dR}{dt}\eta_s + \nu_a k_B T f(A_{zz} - Arr) \tag{6.14}$$

where M is given by Equation (6.9), and f is the FENE spring term defined above. The simultaneous solution of Equations (6.11)-(6.14) allows for us to solve for the radius evolution in a CaBER type experiment for the Sticky Network model. The initial conditions are similar to those imposed with the FENE-P model: initially, the radius is set to R_0, there is no stretch in the chains ($A_{zz} = A_{rr} = 1$) and the initial fraction of bridged chains is taken to be the total fraction of elastically active chains ($\nu_{a,0} = \nu$).

6.4 Asymptotics analysis

It is of interest to verify whether the 'middle elastic time' of Entov and Hinch [22] discussed in detail in Section 4.4 upon which the extraction of the relaxation time is based for CaBER experiments is recovered by the Sticky Network model. If so, then presumably a relationship between the CaBER relaxation time λ_H observed from the exponential thinning regime of the filament thinning experiment and the parameters of the Sticky Network model can be obtained.

The 'middle elastic time' is defined as the the period of filament thinning in which capillary forces are resisted by and large by axial polymer stresses, before significant enough chain stretch has set in that the FENE spring term becomes significantly different than 1. In other words $b \gg A_{zz} \gg A_{rr}$ and $f \approx 1$ [22]. Introducing these simplifications into Equations (6.9)-(6.14), we arrive at

$$\frac{d\nu_a}{dt} \to -\frac{g}{\lambda_e}\nu_a \tag{6.15}$$

$$\frac{dA_{zz}}{dt} \to -\frac{4}{R}\frac{dR}{dt} - 2\frac{g}{\lambda_e}A_{zz} \tag{6.16}$$

$$\frac{\sigma}{R} \to \nu_a k_B T A_{zz} \tag{6.17}$$

From (6.15), it follows that during the 'middle elastic time',

$$\nu_a \to \nu \exp\left(-\frac{gt}{\lambda_e}\right) \tag{6.18}$$

and

$$A_{zz} \to \left(\frac{1}{\xi}\right)^4 \exp\left(-\frac{2gt}{\lambda_e}\right). \tag{6.19}$$

Combining these results with Equation (6.17) gives us the expression for the evolution of the filament radius during the 'middle elastic time'

$$\xi \to \left(\frac{\nu_a k_B T}{\frac{\sigma}{R_0}}\right)^{\frac{1}{3}} \exp\left(-\frac{gt}{\lambda_e}\right) \tag{6.20}$$

.

Comparison of Equation (6.20) with the the analogous result from the FENE-P model, Equation (4.26) reveals that during the middle elastic regime, there should indeed be an exponential thinning period for the Sticky Network model. Furthermore, the system relaxation time λ_H as typically measured with CaBER is related to the sticky network junction exit rate through

$$\lambda_H \to \frac{\lambda_e}{3g} \tag{6.21}$$

.

A summary of these results are shown in Figure 6-2, where the nondimensional radius ξ as well

as the axial and radial microstructural deformations (A_{zz} and A_{rr}) are plotted as function of the nondimensional time $\tau = \frac{t}{\lambda_H} = \frac{3gt}{\lambda_e}$ for two different sets of parameters. In the following section, we will show that these correspond to the values chosen for a young saliva sample ($t = 30$min)and an older sample ($t = 5$ hours). The major differences between the two parameter choices are the resulting elastocapillary numbers $E_c = \frac{\nu k_B T}{\frac{\sigma}{R_0}}$, and non dimensional viscosities $S = \frac{\eta_s}{G\lambda_H}$. These results are tabulated in Table 6.1. It is clear that between the two samples, E_c drops from nearly unity at the 30 minute parameter choice ($E_c = 0.875$) to an order of magnitude lower, $E_c = 0.094$ at the 5 hour parameter range. This corresponds to a decrease in polymer stress relative to capillary stresses. At the same time, S drops increases from $S = 0.0013$ at the 30 minute parameter choice to $S = 0.042$ at 5 hours, reflecting a decrease in relative importance of polymer viscosity compared to solvent viscosity. The combined effect of these two changes is to increase the duration and decrease in filament radius during the viscocapillary regime, as can be seen by comparison of Figures 6-2a and 6-2b.

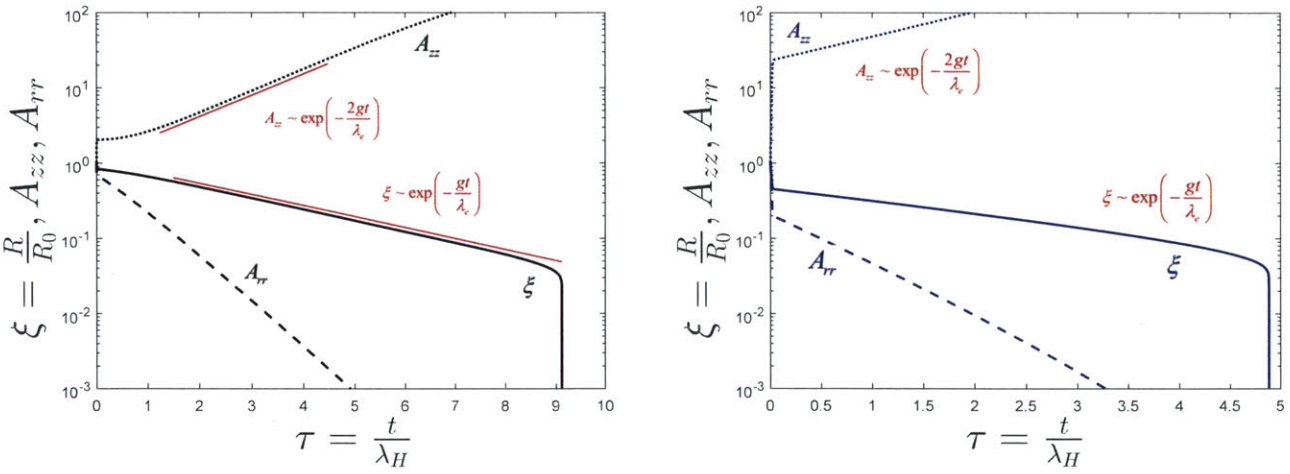

(a) 30 minutes

(b) 5 hours

Figure 6-2: Examination of the axial and radial microstructural deformation A_{zz} and A_{rr} for two model systems of saliva at 30 minutes and 5 hours. The nearly non-existant viscocapillary period in the 30 minute simulation results in the radial microstructural deformation A_{rr} being comparable to the axial microstructural deformation A_{zz} when elastocapillary thinning sets in, resulting in some initial curvature in the radius profile and delay of the onset of the middle elastic time [22]. This is not observed in the 5 hour model where the initial viscous drop is much larger, and as a consequence no radial curvature is observed.

As a result of the very small viscous period in the 30 minute simulation, the radial microstructural deformation term A_{rr} is comparable to the axial term A_{zz} when the elastocapillary regime begins. As a result, there is some curvature observed in the filament radius evolution which is not seen in the 5 hour case, when the 'middle elastic time' requirement of $A_{rr} \ll A_{zz}$ is immediately met.

With this subtlety in mind, however, it is clear that the exponential decay regime of the 'middle elastic time' is indeed met with the Sticky Network model, validating its use for analysis of CaBER data.

6.5 Comparison of Sticky Network model with saliva experiments

Similarly to the procedure followed for the Rolie-Poly-FENE-P model, we specify the chain molecular weight at every time using the approximation developed using data from Esser et al [23] given in Equation (5.11). We furthermore impose the system relaxation λ_H using the value obtained from the CaBER data, and solve for the exit rate λ_e accordingly using Equation (6.21). This also permits the determination of the energy barrier ΔG using Equation (6.4). The procedure is then to fit the plateau modulus G_N in order to obtain a value for the number of entanglements z and entanglement molecular weight M_e, from which the remainder of the molecular properties such as the finite extensibility b can be determined.

The obtained results for these parameters are shown in Table 6.1. The fit values of G_N are slightly higher for the younger samples than we have observed in SAOS data with saliva (see Figure 2-3. However, they are reasonably consistent with other data reported in the literature (see, for example Stading et al [63]), especially considering the fact that in general, salivary literature does not report or account for the age of the sample in question. Furthermore, it is not straightforward to measure the plateau elastic modulus for solutions [75], and so the fact that the values for G_N lie within the appropriate order of magnitude range compared to reported literature is relatively

reassuring.

Time[min]	MW[MDa]	G_N[Pa]	M_e [Da]	z	λ_H[ms]	b	E_c	S
30	62.16	14	3.30×10^4	1884.4	123	266.2	0.875	0.0013
60	51.95	8	5.77×10^4	899.85	91	416.62	0.5	0.0034
120	43.40	5	9.24×10^4	469.98	74	606.78	0.31	0.0077
300	34.24	1.5	3.08×10^5	111.2	33	1589.78	0.094	0.042
660	27.91	0.3	1.54×10^6	18.13	24	5761.2	0.019	0.32

Table 6.1: Sticky Network model parameters for saliva at various ages.

In Figure 6-3, the results for the Sticky Network model using the parameters listed in Table 6.1 are compared with the experimental CaBER data for saliva. Consistent with the experimental data, the large initial viscous drop observed with the FENE-P model is nearly eliminated for the heavily entangled younger samples. As z and M_e decrease with sample age and correspondingly, E_c decreases and Sincreases, the model does predict a substantial viscocapillary dominated region. Although this is not observed in the CaBER data presented, it is not necessarily unphysical. Since the CaBER data is shown only after the strike time, when the plates have reached their final separation height, it is possible that any initial viscous response that could have been observed had the experiment started immediately from the final stretch position is missed since it occurs during the plate separation; a period of the experiment that the model cannot capture.

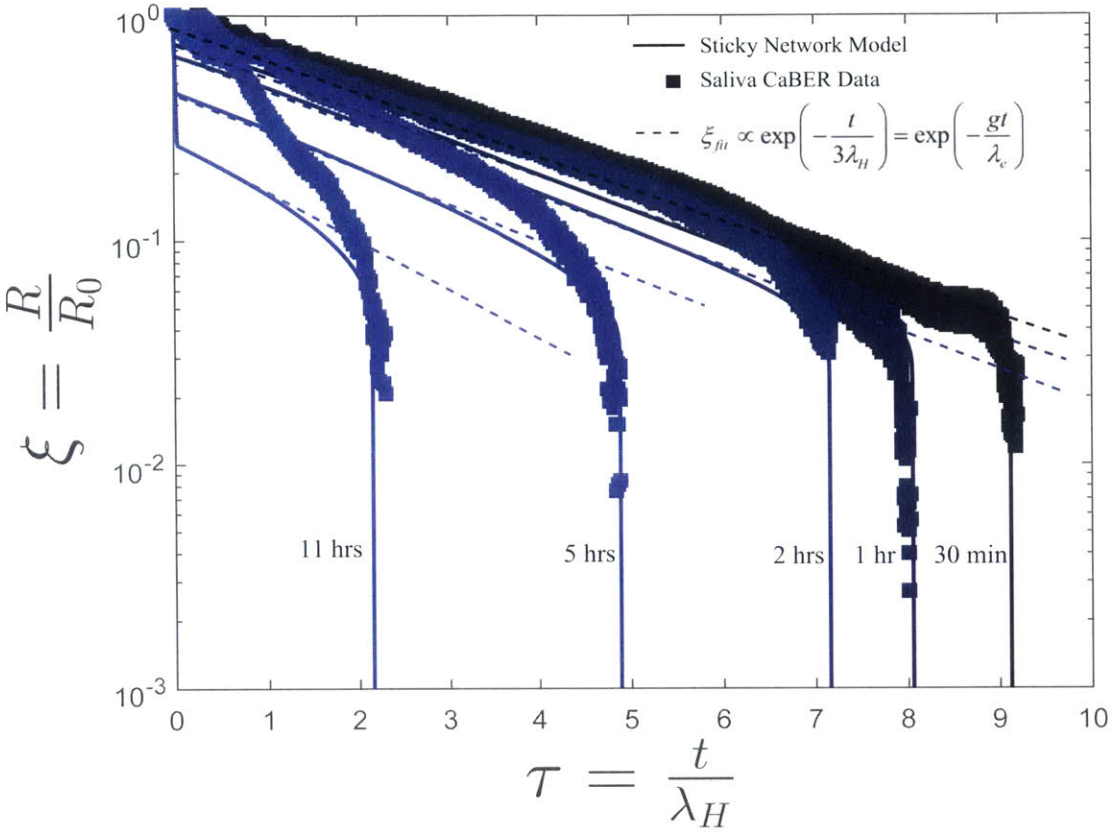

Figure 6-3: Comparison of the Sticky Network model with CaBER data for saliva at various ages

The sticky network model is also able to capture the exponential decay region characteristic of the 'middle elastic time', during which the strain rate is essentially constant and the slope matches that obtained from the CaBER data.

Ultimately, however, the most significant improvement of this model compared to the FENE-P and Rolie-Poly-FENE-P models is its ability to capture the sharp filament rupture behaviour characteristic of the sticky network nature of salivary fluid, particularly for the younger samples. Equation (6.15) reveals that during the middle elastic time, the fraction of bridged chains decays as $\sim \exp\left(-\frac{gt}{\lambda_e}\right)$. However, as the chain begin to reach their extension limits, the term in square brackets in the expression for M (Equation (6.9)) begins to deviate significantly from 1, and the decay rate of nu_a begins to increase dramatically, leading to a sudden failure of the network and plummeting of the filament radius. This idea of a 'glassy' rupture is in line with the work

done by Kroy et al in their considerations of other sticky biological networks ([40, 71]), as well as the observations by Haward et al [29] regarding the rather sudden and dramatic rupture of the salivary network above a certain strain rate under elongational crossflow. Additionally, the parameters calculated for the model are physical and consistent with biological data available in the literature. As such, modeling saliva as an associative entangled mucin network seems like a promising approach for future understanding of its rheological behaviour under various flow conditions.

Chapter 7

Conclusion

To conclude, this thesis provides new and thorough data for the shear and extensional rheology of saliva. One of the major contributions presented by this data is the inclusion of the notion of salivary degradation, and a characterization of the properties of saliva at various ages. Considering the increasing frequency with which the properties of salivary fluid and other bodily mucus secretions are being used as medical diagnostic tools, being able to account for the stability of their rheological properties with an accurate model is of tremendeous use [39, 9, 78]. Following the observation that in particular the extensional rheological properties of saliva are unstable with time, the primary objective of this thesis was to develop a model that could capture the observed trends of decreasing time to breakup and relaxation time observed by CaBER for samples of saliva at different ages following extraction from the mouth.

Examination of the structure of saliva reveals that much of its viscoelasticity can be attributed to the presence of large salivary MUC5B mucins [61]. We hypothesized that over time, once the saliva was extracted from the mouth, enzymatic activity and degradation cause a decrease in the molecular weight of the constituent MUC5B chains. This hypothesis was reinforced by protein profile data from Esser et al [23] for saliva, which appears to show a decrease in intensity of salivary proteins of specific sizes as a function of time following extraction from the mouth. By fitting a crude power law to this intensity data, an estimate for the time rate of change of MUC5B molecular weight was developed. It was therefore desired to develop a model for which decreasing

the polymer molecular weight could result in a decrease in the observed relaxation time and time to breakup under simple elongational flow.

As a result, the first modeling attempt was to assume a dilute solution of FENE-P springs (representing the mucins) in a Newtonian solvent, and attempt to relate the model parameters from the biological properties of the mucin. The advantage of this simple approach was the ability to derive a composite analytic solution (with an explicit result for the breakup time and an implicit equation for the radius evolution as a function of time) that matched the numerical solution examined in detail by Entov and Hinch [22] extremely well. The disadvantage was that the model missed some of the key aspects of the dynamics of the filament thinning process. In particular, the model predicted a large initial viscocapillary decrease in the filament radius that was not observed experimentally, and the sharp filament rupture behaviour observed particularly in the younger samples was not captured.

The next attempt was to consider the dynamics of an entangled network, including the relaxation mechanisms of reptation, retraction, and constraint release, through the Rolie-Poly Model developed by Graham et al [45, 50]. To this model, we added in chain finite extensibility using the same principles as in the FENE-P model, in order to develop the Rolie-Poly-FENE-P model. By considering the dynamics of the entangled network as a whole, and the stretch of entanglement segments as opposed to the entire chain, the initial viscocapillary drop was largely eliminated, which was more consistent with the experimental results. However, this model still had no mechanism to account for glassy or sticky behaviour that could cause the network to collapse at a particular level of stress, and so the dramatic filament rupture behaviour observed experimentally could not be reproduced.

The final model considered built off of the foundation of the finitely extensible entanglement network developed in the Rolie-Poly-FENE-P model, but following the method of Tripathi et al [67], allowed for inclusion of junction interactions in the form of a 'stickiness' parameter, or energy

well, that the junctions needed to be able to overcome in order to dissociate from the remainder of the network. This approach of treating saliva as a sticky or glassy gel has much precedent in the literature for the modeling of biopolymer systems. Kroy et al applied it to the study of plant polysaccharide systems and DNA/protein interaction systems [40, 71] while Ewoldt et al applied it towards the modeling of Hagfish slime [25]. The depth of the energy well faced by the junctions was modeled to decrease as a function of stretch in the entanglement segments. In the context of a CaBER experiment, this implies that as the chains begin to reach their finite extensibility, the likelihood that they will detach from the rest of the network increases very quickly. Ultimately, there is a point at which most of the chains detach, and the polymer stress that the network is able to sustain plummets dramatically, leading to a sudden rupture in the filament radius. With this model, the CaBER data for saliva at various ages (accessed by decreasing the molecular weight of the chains) was able to be reproduced very well.

In terms of future work, it would still be of great interest to understand more about the biological side of the process of degradation, which would shed light on whether the assumption of decreasing mucin molecular weight with time is a valid one. Suggested experiments include adding protease inhibitors or accelerators to the saliva, in order to try to be able to tune the degradation process and understand more about the conformational changes to the biopolymers. It is also of interest to apply this notion of the effect of mucin structure on mucus and saliva rheology towards using the properties of these fluids as diagnostic tools for disease. There is evidence that different ratios of various mucins can lead to pathologies in mucus structure in cystic fibrosis and other diseases, which can result in extreme difficulty in clearing mucus for those afflicted [38]. Developing this model further to be able to account for protein structure more carefully and different mucin species could therefore be extremely useful for developments in this field.

Bibliography

[1] A. Aggazzotti. Modificazioni della viscosita della saliva mista dopo che e'stata secretata in rapporto col potere filante e colla tensione superficiale. *Arcghivio di fisiologia*, 20:3–15, 1922.

[2] S. L. Anna and G. H. McKinley. Elasto-capillary thinning and breakup of model elastic liquids. *Journal of Rheology*, 45(1):115, 2001.

[3] S. L. Anna, G. H. McKinley, D. a. Nguyen, T. Sridhar, S. J. Muller, J. Huang, and D. F. James. An interlaboratory comparison of measurements from filament-stretching rheometers using common test fluids. *Journal of Rheology*, 45(1):83, 2001.

[4] O. Arnolds, H. Buggisch, D. Sachsenheimer, and N. Willenbacher. Capillary breakup extensional rheometry (CaBER) on semi-dilute and concentrated polyethyleneoxide (PEO) solutions. *Rheologica Acta*, 49(11):1207–1217, 2010.

[5] R. Bansil and B. S. Turner. Mucin structure, aggregation, physiological functions and biomedical applications. *Current Opinion in Colloid and Interface Science*, 11(2-3):164–170, 2006.

[6] P. J. Basser, T. a. McMahon, and P. Griffith. The mechanism of mucus clearance in cough. *Journal of biomechanical engineering*, 111(4):288–297, 1989.

[7] A. Bazilevsky, V. Entov, and A. Rozhkov. Failure of an Oldroyd liquid bridge as a method for testing the rheological properties of polymer solutions. *Polymer Sciences Series A (Translated from Vysokomolekulyarnya Soedineniya Seriya A pp. 474-482)*, 43:1161–1172, 2001.

[8] A. V. Bazilevsky, V. M. Entov, and A. N. Rozhkov. Liquid Filament Microrheometer and Some of Its Applications. In D. R. Oliver, editor, *Third European Rheology Conference and*

Golden Jubilee Meeting of the British Society of Rheology SE - 21, pages 41–43. Springer Netherlands, 1990.

[9] A. V. Bazilevsky, V. M. Entov, and A. N. Rozhkov. Breakup of a Liquid Bridge as a Method of Rheological Testing of Biological Fluids. 46(4):613–622, 2011.

[10] R. Bird, C. Curtiss, R. Armstrong, and O. Hassager. *Dynamics of Polymeric Liquids, Kinetic Theory (Volume 2)*. Wiley and Sons, 1987.

[11] R. Bird, P. Dotson, and N. Johnson. Polymer solution rheology based on a finitely extensible beadspring chain model. *Journal of Non-Newtonian Fluid Mechanics*, 7(2-3):213–235, 1980.

[12] R. Bird and O. Hassager. *Dynamics of Polymeric Liquids, Fluid Mechanics (Volume 1)*. Wiley and Sons, 1987.

[13] J. H. H. Bongaerts, D. Rossetti, and J. R. Stokes. The lubricating properties of human whole saliva. *Tribology Letters*, 27(3):277–287, 2007.

[14] L. Bourouiba, E. Dehandschoewercker, and J. Bush. Violent expiratory events: on coughing and sneezing. *Journal of Fluid Mechanics*, 745:537–563, 2014.

[15] L. Campo-Deaño and C. Clasen. The slow retraction method (SRM) for the determination of ultra-short relaxation times in capillary breakup extensional rheometry experiments. *Journal of Non-Newtonian Fluid Mechanics*, 165(23-24):1688–1699, 2010.

[16] J. P. Celli, B. S. Turner, N. H. Afdhal, R. H. Ewoldt, G. H. McKinley, R. Bansil, S. Erramilli, and S. Erramilli. Rheology of gastric mucin exhibits a pH-dependent sol-gel transition. *Biomacromolecules*, 8(5):1580–1586, 2007.

[17] S. Clarke, J. Jones, and D. Oliver. Flow in Airways. *Journal of Applied Physiology*, 29(4):464–471, 1970.

[18] C. Clasen, J. P. Plog, and W. Kulicke. How dilute are dilute solutions in extensional flows ? *Journal of Rheology*, 50:849–881, 2006.

[19] P. G. de Gennes. Reptation of a Polymer Chain in the Presence of Fixed Obstacles. *The Journal of Chemical Physics*, 55(2), 1971.

[20] J. Dekker, J. W. a. Rossen, H. a. Büller, and a. W. C. Einerhand. The MUC family: An obituary. *Trends in Biochemical Sciences*, 27(3):126–131, 2002.

[21] J. Eggers. Nonlinear dynamics and breakup of free-surface flows. *Reviews of Modern Physics*, 69(3):865–930, 1997.

[22] V. Entov and E. Hinch. Effect of a spectrum of relaxation times on the capillary thinning of a filament of elastic liquid. *Journal of Non-Newtonian Fluid Mechanics*, 72(1):31–53, 1997.

[23] D. Esser, G. Alvarez-Llamas, M. de Vries, D. Weening, R. J. Vonk, and H. Roelofsen. Sample stability and protein composition of saliva: Implications for its use as a diagnostic fluid. *Biomarker Insights*, 2008(3):25–37, 2008.

[24] E. Evans and K. Ritchie. Dynamic strength of molecular adhesion bonds. *Biophysical journal*, 72(4):1541–1555, 1997.

[25] R. H. Ewoldt, T. M. Winegard, and D. S. Fudge. Non-linear Viscoelasticity of Hagfish Slime. *International Journal of Non-Linear Mechanics*, 46:627–636, 2011.

[26] G. Fano. Contributo allo studio dei corpi filanti. *Archivio di fisiologia*, 5:365–370, 1908.

[27] M. Ferguson and M. Barker. Saliva substitutes in the management of salivary gland dysfunction. *Advanced Drug Delivery Reviews*, 13(1-2):151–159, 1994.

[28] E. S. Frenkel and K. Ribbeck. Salivary Mucins Protect Surfaces from Colonization by Cariogenic Bacteria. *Applied and Environmental Microbiology*, 81(1):332–338, 2014.

[29] S. J. Haward, J. a. Odell, M. Berry, and T. Hall. Extensional rheology of human saliva. *Rheologica Acta*, 50(11-12):869–879, 2011.

[30] S. J. Haward, V. Sharma, C. P. Butts, G. H. McKinley, and S. S. Rahatekar. Shear and Extensional Rheology of Cellulose/Ionic Liquid Solutions. *Biomacromolecules*, 13(5):1688–1699, May 2012.

[31] S. D. Hoath, D. C. Vadillo, O. G. Harlen, C. McIlroy, N. F. Morrison, W. K. Hsiao, T. R. Tuladhar, S. Jung, G. D. Martin, and I. M. Hutchings. Inkjet printing of weakly elastic polymer solutions. *Journal of Non-Newtonian Fluid Mechanics*, 205:1–10, 2014.

[32] T. Inatomi, A. S. Tisdale, Q. Zhan, S. Spurr-Michaud, and I. K. Gipson. Cloning of rat Muc5AC mucin gene: comparison of its structure and tissue distribution to that of human and mouse homologues. *Biochemical and Biophysical Research Communications*, 236(3):789–797, 1997.

[33] A. Jaishankar and G. McKinley. A fractional K-BKZ constitutive formulation for describing the nonlinear rheology of multiscale complex fluids. *Journal of Rheology (1978-present)*, 58(6), 2014.

[34] A. Jaishankar, V. Sharma, and G. H. McKinley. Interfacial viscoelasticity, yielding and creep ringing of globular proteinsurfactant mixtures. *Soft Matter*, 7(17):7623–7634, 2011.

[35] A. Jaishankar, M. Wee, L. Matia-Merino, K. K. T. Goh, and G. H. McKinley. Probing hydrogen bond interactions in a shear thickening polysaccharide using nonlinear shear and extensional rheology. *Carbohydrate Polymers*, 123(0):136–145, June 2015.

[36] K. K. Kabanemi and J. F. Hétu. Nonequilibrium stretching dynamics of dilute and entangled linear polymers in extensional flow. *Journal of Non-Newtonian Fluid Mechanics*, 160(2-3):113–121, 2009.

[37] M. Kesimer, A. M. Makhov, J. D. Griffith, P. Verdugo, and J. K. Sheehan. Unpacking a gel-forming mucin: a view of MUC5B organization after granular release. *American journal of physiology. Lung cellular and molecular physiology*, 298(1):L15–L22, 2010.

[38] M. King. Is cystic fibrosis mucus abnormal? *Pediatric research*, 15(2):120–122, 1981.

[39] L. Kopito and H. Kosasky. The tackiness rheometer determination of the viscoelasticity of cervical mucus. *Human Reproductive Medecine*, 3:351–361, 1979.

[40] K. Kroy. Dynamics of wormlike and glassy wormlike chains. *Soft Matter*, 4(12):2323, 2008.

[41] J. C. M. Lam, K. Kairaitis, M. Verma, J. R. Wheatley, and T. C. Amis. Saliva production and surface tension: influences on patency of the passive upper airway. *The Journal of physiology*, 586(Pt 22):5537–5547, 2008.

[42] R. G. Larson. *The structure and rheology of complex fluids.* Oxford University Press, New York, 1999.

[43] R. G. Larson, T. Sridhar, L. G. Leal, G. H. McKinley, a. E. Likhtman, and T. C. B. McLeish. Definitions of entanglement spacing and time constants in the tube model. *Journal of Rheology*, 47(3):809, 2003.

[44] R. Liang and M. Mackley. Rheological characterization of the time and strain dependence for polyisobutylene solutions. *Journal of Non-Newtonian Fluid Mechanics*, 52(3):387–405, 1994.

[45] A. E. Likhtman and R. S. Graham. Simple constitutive equation for linear polymer melts derived from molecular theory: Rolie-Poly equation. *Journal of Non-Newtonian Fluid Mechanics*, 114(1):1–12, 2003.

[46] G. Marrucci. Dynamics of entanglements: A nonlinear model consistent with the Cox-Merz rule. *Journal of Non-Newtonian Fluid Mechanics*, 62(2-3):279–289, 1996.

[47] G. McKinley and T. Sridhar. Filament-stretching rheometry of complex fluids. *Annu. Rev. Fluid Mech.*, 34:375–415, 2002.

[48] G. H. McKinley. Visco-Elasto-Capillary Thinning and Break-Up of Complex Fluids. *Polymer*, 2005(05):1274–1277, 2005.

[49] G. H. McKinley and A. Tripathi. How to extract the Newtonian viscosity from capillary breakup measurements in a filament rheometer. *Journal of Rheology*, 44(3):653, 2000.

[50] S. T. Milner, T. C. B. McLeish, and a. E. Likhtman. Microscopic theory of convective constraint release. *Journal of Rheology*, 45(2):539, 2001.

[51] N. F. Morrison and O. G. Harlen. Viscoelasticity in inkjet printing. *Rheologica Acta*, 49(6):619–632, 2010.

[52] D. T. Papageorgiou. On the breakup of viscous liquid threads. *Physics of Fluids (1994-present)*, 7(7), 1995.

[53] A. Peterlin. Hydrodynamics of macromolecules in a velocity field with longitudinal gradient. *Polymer Letters*, 4:287–291, 1966.

[54] A. Preetha and R. Banerjee. Comparison of artificial saliva substitutes. *Trends in Biomaterials and Artificial Organs*, 18(2):178–186, 2005.

[55] P. Rantonen and J. Meurman. Viscosity of whole saliva. *Acta odontologica Scandinavia*, 56:210–214, 1998.

[56] B. D. E. Raynal, T. E. Hardingham, J. K. Sheehan, and D. J. Thornton. Calcium-dependent protein interactions in MUC5B provide reversible cross-links in salivary mucus. *Journal of Biological Chemistry*, 278(31):28703–28710, 2003.

[57] B. D. E. Raynal, T. E. Hardingham, D. J. Thornton, and J. K. Sheehan. Gel-Forming Properties of Saliva. *Pharmacia*, 296:289–296, 2002.

[58] A. Round, M. Berry, T. J. McMaster, S. Stoll, D. Gowers, a. P. Corfield, and M. J. Miles. Heterogeneity and persistence length in human ocular mucins. *Biophysical journal*, 83(3):1661–1670, 2002.

[59] D. Sachsenheimer, B. Hochstein, and N. Willenbacher. Experimental study on the capillary thinning of entangled polymer solutions. *Rheologica Acta*, 53(9):725–739, 2014.

[60] P. W. Scherer and L. Burtz. Fluid mechanical experiments relevant to coughing. *Journal of biomechanics*, 11(4):183–187, 1978.

[61] R. G. Schipper, E. Silletti, and M. H. Vingerhoeds. Saliva as research material: Biochemical, physicochemical and practical aspects. *Archives of Oral Biology*, 52(12):1114–1135, 2007.

[62] V. Soland, G. Brock, and M. King. Effect of airway wall flexibility on clearance by simulated cough. *Journal of applied physiology (Bethesda, Md. : 1985)*, 63(2):707–712, 1987.

[63] M. Stading, D. Johansson, C. Diogo-löfgren, and C. Christersson. Viscoelastic properties of saliva from different glands. *ANNUAL TRANSACTIONS OF THE NORDIC RHEOLOGY SOCIETY*, 17:1–4, 2009.

[64] J. Stokes and G. A. Davies. Viscoelasticity of human whole saliva collected after acid and mechanical stimulation. *Biorheology*, 44(3):141–160, 2007.

[65] S. Takehara, M. Yanagishita, K. A. Podyma-Inoue, and Y. Kawaguchi. Degradation of MUC7 and MUC5B in Human Saliva. *PLoS ONE*, 8(7):1–9, 2013.

[66] M. Torres, B. Hallmark, I. Wilson, and L. Hilliou. Natural Giesekus fluids: Shear and extensional behavior of food gum solutions in the semidilute regime. *AIChE Journal*, 60(11):3902–3915, 2014.

[67] A. Tripathi, K. C. Tam, and G. McKinley. Rheology and Dynamics of Associative Polymers in Shear and Extension: Theory and Experiments. *Macromolecules*, 39:1981–1999, 2006.

[68] D. C. Vadillo, W. Mathues, and C. Clasen. Microsecond relaxation processes in shear and extensional flows of weakly elastic polymer solutions. *Rheologica Acta*, 51(8):755–769, 2012.

[69] B. van den Brule and P. Hoogerbrugge. Brownian Dynamics simulation of reversible polymeric networks. *Journal of Non-Newtonian Fluid Mechanics*, 60(2-3):303–334, 1995.

[70] J. van Meerveld. Modified constraint release in molecular based reptation models for fast flows. *Journal of Non-Newtonian Fluid Mechanics*, 122:263–272, 2004.

[71] R. R. R. Vincent, B. W. Mansel, A. Kramer, K. Kroy, and M. A. K. Williams. Microrheological behaviour and nonlinear rheology of networks assembled from polysaccharides from the plant cell wall. *New Journal of Physics*, 15:1–21, 2013.

[72] J. Voynow and B. Rubin. Mucins, mucus, and sputum. *Chest*, 135(2):505–512, 2009.

[73] C. Wagner, L. Bourouiba, and G. H. McKinley. An analytic solution for capillary thinning and breakup of FENE-P fluids. *Journal of Non-Newtonian Fluid Mechanics*, 218:53–61, 2015.

[74] L. Wolff, P. Fernandez, and K. Kroy. Inelastic mechanics of sticky biopolymer networks. *New Journal of Physics*, 12:1–17, 2010.

[75] X. Ye, R. G. Larson, C. Pattamaprom, and T. Sridhar. Extensional properties of monodisperse and bidisperse polystyrene solutions. *Journal of Rheology*, 47(2):443, 2003.

[76] G. Zayas, M. C. Chiang, E. Wong, F. MacDonald, C. F. Lange, A. Senthilselvan, and M. King. Cough aerosol in healthy participants: fundamental knowledge to optimize droplet-spread infectious respiratory disease management. *BMC Pulmonary Medicine*, 12(1):11, 2012.

[77] A. Ziolkovska. Laws of flaxseed mucilage extraction. *Food Hydrocolloids*, 26(1):197–204, 2012.

[78] E. Zussman, A. Yarin, and R. M. Nagler. Age- and flow-dependency of salivary viscoelasticity. *Journal of dental research*, 86(3):281–285, 2007.